EXPERIMENTAL INVESTIGATION OF HYDRODYNAMIC SELF-ACTING GAS BEARINGS AT HIGH KNUDSEN NUMBERS

BY

YIAO-TEE HSIA

GERALD A. DOMOTO

JUL 1980   156

DTIC ELECTE JUL 3 0 1980 D C

Report No. 28 (Final) 1977-1980

Tribology and Lubrication Research Laboratory

School of Engineering and Applied Science

Department of Mechanical Engineering

Columbia University

in the City of New York

New 411869

TABLE OF CONTENTS

Accession For

NTIS GRA&I
DDC TAB
Unannounced
Justification

By
Distribution/
Availability Codes

Dist   Avail and/or
        special

A

ABSTRACT

EXPERIMENTAL INVESTIGATION OF
HYDRODYNAMIC SELF-ACTING GAS BEARINGS
AT HIGH KNUDSEN NUMBERS

This investigation gives experimental confirmation of the "slip flow" theory, developed by Burgdorfer, for modelling hydrodynamic gas bearing with clearances below 0.25 μm. An interferometric technique using two CW lasers is used to measure the small clearances with an 0.025 μm accuracy. The pitch and roll angles of the slider bearing and the surface contour of the slider are also measured interferometrically.

The effects of molecular rarefaction are studied by operating the bearing in different gas media with different mean free paths. Air is used to study Knudsen number below 0.5 while helium is used to study Knudsen number above 0.5.

Experimentally measured trailing edge clearances and pitch angles are compared with theoretical predictions using the "modified" Reynolds equation with velocity slip boundary conditions. The modified Reynolds equation is solved numerically using two different numerical algorithms. Excellent agreement between experiment and theory is found for clearances as high as 1.60 μm to as low as 0.075 μm with corresponding ambient Knudsen number of 0.04 and 2.51, respectively.

ACKNOWLEDGMENT

Doroff.   Without the continued sponsorship and financial
support of the Office of Naval Research, the study would
have been impossible.

1. INTRODUCTION

This investigation is an experimental study of hydrodynamic, self-acting, gas-lubricated bearings operating under "slip-flow" conditions. Conventional lubrication theory developed for gas bearings cannot be applied to the type of bearing under study because the fluid inside the gas film cannot be assumed to be a continuum, that is, the molecular mean free path of the gas is not negligible compared with the bearing clearance. Under this condition, slippage between the gas and the bearing walls will occur and must be considered in the theoretical model. Burgdorfer [5] has developed a slip-flow model in which first order approximation of the velocity slip at the boundaries is considered and a so-called "modified" Reynolds equation is derived. This equation is now used as the governing equation for hydrodynamic, gas-lubricated bearings operating under "slip-flow" conditions. Burgdorfer further asserted that as long as the ratio of the molecular mean free path of the gas and the film thickness (known as the Knudsen number) is between 0 and 1, the modified Reynolds equation will be sufficient to describe the flow phenomenon. Flows with Knudsen numbers between 0.01 and 0.1 are known as slip flows, while flows with Knudsen numbers between 0.1 and 1.0 are known as transition flows. Presently there exist some experimental data to confirm the applicability of the slip-flow approximation to the slip flow regime. However, there is very little experimental data presently to verify the applicability of the slip-flow approximation to the transition flow regime.

Experimental investigations by Tseng [35] and Sereny [33] attempted to study the equation over the full range of Knudsen numbers, that is, in both slip flow and transition flow regimes. However, due to the experimental procedure used in their experiments, the effects of molecular slip could not be studied for Knudsen numbers greater than 0.1. In both studies, even though the ambient Knudsen number was increased beyond 0.1 by reducing the ambient operating pressure, the additional molecular slippage effects expected as the result of the increase in mean free path were offset by the effects of high bearing number or compressibility number, Λ , which was also increased by the lowering the ambient pressure since the bearing number is inversely proportional to the ambient pressure, i.e. $\Lambda = 6\mu U l/(p_a h_t^2)$. Thus, increasing the Knudsen number by decreasing the operating pressure does not necessarily increase the molecular rarefaction effects.

Recently, an experimental investigation by Kogure, Kaneko, and Mitsuya [21] has shown that the modified Reynolds equation is valid for Knudsen number up to 0.3. In their work, the Knudsen number was increased by decreasing the bearing clearance through reducing the bearing width. In contrast to the work of Tseng [35] and Sereny [33], the increased molecular slip effect in Kogure's work was not overshadowed by the high bearing number effect. However, this recent study by Kogure was limited to the low end of the transition flow regime.

In the present experimental investigation, in order to minimize the high bearing number effects and maximize

the molecular rarefaction effects, the bearing is tested in different gas media of different ambient mean free paths. More specifically, air is used to study Knudsen numbers below 0.5 while helium is used to study Knudsen numbers above 0.5. Furthermore, slider bearings of various width are used to change the bearing clearance which in turn will change the Knudsen number. This investigation represents the first work that has successfully studied the hydrodynamic, self-acting, gas-lubricated bearing operating over a wide range of Knudsen numbers (that is, in both slip flow and transition flow regimes) without the presence of high bearing number effects.

The experimental results of this investigation confirm the validity of the modified Reynolds equation for the entire reported range of Knudsen numbers, between 0 and 1. Moreover, the results also showed that the modified Reynolds equation is also capable of describing the flow phenomenon for ambient Knudsen number far beyond 1.0.

In addition to the experimental work, the investigation also examined the accuracy of the numerical solution of the modified Reynolds equation. Two finite-difference algorithms were used to solve the equation. Numerical results - the predicted load and pitch angle - from the two algorithms agree with each other to within 2%.

2. STATE OF THE ART

The study of ultra thin gas film bearing has become of great interest in recent years. One of the prime motivations has come from the computer magnetic disk recording industry where higher recording density and signal resolution can be achieved if the read/write element which is attached to a taper-flat slider can be maintained at a closer spacing over the magnetic disk rotating at a high speed. It has been established by Hoagland [19] and Pear [24] that the recording density can be greatly increased if the slider/disk separation is reduced. In actual operation, due to the relative motion of the disk and the taper-flat slider, a hydrodynamic self-acting gas lubricated bearing is established between the two surfaces. The total pressure force generated within the gas film balances exactly the externally applied force on the slider. The physical situation described is illustrated schematically in Figure 11-2. Thus, to design a recording system where a proper slider/disk separation can be maintained, an accurate model of the bearing system is needed.

Since the first conception and application of the disk recording head element in 1956, the classical Reynolds equation has been found to predict well the performance of the air bearing operating with film thicknesses on the order of 8 to 10 μm [4]. The sliders studied by [4] were either plane flat sliders or convex sliders with very large width to length ratio or slenderness ratio (about 1.3). As the slider underwent design changes in order to increase the recording density,

the result was a reduction in the bearing clearance from 8 μm to 1 μm [35]. The single pad slider geometry also became more sophisticated with a taper-flat surface and a slenderness ratio of 2.0. To further increase the recording density, the bearing clearance was further reduced from 1 μm to the present 0.5 μm. The slider geometry was also changed to the present double pad arrangem nt with taper-flat surfaces and a slenderness ratio of 0.1. This type of head is known as the Winchester head and is shown schematically in Figure 11-3.

As the bearing clearance is reduced to the present 0.5 μm value, the classical Reynolds equation used to describe the fluid flow phenomenon in the bearing film is no longer adequate. It has been shown by Burgdorfer [5] that as the slider/disk separation is substantially reduced, the classical Reynolds equation must be modified to take into account molecular slip at the gas/solid interfaces. The main effect of this molecular rarefaction is to reduce the load carrying capacity of the slider bearing. Figure 11-4 shows the extent of this molecular slip effect as the mean free path of the gas medium is increased at constant ambient pressure. As the figure indicates, for fixed trailing edge clearance, less external load is required to maintain the bearing at that clearance when slip is present. In other words, if the load on the slider is fixed, the slider will operate at a lower clearance when molecular slip is considered. Thus, if molecular slip is not properly accounted for in designing the bearing system, substantial error can result in predicting the bearing clearance for constant load.

The modified Reynolds equation is theoretically valid for Knudsen number up to 1. However, there exist very little experimental data presently to substantiate the slip-flow approximation of the Reynolds equation developed by Burgdorfer [5] over the entire range of Knudsen numbers (from 0 to 1.0).

Hsing and Malanoski [20] were the first investigators to attempt to confirm the validity of the "slip-flow" theory as applied to a spiral grooved thrust bearing. They compared their theoretically predicted pressures to those measured by Sternak [20] and found significant improvement in the theoretically results when slip was considered. Excellent agreement was found for certain range of operating conditions - compressibility number less than 100 and ambient Knudsen number less than 0.1. However, for conditions above this range, the slip-flow theory begins to fail quite rapidly. Consequently, Hsing and Malanoski seriously questioned the validity of the slip-flow approximation when the ambient Knudsen number becomes greater than 0.1, that is in the transition flow regime.

The first experimental work that attempted to study the slip-flow approximation as applied to the slider bearing system was carried out by R.C. Tseng [35]. In his work, Tseng was interested primarily in the molecular slip effects in an "infinitely" wide bearing. Thus, in his experiments, a taper-flat slider with a very large width to length ratio (about 2.0) was used. To study the rarefaction effects, the molecular mean free path of the air was increased by decreasing the ambient pressure. In

this manner, Tseng was able to run the wide slider bearing with ambient Knudsen numbers up to 2.4. It should be noted that this is far beyond the reported limits of the slip flow approximation. However, even though such high ambient Knudsen numbers were achieved, the effect of slip was negligible because the bearing performance was dominated by high compressibility (bearing) number effect. This is particularly evident when one examines Tseng's figure since his continuum theory curve and the slip-flow theory curve coincide at the high Knudsen number range. Nevertheless, Tseng was able to confirm that the slip flow approximation can predict the trailing edge clearance to within 10% of the actual value for Knudsen numbers up to 0.1 (slip flow regime). Tseng's study also found that a proper selection of the surface accommodation coefficient for air/disk and air/slider interfaces can greatly improve the theoretical predictions. Surface accommodation coefficient, σ, is defined as the fraction of gas molecules which are adsorbed when striking the wall and then reemitted with a random distribution in angle and velocity. Tseng found that if the surface accommodation coefficient is taken to be 0.89 instead of 1.0, a closer agreement between theory and experiment can be achieved. It should be noted that the value 0.89 used for the surface accommodation coefficient was the experimental value measured by Schaaf [30] for an air/glass interface for flows with low shear rates. In the bearing film, the shear rate is several orders of magnitude larger than those encountered by Schaaf in his studies. Whether the same value can be used is debatable. In the present study, the experiments have been used to help in the

determination of the best value for the surface accommodation coefficient for air/glass and helium/glass interfaces.

Only recently have experimental data become available for narrow slider bearings with width to length ratio of 0.1. The data were obtained by Sereny [33]. With a narrower bearing, the effect of slip is expected to be more pronounced. Similar to Tseng's work [35], Sereny studied the molecular rarefaction effect by increasing the mean free path of air via decreasing the ambient pressure. In his study, the effect of surface curvature (crown) due to lapping was considered because it was found that the crown could have considerable effect on the bearing performance. Figure 11-5 is a typical curve showing the effects of crown on the load and pitch angle calculations. As one can see, a convex crown (positive h_c) can significantly increase the load capacity while a concave crown (negative h_c) decreases the load capacity. Based on his experimental results, Sereny concluded that the slip-flow approximation completely fails to predict the rarefaction effects for ambient Knudsen number greater than 0.1. It should be noted that theoretical load/spacing curves plotted did not shift as the ambient operating pressure is reduced at constant disk velocity. This is not surprising since as the Knudsen number is increased by decreasing the ambient pressure, the operating bearing number is also increased by the same factor. Consequently, the additional molecular slip effect as the result of the increase in mean free path is offset by the increased high bearing number effect.

Figure 11-6 shows this offsetting effect which is illustrated by the fact that the slip flow curves for subambient pressures do not shift away from ambient pressure curve. Comparing figure 11-4 with figure 11-6, it is clear that by changing the mean free path while keeping the ambient pressure constant, more slippage effect could be observed.

Recently Kogure, Kaneko, and Mitsuya [21] reported their experimental findings on narrow slider bearings operating at "high" Knudsen numbers. They found excellent agreement between experiment and theory for Knudsen numbers up to 0.35. Unlike previous experimental investigations [33, 35], Kogure studied the increased molecular slip effect by decreasing the trailing edge clearance via reduction of the bearing width. Figure 11-7 is a typical curve showing the sensitivity of the load capacity to bearing width. In this manner, high bearing numbers encountered by Tseng [35] and Sereny [33] could be avoided. Kogure's study was limited to Knudsen numbers below 0.35 because the mean free path of air (0.069 µm) was not changed and the lowest trailing edge clearance achieved was about 0.2 µm. However, for Knudsen number range greater than 0.35, there is still no experimental data available to either prove or disprove the slip-flow approximation.

2.1 Measurement Techniques

Capacitance and optical techniques have been used successfully to measure the slider/disk separation. Brunner and his colleagues [4] used two capacitance probes imbedded in the slider to measure the bearing clearances

at two points on the slider. Knowning the surface contour, Brunner was able to determine the trailing edge clearance as well as the pitch angle of the slider bearing. It is not known whether the probes had any effect on the bearing performance. As the slider size was reduced, smaller and unshielded capacitance probes were used [3] to measure the slider flying characteristics. However, with the present slider design, neither the shielded nor the unshielded could be used because the probes are much larger than the slider itself.

Optical interferometric techniques have been successfully used to measure the gap between a moving magnetic tape and a static recording head [23, 18]. The interference fringe patterns can be produce by either a monochromatic light source or a white light. Lin and Sullivan [22] were the first investigators to successfully use white light to produce color fringes (known as Newton color rings) for measuring the trailing edge clearance of slider bearings. Later Tseng [35] also chose to use white light over monochromatic light to measure the slider trailing edge clearance. Recently Sereny [33] used two lasers (a CW He-Ne laser and a Variable Wavelength Pulsed Dye laser) to determine the clearance profile of the slider bearing. Since the optical measuring techniques gives a complete mapping of the slider clearance, Sereny also used this technique to measure the surface curvature (crown) on the "flat" portion of the taper-flat slider as well as the taper height.

There are advantages and disadvantages associated with the two techniques. For capacitance probes, the

advantage is that a real disk can be used in the experiments, while the disadvantage is that the imbedded probe can interfere with the bearing performance due to added weight or due to improper probe implantation. On the other hand, the advantage of the interferometric technique is that the slider is not altered in any way which could interfere with its performance, while the disadvantage is that the real disk must be replaced with a glass disk in order to allow the light to pass through and to creat the necessary optical interference. Slider flying characteristics can be different if the glass disk is used because the surface finish (roughness) on an actual disk is different from the glass disk. However, it is well accepted now that the interferometric technique is a reliable and accurate method for measuring small clearances.

2.2 Surface Roughness

As the bearing clearance is reduced, effects due to surface roughness on the slider and on the disk may become significant in addition to the molecular rarefaction effects. Roughness studies by numerous researchers [7, 14, 27, 34, 36] have shown that surface roughness can considerably influence the bearing performance. The roughness can be transverse, longitudinal, or striated relative to the direction of the flow. Rhow and Elrod [27] have shown that there is a general increase in the load carrying capacity due to striated roughness based on mean film thickness. However, a theoretical study based on Reynolds roughness by Christensen and Tonder [7] has shown that effects due to transverse or longitudinal

roughness are less pronounced in the case of narrow bearings (width to length ratio of 0.5) as compared to "infinitely" wide bearing. In the present study, sliders with width to length ratios of 0.15 or less are studied and surface roughness is not considered.

In the present experimental study, the molecular rarefaction effect predicted using the slip-flow approximation of the Reynolds equation is verified experimentally. Bearing clearance profiles and surface contour are measured interferometrically using two CW lasers - a Helium-Neon laser with wavelength of 632.8 nm and a Helium-Cadmium laser with wavelength of 441.6 nm. Experiments are performed with ambient Knudsen number varying from 0.04 to 2.5 without approaching excessively high bearing numbers. Bearing clearances as low as 0.075 μm with ambient mean free path of 0.188 μm have been measured. Excellent agreement has been found between experiment and slip-flow theory over the entire range of ambient Knudsen number, from 0.04 to 2.5.

3. THEORY

The classical treatment of the slider gas bearing problem is well known and has been thoroughly discussed in many lubrication texts [9, 15, 16]. The classical Reynolds equation is limited, however, to flows where the molecular mean free path of the gas is negligible compared with the dimensions of the flow passage, namely the slider bearing clearance. On the other hand, when the film thickness is much smaller than the molecular mean free path of the gas (i.e. rarefied gas flow), the problem is solved using kinetic theory analysis. However, if the flow is neither continuum nor molecular, the classical treatment is inadequate and kinetic theory analysis is too tedious. It has been shown from rarefied gas studies, both theoretically and experimentally, that the Navier-Stokes equation, together with slip velocity and temperature jump conditions, is adequate for analyzing flows in the so-called "slip-flow" or "transition" regime.

The first theoretical analysis of the rarefaction effect in gas lubrication was done by Burgdorfer [5]. The derivation of the modified Reynolds equation is identical to that for the classical Reynolds equation except for the boundary conditions at the walls (i.e. the slider surface and the rotating disk surface.) In addition to the standard Couette flow boundary conditions, a velocity slip is also assumed at all surface boundaries. The magnitude of the slip is approximated to the first order by the expression: (refer to coordinate system defined in Figure 11-2)

$$u_{slip}\big|_{wall} = f\frac{(2-\sigma)}{\sigma}\lambda\frac{\partial u}{\partial z}\bigg|_{z=wall} \tag{3.1}$$

where f - a numerical constant

   σ - surface accommodation coefficient

   λ - mean free path of gas

In equation (3.1), f is usually taken to be unity while σ can be less than or equal to unity, depending on the gas and boundary surface finish.   No temperature jump condition is needed since theoretical estimates of temperature difference between the bearing surface and the gas film show this to be negligible.

For the sake of simplicity, the modified Reynolds equation is usually written with σ and f equal to 1.   But if either parameter is not unity, the equation can be easily modified by introducing the factor $f(2-\sigma)/\sigma$ wherever appears.   The following steady-state modified Reynolds equation was derived by [5]:

$$\frac{\partial}{\partial x}\left[ph^3\frac{\partial p}{\partial x}\left(1+\frac{6\lambda}{h}\right)\right] + \frac{\partial}{\partial y}\left[ph^3\frac{\partial p}{\partial y}\left(1+\frac{6\lambda}{h}\right)\right] = 6\mu U\frac{\partial}{\partial x}(ph) \tag{3.2}$$

Nondimensionalizing the variables as defined in the Nomenclature, the resulting dimensionless form of equation (3.2) is written as follows:

$$\left(\frac{w}{T}\right)^2\frac{\partial}{\partial X}\left[PH^3\frac{\partial P}{\partial X}\left(1+\frac{6K_\infty}{PH}\right)\right] + \frac{\partial}{\partial Y}\left[PH^3\frac{\partial P}{\partial Y}\left(1+\frac{6K_\infty}{PH}\right)\right] = \Lambda\left(\frac{w}{T}\right)^2\frac{\partial(PH)}{\partial X}$$

$$\tag{3.3}$$

where K_∞ is the ratio of the ambient

mean free path to the minimum
bearing clearance (known as the
ambient Knudsen number)

Equation (3.3) is written in slightly different form
than the equation derived by [5] in that the ratio of the
slider width to the slider length is present. Instead of
the normal procedure of normalizing the y-dimension with
respect to the length, normalization is carried out with
respect to the width. For sake of completeness, the
derivation steps leading to equation (3.3) are outlined in
Appendix A.

If σ takes on values less than unity, equation (3.3)
is slightly modified with the parameter K_∞ being replaced
by $(2 - \sigma)K_\infty / \sigma$. For air/glass interface, it was found
by Schaaf [30] that a realistic value of σ is 0.89.
Moreover, Tseng [35] and Sereny [33] both have shown that
with σ equal to 0.89, a better agreement between
experiment and slip-flow theory can be achieved.

Equation (3.3) is a two-dimensional, non-linear,
second-order differential equation in P and cannot be
solved analytically for arbitrary slider geometry. But
several observations can be made by examining the
equation. One is that if the bearing number, Λ, is
sufficiently large and the width to length ratio is of
order 1, the right hand side of the equation will
dominate. The flow in the gas film is therefore Couette
dominant and molecular slip effects are negligible.
Another observation is that if the slider is very narrow
(width to length ratio $\sim$ 0.1), as is the case for the
present bearing geometry, the flow out the side edges will

be significant. Moreover, the criterion for "large" bearing number is now dictated by the new dimensionless parameter, Λ^* ($= \Lambda (w/l)^2$) , the "modified" bearing number. Thus for narrow bearings, the flow inside the gas film will not be Couette dominant until the modified bearing number, Λ^*, is sufficiently large. Therefore, until this limit is reached, the molecular slip effect in narrow bearings cannot be neglected even though the conventional bearing number is high.

The ability to obtain analytical solutions to any problem is important because it allows parametric analyses which can lead to better understanding of the problem. Simplification of the governing equation is one of the ways that can lead to analytical solutions. In gas bearings, the most common way to simplify equation (3.3) is to assume the bearing is infinitely wide. With this assumption, the equation becomes one-dimensional and can be easily solved for certain slider geometries. Burgdorfer was able to obtain closed form solutions for Rayleigh step bearings and plane slider bearings [5]. Perturbation techniques and asymptotic analysis have been used by various investigators to gain better insight into the problem. Asymptotic solution for infinitely wide slider bearings at high bearing numbers without slip have been obtained by numerous investigators [10, 11, 13, 17, 31]. Recently, Sereny obtained the one-dimensional asymptotic solution with slip at high bearing numbers [33]. Asymptotic solutions for finite width slider bearings at high bearing numbers without slip have been obtained by Elrod and McCabe [13] and Schmitt

and DiPrima [32].   However, an asymptotic solution for finite-width slider bearings at high bearing numbers with slip has not been developed thus far.

In order to design and develop new bearing systems, the full modified Reynolds equation, eq. (3.3), must be considered and the solution can be obtained only by numerical techniques.

4. NUMERICAL SOLUTION

The analysis of compressible lubrication films is complicated due to the non-linear nature of the governing equation, the well known Reynolds equation. The equation is further complicated by the introduction of molecular slip as the bearing clearance become comparable to the molecular mean free path of the gas medium. Analytical solution of the full modified Reynolds equation is impossible to obtain except for certain limiting cases discussed in the previous chapter. For real problems, the full equation must be considered and solved numerically.

Presently, there are two schools of thought on the type of numerical solution technique that should be used. The majority of the numerical solution are still based on the finite difference approximation of the governing equation. But in recent years, the finite element method, whose application had been limited mainly to structural analysis, has been applied to lubrication problems (as well as other fluids and heat transfer problems.)

Several papers have been published recently which focused on the application of the finite element technique in solving the Reynolds equation [2, 25, 26]. The finite element method has one distinct advantage over the more commonly used finite difference method; as the former is able to handle irregular shape boundaries without major modifications to the computer code. This versatility is attributed to the fact that irregular shapes can always be approximated by patch work of polygonal elements. However, both Booker and Huebner [2] and Reddi and Chu [26] are careful to point out that, in terms of computer

time, the finite element method may not be better (sometimes even worse) than the finite difference method. Reddi and Chu [26] also noted that it is very difficult to compare the two techniques on the same level since the solution techniques for solving the resulting matrices are different.

The most often used numerical technique to solve the full compressible Reynolds equation is still the finite difference method. Castelli and Pirvics [6] summarized in their paper the state of the art of numerical solution methods as it existed in 1969. Since that time only a few papers [8, 37, 12] have focused on the numerical solution techniques as applied to the Reynolds equation. The finite difference method is divided into two distinct parts - discretization of the Reynolds equation and the solution of the resulting set of algebraic equations.

All numerical solution methods require the representation of the dependent variable at a finite number of points defined by the intersection of a grid mesh. The distribution of grid lines should be such that they fall on all boundaries and clearance discontinuities. Furthermore, if there are sharp pressure gradients anywhere in the bearing, special grid distribution is required. For the taper-flat slider bearing, sharp pressure gradients exist at the break and at the trailing edge and denser grid mesh is need at these two regions in order to assure accurate solution and numerical stability. These sharp gradients are caused by the presence of small boundary layers and these boundary layers have been estimated to be on the order of $1/\Lambda$ [10, 11, 13, 31, 32].

For finite width bearings, if the bearing number is sufficiently large, a side boundary layer of the order $1/\sqrt{\Lambda}$ [13, 32] will be present at the edges causing a large pressure gradient in the region and a finer grid mesh will be required at the side edges of the slider for numerical stability.

Until recently, all finite difference algorithms that have been developed [6, 37] require the use of variable grid mesh when the bearing number is large. However, a new algorithm has been developed by H.G. Elrod [12] which does not require the use of variable grid spacing in order to insure numerical stability. Because constant grid mesh can be used, this new algorithm is much faster than any previous algorithm in terms of computer time. The original algorithm developed by Elrod has not been published. In this investigation a similar algorithm was formulated using the exponential approximation method developed by Elrod [12]. The formulation of this "new" algorithm is outlined in Appendix B.

In this study, two different discretization methods are used. One is the integral discretization technique developed by Castelli and Pirvics [6]. The details of this technique can be found in Reference [6]. Basically for integral discretization, a finite difference approximation is applied to equation (3.3) after the equation has been integrated once over each grid cell using Gauss' theorem (for transforming surface integral to line integral). It was shown by Sereny [33] that integral discretization is superior to the differential discretization in that it is less dependent on the size of

the grid mesh and provides the necessary conservation of mass. The other discretization method used is the exponential approximation method developed by Elrod [12].

Once the Reynolds equation is discretized, one algebraic equation is written for each grid point resulting in a system of algebraic equations. The system can then be solved by various numerical techniques. Two implicit schemes are used - Column Method and Alternating Directional Implicit method (ADI). The so-called Column Method is described in detail in reference [6].

In the beginning of this investigation, experimental results are compared with theoretical predictions using the integral discretization techniques. But later the exponential approximation method is used for all the predictions. Both Column Method and ADI were used with each discretization method and their results checked with each other. In addition, the efficiency in terms of computational time of each algorithm are also compared.

5. DESCRIPTION OF THE EXPERIMENTAL APPARATUS

The measurement of film thicknesses on the order of 0.25 µm or less requires a clean and vibration free environment. In addition, close tolerances on the measured quantities - bearing clearance profile and load - must be maintained. An experimental apparatus meeting such requirements is used in the present investigation. The apparatus was originally designed and built by Sereny [33]. Two major changes have been made to the experimental set-up. First is that the Variable Wavelength Pulsed Dye Laser has been replaced with a Continuous Wavelength (CW) Helium-Cadmium Laser. It was found that the Pulsed Dye laser was too unreliable and the lasing wavelength of the dye solution used in the laser could not be determined accuratetly. The accuracy in determining the bearing clearance profile is highly dependent on knowing the wavelength of the two lasers used. Second is that the test chamber has been instrumented with a gas analyzer to measure the concentration of different gas media which may be introduced into the chamber. Only gases with sufficiently different thermal conductivity than air can be used.

The experimental apparatus consists of two major components - a sealable but controllable test chamber and an optical bench. Figure 11-8 is a schematic diagram of the experimental set-up.

5.1 Test Chamber

The test chamber is divided into upper and lower sections by a dividing plate. The variable speed D.C. motor and the belt drive mechanism are housed in the lower

chamber while the actual bearing test environment is located in the upper chamber. This is done to prevent contaminants from the motor and belt drive from entering the test area. The entire test chamber can be sealed so that the inside environment can be controlled such that the mean free path can be changed. There are two ways to change the mean free path inside the test chamber. The first method is to reduce the chamber pressure since the mean free path of a gas is inversely proportional to the pressure. Alternatively, the gas inside the chamber can be changed to another one that has a different mean free path. For example, helium has a mean free path that is 2.5 times greater than air while the viscosity of the two gases differ only by ten percent. In the present investigation, even though the apparatus was originally designed to operate at subambient pressures, the second method is used because the molecular slip effect is more pronounced if the mean free path can be increased without changing the ambient pressure. Comparison of Figures 11-4 and 11-6 clearly shows the superiority of the second method. It should be noted that even though in Figure 11-4 the curves are for air, it is still applicable for helium because the viscosity of the two gases do not differ significantly.

The upper and lower chambers are connected only through a valve. When the test chamber is sealed for helium experiments, this valve is opened to allow helium, which is forced fed into the upper chamber, to flow into the lower chamber before exiting the test chamber. In this manner, there is always a flow from upper to lower

chamber which helps to prevent dust in the lower chamber from migrating up to the upper chamber.

In the upper chamber, a 4.45 cm thick optical-flat disk with a 25.4 cm O.D. is mounted at its inner diameter (4.6 cm I.D.) to a precision ball bearing spindle. The disk has a surface flatness of 1/20 of the He-Ne laser wavelength of light used and is dynamically balanced to within 2.5 μm peak to peak.

The slider bearing used in this study is of the IBM "Winchester" design. Basically, the slider has a two-rail taper-flat configuration and is made of ferrite material. A sketch of the Winchester slider is shown in Figure 11-3. The nominal length associated with the slider of this type is 5.6 mm with a projected taper length of 1.27 mm. The nominal taper angle is about 8.7 milli-radians (half a degree). In this study, the nominal width of the rail varies between 0.38 mm and 0.89 mm.

The slider head is aligned and glued onto a gimbal spring suspension system which is capable of applying a 10 gram load on the slider. The load is applied through a load point called the pivot point. The spring is designed such that very little moment is created about the pivot point when the slider pivots. Figure 11-9 is a photograph showing the gimbal spring with the slider mounted. The slider-spring assembly is clamped to one end of the cantilever beam while the other end of the beam is fixed onto a precision stage with five degrees of freedom - three rotation and two translation. With this mounting scheme, the yaw and roll angles of the slider can be

adjusted or biased.

The external load on the slider can be varied through the use of a variable loading mechanism. The mechanism consists of a loading button glued onto a rubber diaphragm which is mounted on top of a small gas chamber. The mechanism is strategically located under the slider-spring assembly such that when the small gas chamber is pressurized, the diaphragm expands causing the loading button to protrude and to push against the slider at the pivot point. The force applied to the slider is determine by measuring the strain on the cantilever beam to which the slider assembly is attached. The beam or arm is made of Delrin material[1] and is instrumented with four strain gages. Figure 11-10 shows the entire arm assembly. The arm is calibrated with dead weights and the strain rate of change per gram was found to be 10.5 μm/m/gram for loads between 10 and 30 grams. Figure 11-11 shows the typical calibration curve for the arm at 20°C. It has been found that the calibration curve is sensitive to ambient temperature. Since the experiments are performed in an air-conditioned laboratory, close control of the ambient temperature was maintained.

A constant temperature hot-wire anemometer is used as a gas analyzer to measure the helium gas concentration inside the test chamber. Helium was selected for several reasons. One is that the mean free path of helium is much larger than air (0.188 μm vs 0.069 μm). Another reason is

---

[1]Delrin is registered trademark of Du Pont

that the thermal conductivity of helium is significantly different (about eight times higher) than air. Thus when helium is introduced into the test chamber, the hot-wire anemometer can easily detect its presence. The hot-wire probe is calibrated inside a vacuum bell jar. The voltage response of the probe versus the helium concentration is plotted in Figure 11-12. The mean free path curve on the figure is obtained using the theoretical formula for mixtures given in Reference [29]. Therefore, once the probe voltage response is measured, the helium concentration and the mean free path of the helium/air mixture are easily determined using the calibration curve. Viscosity of the gas mixture can also be calculated using the theoretical mixture formula given in Reference [29]. It should be noted that the highest purity research grade helium is used in the experiments. The helium is also filtered before it is force fed into the test chamber. The hot wire probe is mounted in the upper chamber and is shielded from the gas motion inside the chamber caused by the rotating disk. Probe responses obtained when the disk is still and when it is rotating showed no difference. For all the experiments, the test chamber was filled with 100% helium.

The entire test chamber is located in front of the laminar flow bench in order to prevent particulate contamination from the room when the unit is opened. In addition, before any experiments are performed, the upper chamber is purged with clean air which has been passed through a "clean air" filter.

5.2 Optical Bench

The optical bench used to measure the bearing
clearances is separated from the test chamber. The
optical bench consists of two monochromatic light sources
of different wavelength, a beam splitter, 3 mirrors, beam
expander, focusing lens, and an imaging system. A
schematic of the interferometric set-up is shown in Figure
11-8. Two CW lasers are used to generate the needed
interference fringe patterns. The lasers include a
Helium-Neon laser with a wavelength of 632.8 nm and a
Helium-Cadmium laser with a wavelength of 441.6 nm. Since
the final approach path taken by the two laser beams must
be the same, and since the lasers cannot be placed
collinear with each other, the beams are made collinear
via a mirror/beam splitter set-up as shown in Figure 11-8.
Once the beams are collinear, they are expanded to about
1.25 cm in diameter via a beam expander. Due to the path
length difference between the beam reflected from slider
surface and that reflected from the bottom surface of the
glass disk, distinct optical interference pattern is
observed for each of the two lasers. These fringe
patterns are then enlarged ten-times and focused onto a
Polaroid film back where black and white photographs are
taken for each laser. Typical photographs of the fringes
are shown in Figure 11-13. With only minor adjustments,
the present optical arrangement can also be used with
white light (similar to Lin's work [22]).

6. EXPERIMENTAL MEASUREMENTS

6.1 Slider Dimensions

The slider bearings used in this experimental study are the IBM "Winchester" type flying heads found in magnetic disk memory packs. Figure 11-3 shows a sketch of the slider. The slider is made of sintered ferrite with its two skates lapped to a very smooth surface finish.

The physical dimensions of the slider are obtained by two measuring techniques. An optical (machinist) microscope with 10X magnification is used to measure the overall dimensions of the slider head and its skates. These dimensions include the length and width of the slider head, the length and width of each rail, and the projected ramp length of each rail. In addition, the microscope is also used to measure the location of the load point (pivot point). Table 11-1 shows the dimensions for all the various sliders used.

Interferometric techniques are used to measure the taper (ramp) height and surface crown heights because they are too small to be measured by the microscope. Both quantities are obtained after examining the interference fringe photographs taken during actual experiments. The ramp height is determined by counting the number of dark fringes appearing across the ramp. Like all the other dimensions, the ramp height varies from slider to slider as shown in Table 11-1. Using interferometry, the ramp height can be determined to within one-half the laser wavelength; that is, for He-Cd laser, the error is only about 0.22 μm out of 9.0 μm.

On the other hand, the crown height on the slider skate is slightly more difficult to determine from the interference fringe photographs. Several assumption are made before the crown can be determined. One is that the crown, when present, is parabolic in shape with its vertex located at the center of the "land" section of the skate. The crown may be either concave or convex relative to the flat slider and is easily determined by examining the manner in which the fringes are distributed along the skate. Figure 11-15 illustrates the differences among the three surface contours - concave, flat, and convex. As illustrated, for a concave crown, the separation between consecutive fringes becomes larger as the distance from the trailing edge increases; for a "flat" surface, the separation remains constant; and for a convex crown, the separation becomes smaller. Another assumption made is that the crowns on the two skates do not necessarily have to be the same in magnitude or concavity. The last column in Table 11-1 shows how the two crowns can vary on each slider head. Furthermore, it is also assumed that the crown does not change in shape or in magnitude within the load range tested (from 10 grams to 30 grams). Finally, it is assumed that there is no crown across the width of the skate.

In order to reduce the error in determining the crown height, the procedure is computerized. In a previous study [33], the crown height was determined manually by fitting an assumed crown profile through data points from only one experiment. Crown shape and height were also assumed to be the same on both skates. However, in the

present study, the crown concavity and height are determined based on all the experimental data for the particular slider (usually from over 20 experiments). Since the crown determination is directly related to the determination of the flying profile, the exact crowns are determined only when the flying profile is determined for each experiment. The exact procedure is discussed in the following section.

6.2 Flying Profile

With the present experimental measuring technique, the actual flying profile of the slider can be determine with great accuracy. The procedure used to determine the profile is computerized in order to minimize the error in data reduction. The Method of Least Squares is used to determine the trailing edge clearance, the pitch angle, and the roll angle for a given slider and crown profile. The data reduction procedure is outlined in Appendix C.

Different combination of the crown profiles for the two skates are used as input for the computer fitting routine and the combination that best fits the experimental data for all the runs (that is, gives the least (squares) error in fitting) determines the crown profiles on the slider. Moreover, once the best crown profile combination is established, the "experimental" flying profile is also determined for each experiment. This new data reduction procedure is more accurate than the previous method used [33] because the procedure uses all available experimental data. Furthermore, the flying profile determined as well as the crown are mathematically the best for the given data.

It has been determined that an inaccurate crown determination will lead to an inaccurate flying profile determination. With this new procedure, a ± 0.025 μm accuracy or better can be achieved in determining the trailing edge clearance. With the slider bearing expected to operate at less than 0.125 μm minimum film thickness, an error of more than 0.025 μm can lead to significant errors in the numerical solution. Previously, the best accuracy attained was no better than ± 0.050 μm.

7. EXPERIMENTAL RESULTS AND COMPARISON TO THEORY

In this investigation the performance of Winchester type heads of different rail width - 0.38 mm, 0.51 mm, and 0.89 mm - were studied. The physical dimensions of the these sliders are summarized in Table 11-1. The three types of slider were tested in both normal ambient conditions (i.e. air at room conditions) and in a pure helium environment. Whenever possible, the same slider is used in both gas media. However, this was not possible in most cases because the slider has the tendency to "crash" at high loads and low clearances due to dust contamination. Only the wide head (0.89 mm wide) did not crash. Crash is defined as the slider surface being scratched by dust trapped in the gas film. The slider will still "fly" but no data can be taken because the scratched slider surface makes the interference fringes impossible to identify. Figure 11-16 shows what happens to the fringes when the slider "crashes". (Note the streaking along the length of shoe B.)

Each type of slider was tested at various velocities between 17 to 52 m/sec with loads between 8 to 30 grams. The clearance profile for each operating condition is determined using the method of least squares for fitting the experimental data as describe in Appendix C. The experimental results are then compared with numerical solutions of the modified Reynolds equation.

The theoretical prediction are based on actual physical dimensions of the slider and not on the nominal design values. Gas properties of air and helium are assumed to be constant throughout the experiments; that is

air and helium viscosities are taken to be 18.27 Pa-s and
19.50 Pa-s, respectively, while the air and helium mean
free paths are taken to be 0.069 μm and 0.188 μm,
respectively. The ambient pressure needed for calculating
the theoretical load is taken to be 101.4 kPa.

There are two methods by which the results can be
compared. The first method is to compare the accuracy of
the predicted trailing edge clearance and experimentally
measured clearance for a given load. With this approach,
the pivot position of the slider is assumed to be known.
Armed with this assumption and a starting reference
clearance (usually it is the trailing edge clearance), the
computer program proceeds to solve for the flying profile
whose center of pressure coincides with the pivot point.
The program also calculates the load associated with the
profile. In theory, if the load does not correspond to
the given load, the program will change the reference
clearance and repeat the calculations until both the load
and pivot point requirements are satisfied. In practice,
this type of iterative scheme is not used because enormous
an amount of computational time is needed to solve just
one case. Instead, the program will generate a load
versus trailing edge clearance curve for fixed pivot
point. Thus, to determine the theoretical clearance for a
given load, one only has to go to the curve. Associated
with the load/spacing curve is a pitch/spacing curve. In
this investigation, the measured and the predicted pitch
angles is also studied.

The second method is to compare the predicted load
and the predicted center of pressure for given flying

profile (i.e. specify the trailing edge clearance and the pitch angle).

The experimental curves for the load/spacing and pitch angle/spacing characteristics of the three different width sliders in air and helium are presented in Figures 11-17 to 11-32, Figures 11-33 to 11-50, and Figures 11-51 to 11-62. Also plotted on these figures are the numerical solutions of the modified Reynolds equation. All the theoretical curves are for a surface accommodation coefficient of 0.89, unless otherwise indicated. No roll angle/spacing characteristics were plotted because very small roll angles were encountered even when the two shoes on the sliders have different surface curvatures. Furthermore, even if there was a small roll angle, the predicted load and pitch did not differ by more than 5% when the roll angle was taken into account. Since three different width sliders were tested, in order to avoid confusion, the sliders are classified into three categories according to their widths - narrow, standard, and wide.

7.1 Narrow Sliders

Narrow sliders were tested in air and helium at various disk velocities. The slider used in the air experiments was not used in the helium experiments because it had crashed at the end of the air runs. Another slider of the same nominal dimensions was used in helium. Figure 11-17 and 11-18 show the typical experimental load/spacing relationship for the narrow sliders in air and helium, respectively, at the same disk velocity. For each load/spacing plot, there is a corresponding pitch

angle/spacing plot. Figures 11-19 and 11-20 show the pitch/spacing characteristics for the two cases presented in Figures 11-17 and 11-18, respectively. All theoretical curves are based on surface accommodation coefficient of 0.89 for both air and helium cases, unless otherwise indicated.

Several important observations can be made from examining Figures 11-17 and 11-18. To illustrate the effects of molecular slip, theoretical curves based on continuum theory and slip flow theory are plotted on the two figures. As the figures clearly indicate, the main effect of slip is to decrease the load carrying capacity of the slider bearing since the slip theory curve always lies below the continuum theory curves. Furthermore, it is observed that the effect of slip is greater in helium than air demonstrated by the fact that the separation between slip theory curve and continuum theory curve is greater in helium than in air. This is attributed to the fact that the mean free path of helium is much larger than that of air. In addition, the two figures also show that even though the conventional bearing number (indicated by the upper scale on the figure) is of the order 10^3 to 10^4, the effects of slip and side leakage cannot be neglected. If the high bearing number effect had dominated, the slip-flow theory curves and the continuum theory curves would have coincided, as was the case reported by Tseng [35]. At first this may seem to be a surprising result. However, if the modified bearing number as defined by equation (11.24) is used, it is obvious that the bearing is far from approaching the high "bearing" number range.

In fact, for the narrow slider, the modified bearing number is only on the order of 10^1 to 10^2.

Figures 11-17 and 11-18 also show the effect of different values of surface accommodation coefficient, σ, on the theoretical predictions. Two values of σ were used - 1.0 and 0.89. As the figures show, slip theory with $\sigma = 0.89$ gives a slightly better agreement with experiment for both air and helium. The surface accommodation coefficient for air/glass interface was measured to be 0.89 [30], and Tseng [35] has shown that when σ is taken as 0.89, a better agreement between theory and experiment can be achieved for air. However, there is no published data on σ for helium/glass interface. In this investigation, different values of σ were tried and it was found that when σ is equal to 0.89 a good agreement between experiment and theory can be achieved.

Further examination of Figures 11-17 and 11-18 shows that as the clearance is decreased by increasing the external load, the agreement between experiment and theory does not deteriorate even though the ambient Knudsen number is increased from 0.1 to 0.38 for air and from 0.6 to 1.14 for helium. But, it should be noted that much closer agreement is found for helium experiments than for air runs. Moreover, for air, Figure 11-17 also shows some departure between experiment and slip-flow theory at lower spacings. It is believed that helium results are better than air because helium is monatomic while air is a mixture polyatomic gases. Thus the ideal gas assumption and the slip flow approximation used to derive the

modified Reynolds equation may be more applicable for helium than for air, especially up in the higher Knudsen number ranges.

Examination of Figures 11-19 and 11-20 shows that the slip flow theory with $\sigma = 0.89$ is also able to predict with accuracy the pitch angle of the slider bearing operating in air and helium.

Results for the narrow slider at other operating conditions are presented in Figures 11-21 to 11-26 and Figures 11-29 to 11-32 for air and helium, respectively. It is clear from examining these figures that slip flow theory with $\sigma = 0.89$ is able to predict with accuracy the bearing performance over a wide range of bearing numbers and for high ambient Knudsen numbers.

7.2 Standard Sliders

Experimental results for the standard slider operating at various velocities in air and helium are presented in Figures 11-33 to 11-38 and in Figures 11-39 to 11-50, respectively. Once again, slip flow theory with $\sigma = 0.89$ seems to give the best predictions for both air and helium cases. Furthermore, it is found that slip flow approximation does not fail even when the ambient Knudsen number is much larger than 1.0. In particular, Figure 11-39 shows that the slip flow theory is able to accurately predict the load/spacing characteristics of the slider bearing even down to a trailing edge clearance of 0.075 μm with the ambient Knudsen number of 2.5. It should be noted that this agreement is not due to the high bearing number effect because, once again, the continuum

theory curve and the slip-flow theory curve do not coincide as shown by Figure 11-39.

It should be noted that, similar to the narrow slider, the agreement between experiment and theory is better for helium cases than for air. Moreover, the departure between experiment and theory for clearances below 0.25 µm - which was found in the narrow slider results for air - is also present in the standard slider air results.

Once again, Figures 11-36 to 11-38 and Figures 11-45 to 11-50 show that the slip flow theory with σ = 0.89 can also predict with accuracy the pitch angle of the standard slider in air and in helium, respectively.

7.3 Wide Sliders

Experimental results for the wide slider operating at various velocities in air and in helium are presented in Figures 11-51 to 11-53 and Figures 11-57 to 11-59, respectively. The same slider head was used in air and in helium experiments. Once again, the slip flow theory with σ = 0.89 seems to give a better agreement between experiment and theory for both air and helium. However, the experimental results for the wide head are more scattered than those for either the narrow or the standard heads. This scatter can be explained by the fact that the surface on the wide head is very irregular and the surface profile assumed for data fitting was only a rough approximation of the real contour. This deficiency is more evident when comparing the measured pitch with predicted pitch. Figures 11-54 to 11-56 and Figures 11-60

to 11-62 show the inability of the theory to predict the slider pitch angle for both air and helium. It must be noted that this failure is due to the inability to account for the surface irregularities and not due to failure of the slip-flow model because the ambient Knudsen numbers are all below 0.1.

Comparing the load/spacing results from the three different width sliders, one sees that the wide slider operates at much higher clearances than the narrow slider even though the width of the wide bearing is only twice that of the narrow bearing.

8. DISCUSSION

Results presented in the previous chapter clearly indicate that the modified Reynolds equation with slip flow approximation can predict correctly the reduction in load capacity of finite width slider bearings. In addition, the slip-flow theory can also predict accurately the flying pitch angle. The agreement between experiment and slip flow theory is excellent for low ambient Knudsen numbers $(K_\infty < 0.1)$, moderate Knudsen numbers $(0.1 < K_\infty < 0.5)$, and high Knudsen numbers $(0.5 < K_\infty < 2.5)$. It is somewhat misleading to use the ambient Knudsen number as the measure for molecular slip effect because the mean free path of the gas inside the gas film is smaller than the ambient value due to the fact that the local pressure is higher than the ambient pressure. Thus, the local Knudsen number, K_1, based on local values of mean free path and clearance would give more insight into the molecular slip effect. Figure 11-63 and Figure 11-64 are typical contour plots of constant local Knudsen numbers for the narrow slider in air and standard slider in helium, respectively. As the figures clearly show, in terms of local Knudsen numbers, most of the bearing is still dominated by relatively high local Knudsen numbers. Based on these typical plots of local Knudsen numbers, it is clear that the effect of molecular slip is still substantial even with bearing numbers of 6090 and 19308 for the two cases shown, respectively.

In this investigation, the effect of slip has been successfully studied without becoming concerned with high bearing number effect. Had the bearing number been large,

the effect of slip would be diminished. Moreover, there would be a small boundary layer at the side edges of the slider. To show that high bearing number limit is not reached even though the conventional bearing number is large for most of the experimental runs, pressure profiles across the slider bearing are plotted for different points along the length of the bearing. Figure 11-65 and 11-66 are typical plots of the pressure profiles across the bearing for the narrow slider in air and for the standard slider in helium, respectively. The conventional bearing number for Figure 11-65 is 6091 and for Figure 11-66 is 19308. It is clear that neither of the pressure profiles exhibit any sign of a boundary layer at the side edges because there are no sharp pressure gradients near the edges.

In this investigation, the agreement between experiment and slip-flow theory is consistently better for helium results than air results. It is believed that this phenomenon is caused by the fact that helium is a monatomic gas while air is a mixture of polyatomic gases. Thus the slip-flow theory derived on the assumption of ideal gas may be more applicable for helium than for air especially in the higher Knudsen number range, i.e. in transition flow regime. It was noted by Bird [1] that if a gas flow is in local thermodynamic equilibrium, the question of whether it is a simple gas or gas mixture is of no consequence. Bird also asserted that in transition flow, a gas mixture may be initially in uniform composition, but species separation may occur due to thermal or pressure diffusion. Whether this separation is

present in the present study is not known. A more comprehensive analysis of this phenomenon is needed in order to fully understand why helium results are better than air results.

From examining the load/spacing characteristic curves, it appears that slip flow theory can be made to agree better with the experimental data by choosing the surface accommodation coefficient, σ, to be 0.89 for both air/glass and helium/glass interfaces. Since the surface accommodation coefficient is directly related to the surface finish of the solid surface, one could, perhaps, interpret this coefficient as a crude measure of surface roughness with amplitude of less than one mean free path of the gas. For diffuse surface like a rough surface, the molecules hitting the surface are fully accommodated and $\sigma = 1.0$. On the other hand, if the surface is not totally diffuse like a shinny surface, the molecules hitting the surface are reflected specularly and diffusely and $\sigma < 1.0$. Therefore, if the predictions are plotted for two values of σ, the curve for lower value of σ would lie below the higher value of σ as shown in Figure 11-17. Thus in terms of "roughness", the smoother-finish (shinny) surface corresponding to the lower value of σ would carry less load than the rough surface corresponding to the higher value of σ. This result is similar to that obtained through formal treatment of surface roughness. It should be noted that this is only an interpretation of surface accommodation coefficient in terms of surface finish.

The agreement observed between experiment and theory

also suggests that the numerical scheme used to solve the Reynolds equation is both reliable and accurate. In this investigation, several different numerical algorithms were used to solve the modified Reynolds equation; for example, integral discretization method with variable grid and exponential approximation with constant and variable grids. The variable grid used in the numerical algorithms is dependent on the operating conditions and is describe in Appendix E. All the algorithms used the Column Method of solution for solving the system of equations resulting from the finite difference approximation. The purpose of this exercise was to determine the most efficient algorithm, in terms of solution accuracy and computational time, for solving the modified Reynolds equation. Table 11-67 shows the comparison of the three algorithms used. It is quite clear from Table 11-67 that the slowest but very accurate algorithm is the integral discretization method with variable grid while the fastest but not very accurate algorithm is the exponential approximation with constant grid. But the exponential approximation with variable grid is both fast and accurate. It is 60 percent faster in computational time and is within 2% of the predicted results (load and pitch angle) when compared with the integral discretization method with variable grid. It should be noted that variable grid is used in the exponential approximation method to improve solution accuracy and not for numerical stability.

Numerical algorithms using the Alternating Directional Implicit (ADI) scheme to solve the system of equations resulting from two discretization methods -

integral discretization and exponential approximation -
were also examined because in general algorithms using ADI
technique is usually faster than other schemes using
matrix inversions like the Column Method. To add
stability to the ADI scheme, the time dependent term in
the Reynolds equation, $\frac{\partial (PH)}{\partial T}$, is retained and the problem
is solved as a transient one. The Peaceman-Rachford ADI
method [28] was used and is outlined the Appendix D. In
this study, Successive Line Relaxation method with
Alternating Direction was also used and is also discussed
in Appendix D.

For algorithms using integral discretization
technique, it was found that the ADI solution scheme was
much slower than the Column Method because the size of the
time step was limited by the smallest grid spacing used.
It was found that for each problem there was an optimal
size for the time step with which a stable steady state
solution can be obtained with the minimum amount of
iterations. Therefore, if the time step was too large,
the algorithm would become unstable and no solution could
be obtained; on the other hand, if the time step was too
small, the algorithm would take forever to reach the
steady state solution. However, for the test case
studied, even with the optimal time step, the ADI scheme
was still slower than the Column Method.

It has also been found that algorithm using the
exponential approximation technique with ADI was extremely
unstable for both constant and variable grids. The
algorithm was found to be stable only when the time step
was at least two orders of magnitude smaller than that

needed for the algorithm using integral discretization with ADI. Once again, there seemed to be an optimal time step. However, if Alternating Directional Successive Line Relaxation method was used with the exponential approximation technique, the algorithm was found to be unconditionally stable for any size time step with either constant or variable grid spacing. However, even for an infinite time step, the algorithm was found to be still several seconds slower than same algorithm with Column Method.

9. GENERAL REMARKS AND RECOMMENDATIONS

The validity of the modified Reynolds equation with slip flow approximation has been verified over the entire range of Knudsen numbers between 0 and 1.0.

Nevertheless, the author believes that additional research is need in the following areas:

* Determine the reasons why helium results are better than air

* Develop faster numerical algorithms for solving the modified Reynolds equation

* Determine the extent of surface roughness effects in narrow bearing systems

10. NOMENCLATURE

h	Film thickness
h_t	Trailing edge film thickness
h_{min}	Minimum film thickness
h_r	Ramp height
h_c	Crown height of slider shoe
H	Dimensionless film thickness ($= h/h_{min}$)
H_t	Dimensionless trailing edge film thickness ($= h_t/h_{min}$)
K	Knudsen number ($= \lambda/h$)
K_∞	Ambient Knudsen number ($= \lambda_a/h_{min}$)
K_1	Local knudsen number ($= \lambda_1/h$)
l	Length of slider
l_r	Ramp length (projected)
l_{piv}	Pivot point location (measured from the trailing edge)
p	Pressure
p_a	Ambient pressure
P	Dimensionless pressure ($= p/p_a$)
Q	Linearized variable ($= P^2 H^2$)
w	Width of slider shoes
U	Linear velocity of disk
U_x, U_y	Components of velocity in x,y directions, respectively
x	Spatial coordinate in length direction
y	Spatial coordinate in width direction
t	Time
X	Dimensionless spatial coordinate along the length ($= x/l$)
Y	Dimensionless spatial coordinate along the width ($= y/w$)
W	Load
μ	Viscosity of gas

ΔX_i	$i\underline{th}$ grid spacing in X direction
ΔY_j	$j\underline{th}$ grid spacing in Y direction
λ	Wavelength of monochromatic light source or molecular mean free path of the gas
Λ	Bearing number based on trailing edge clearance, ($= 6\mu U l / p_a h_t^2$)
σ	Surface accommodation coefficient
f	Numerical constant (usually set equal to 1)

Subscripts:

a , ∞	ambient conditions
i,j	x,y index of grid point, respectively
t	trailing edge
r	ramp region
l	local conditions or values
min	minimum value
piv	pivot point
c	crown
x,y	x,y components of vector quantity

11. FIGURES AND TABLES

TABLE 11-1: MEASURED DIMENSIONS OF SLIDERS TESTED

HEAD ID	l (mm)	w (mm)	l_r (mm)	D (mm)	h_r (μm)	x_{piv} (mm)		h_c (μm)
PA3	5.552	0.419	1.135	2.718	10.12	2.41	A	0.051
							B	0.051
PA1	5.500	0.381	1.138	2.718	9.81	2.46	A	0.064
							B	0.102
R2	5.537	0.521	0.965	2.515	8.26	2.54	A	-0.051
							B	0.000
R4	5.542	0.513	1.062	2.515	8.29	2.44	A	-0.025
							B	0.025
R1	5.555	0.513	0.947	2.515	8.24	2.44	A	0.051
							B	0.114
Y2	5.570	0.531	1.092	2.548	12.02	2.54	A	-0.064
							B	-0.051
W2	5.512	0.850	0.813	2.261	9.24	2.49	A	0.191
							B	0.152
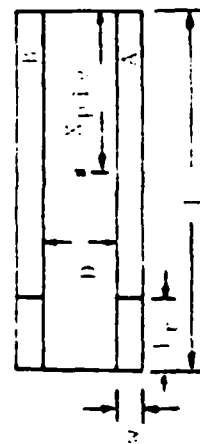
* not drawn to scale *
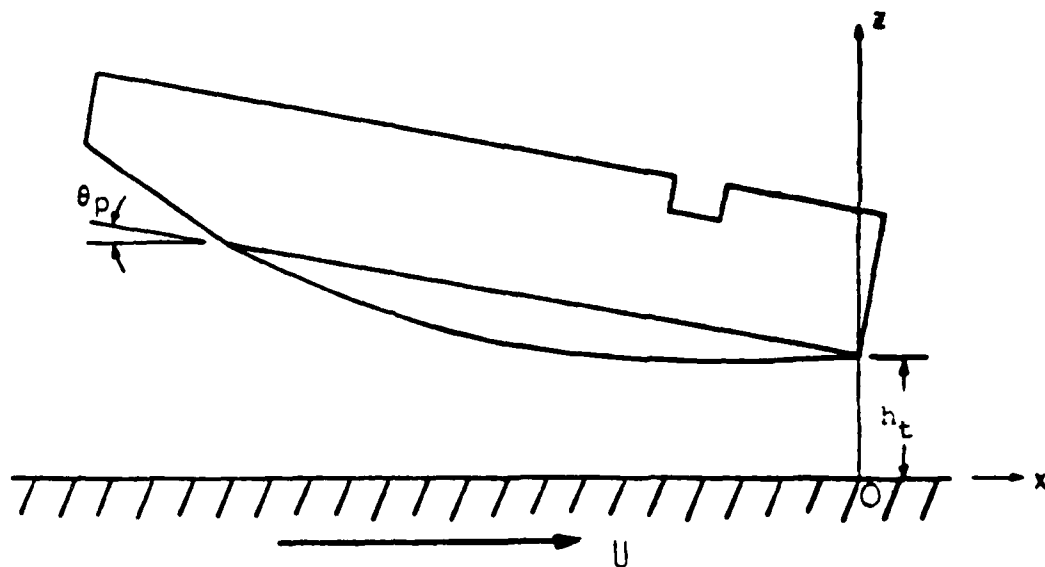
(a) SIDE VIEW
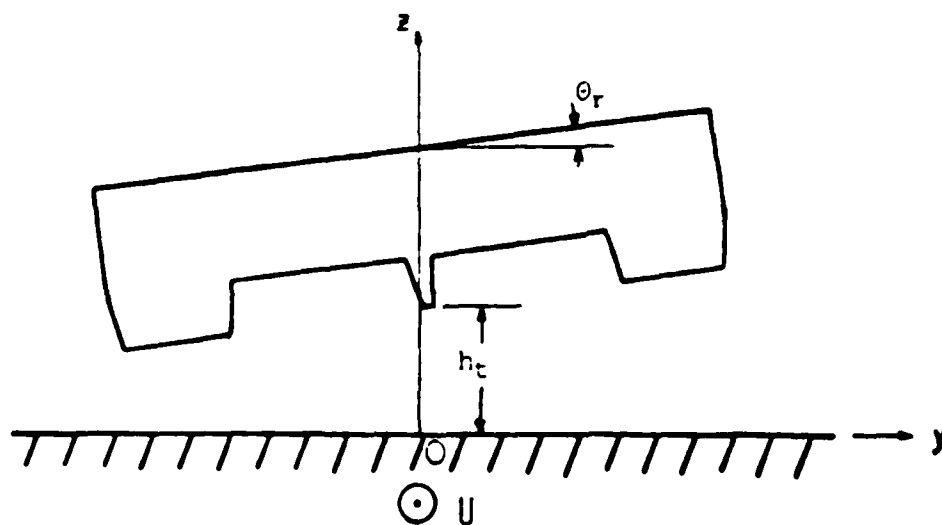
(b) END VIEW

FIGURE 11-2: PHYSICAL SITUATION
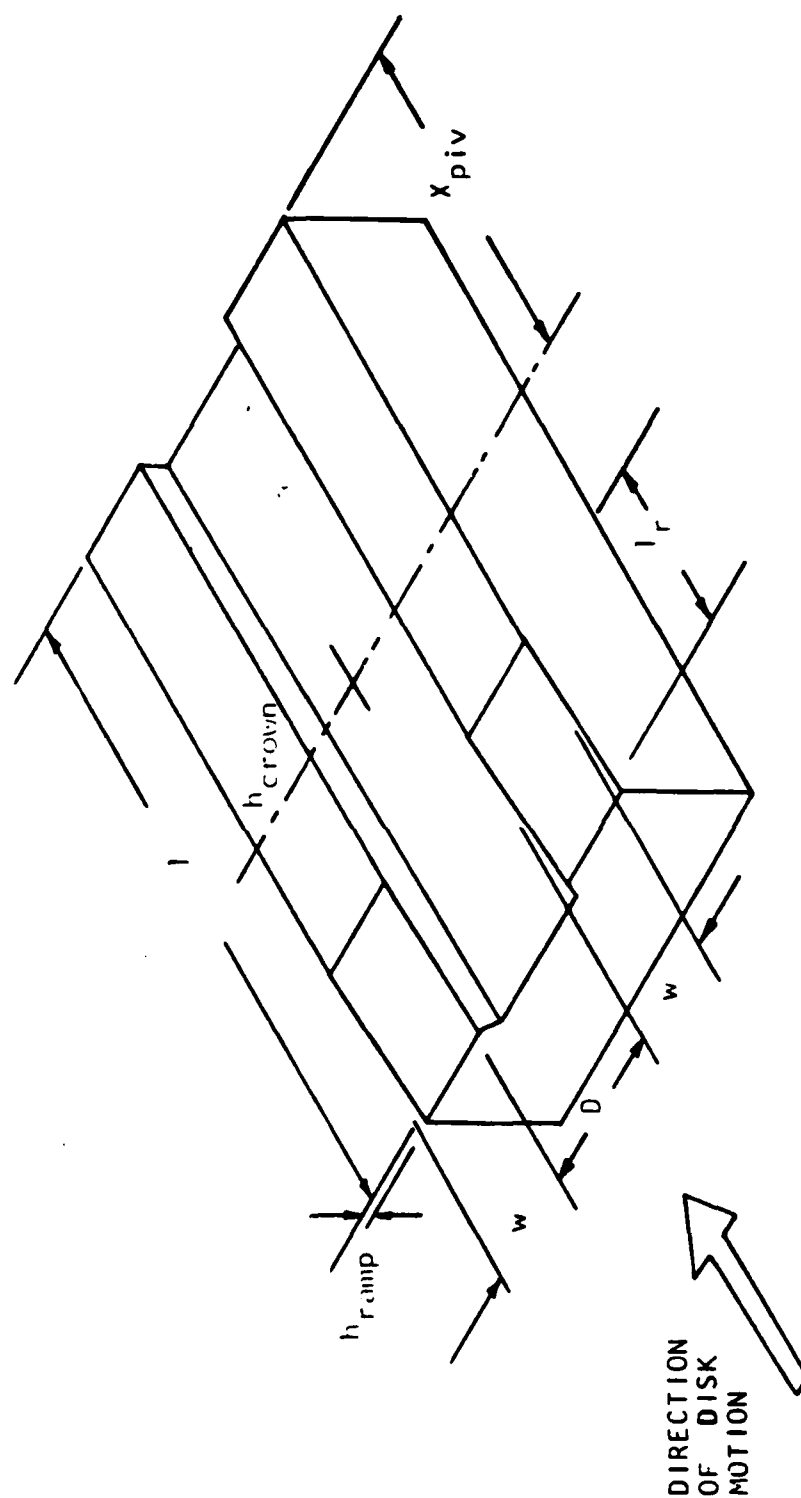
FIGURE 11-3: SCHEMATIC DIAGRAM OF THE WINCHESTER TYPE HEAD
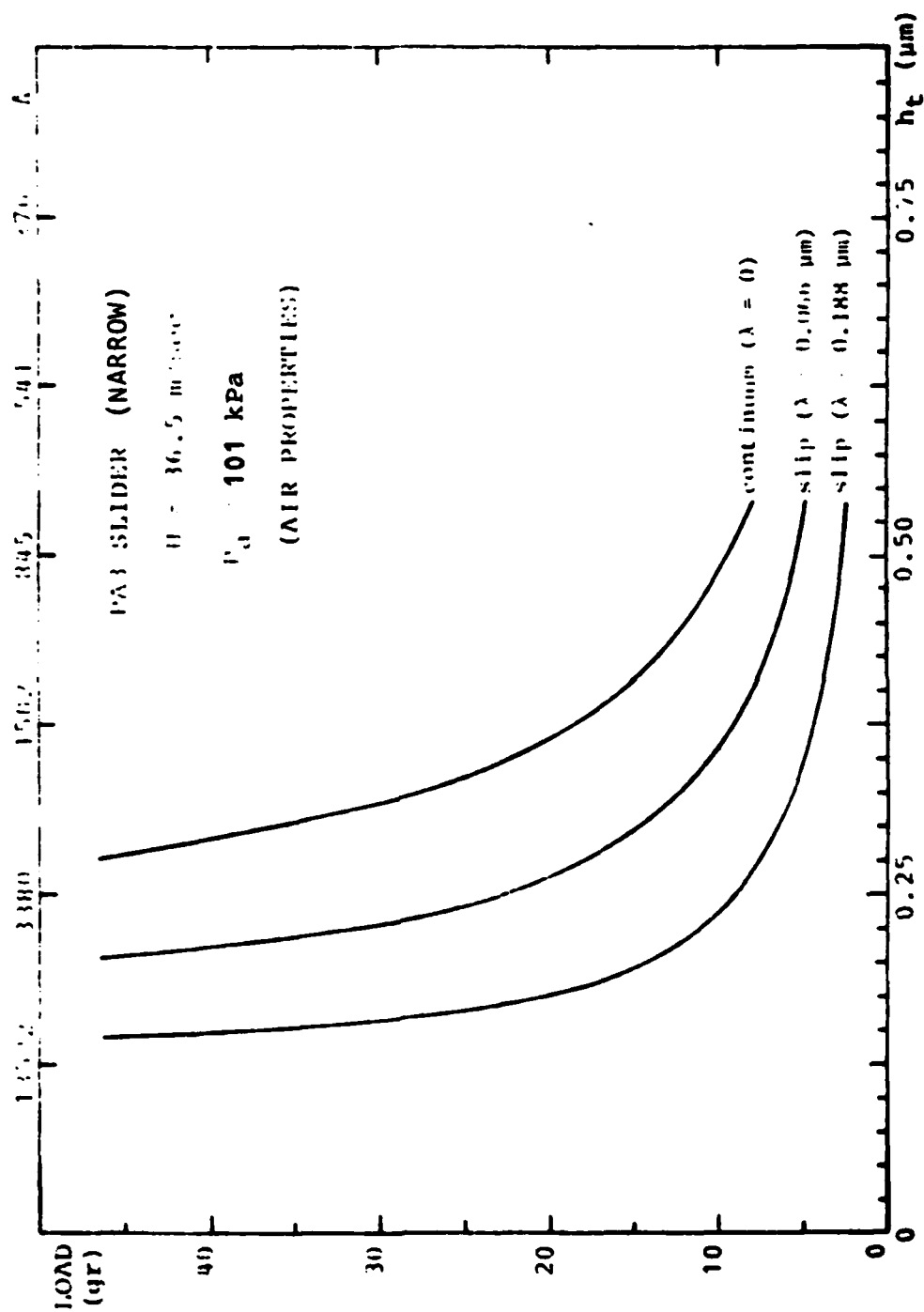
FIGURE 11-4:   EFFECT OF MEAN FREE PATH ON LOAD CAPACITY
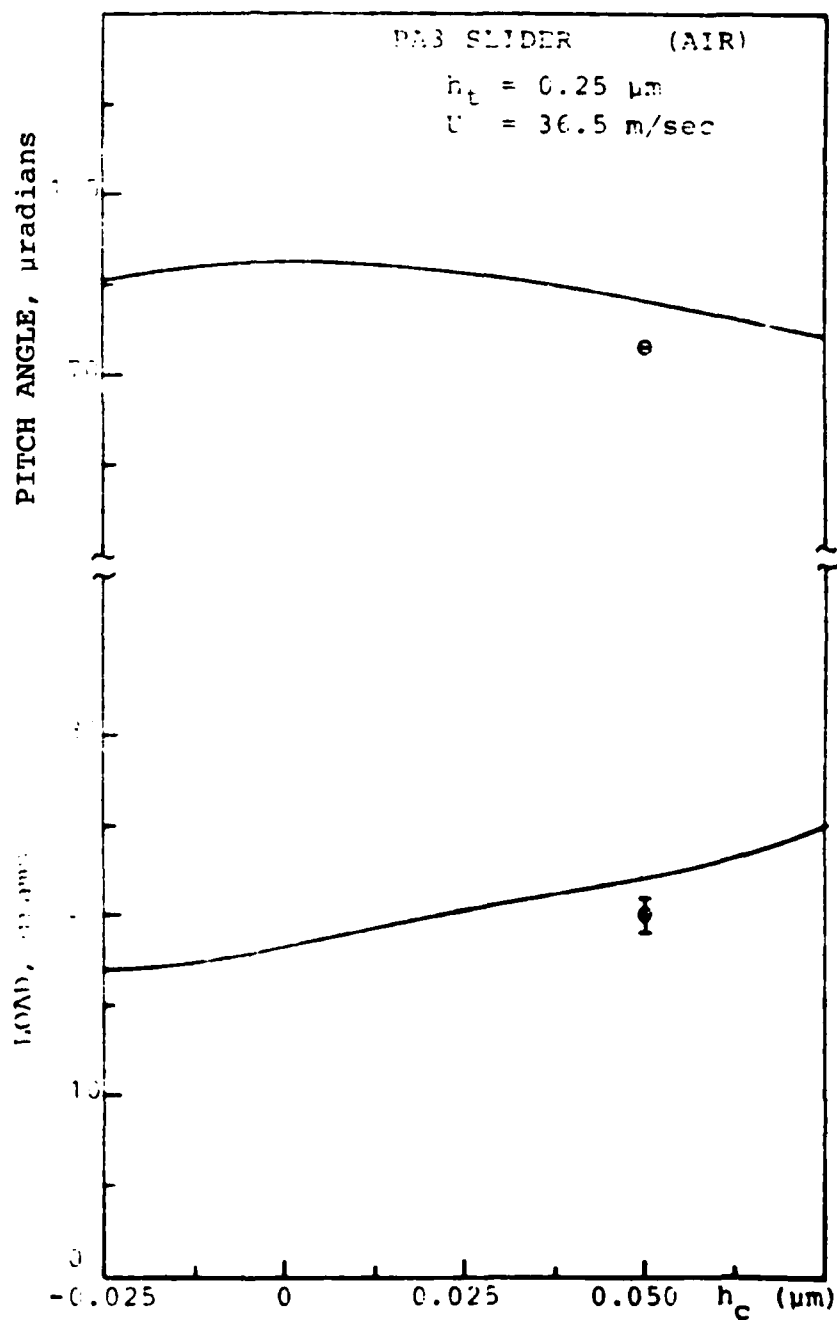
FIGURE 11-5: EFFECT OF SURFACE CROWNING ON LOAD CAPACITY
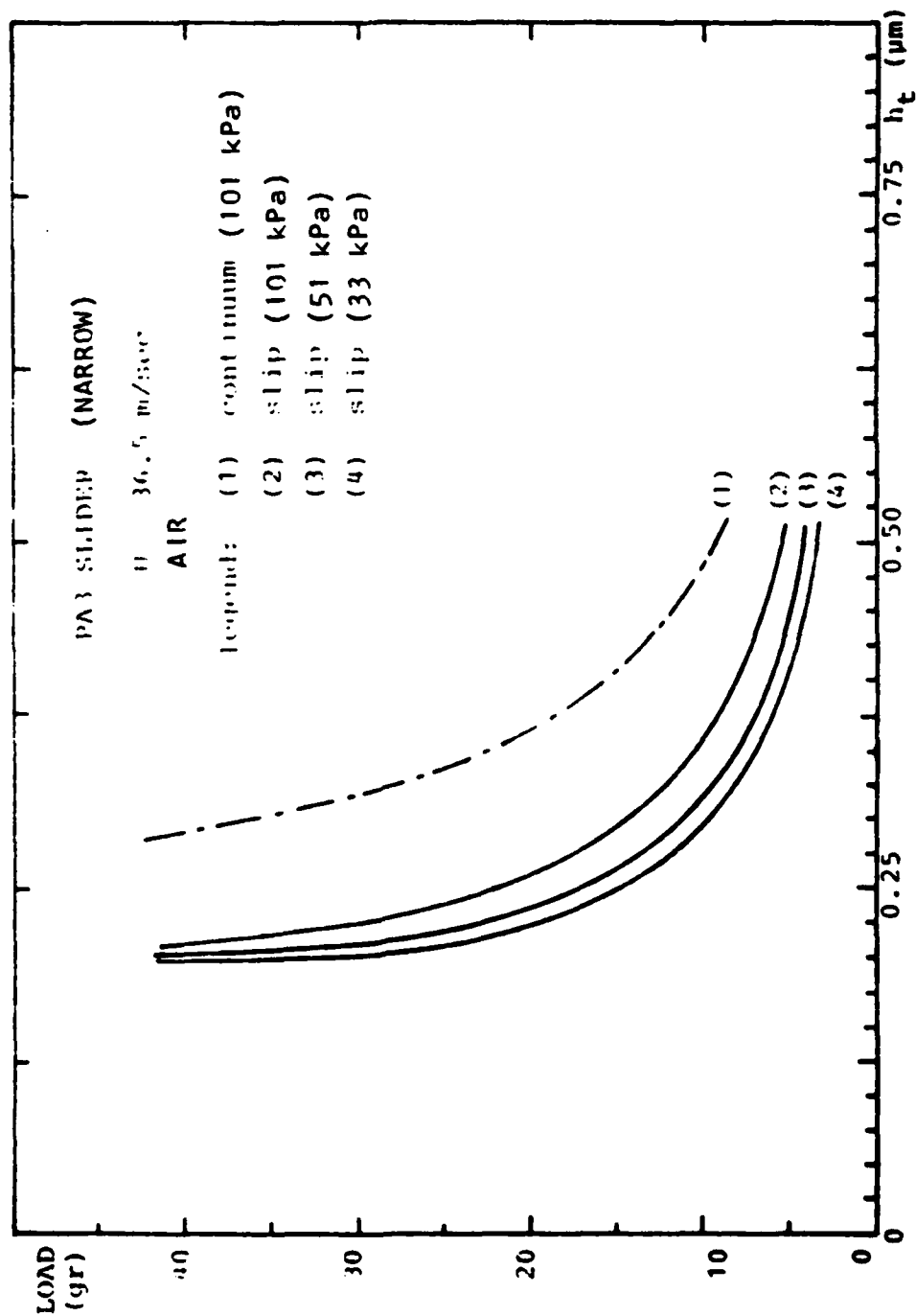
FIGURE 11-6: EFFECT OF OPERATING PRESSURE ON LOAD CAPACITY
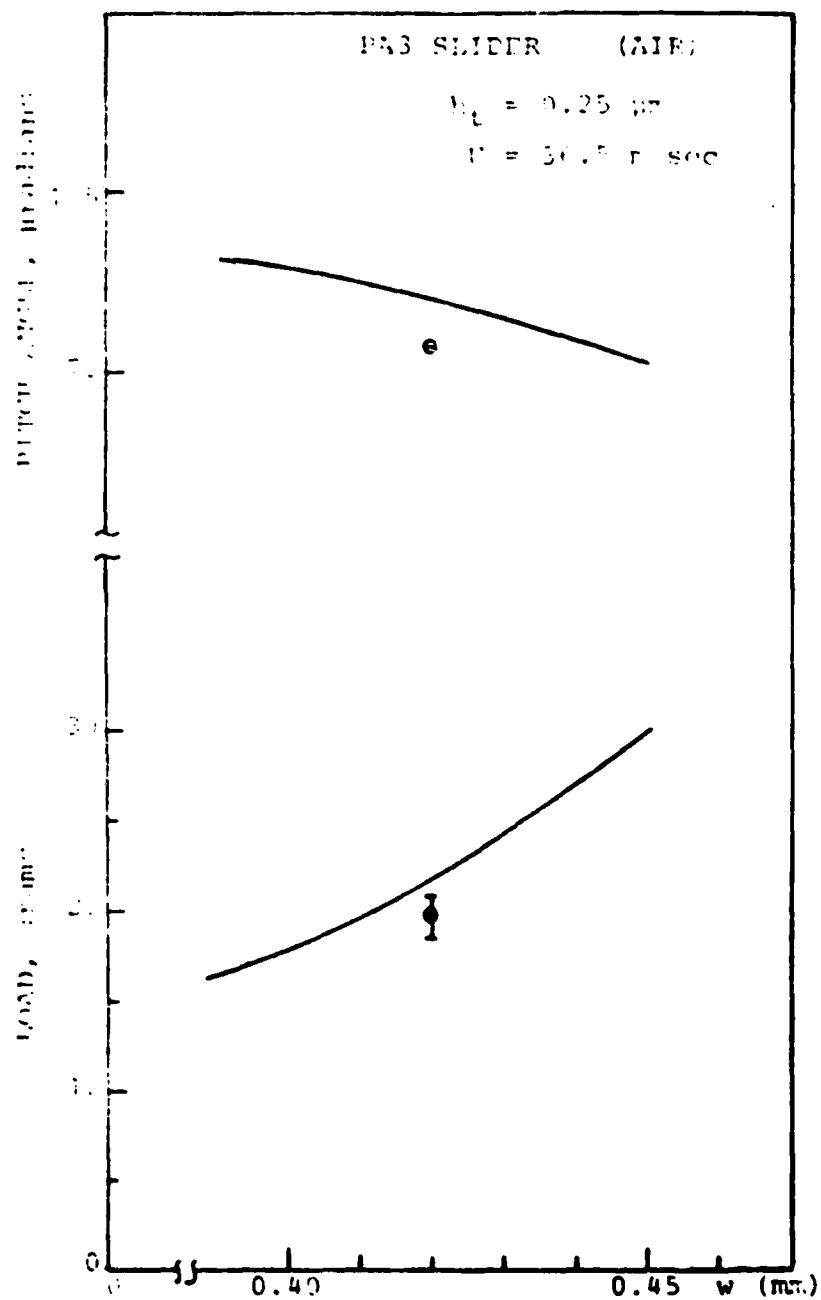
FIGURE 11-7: EFFECT OF SLIDER WIDTH ON LOAD CAPACITY
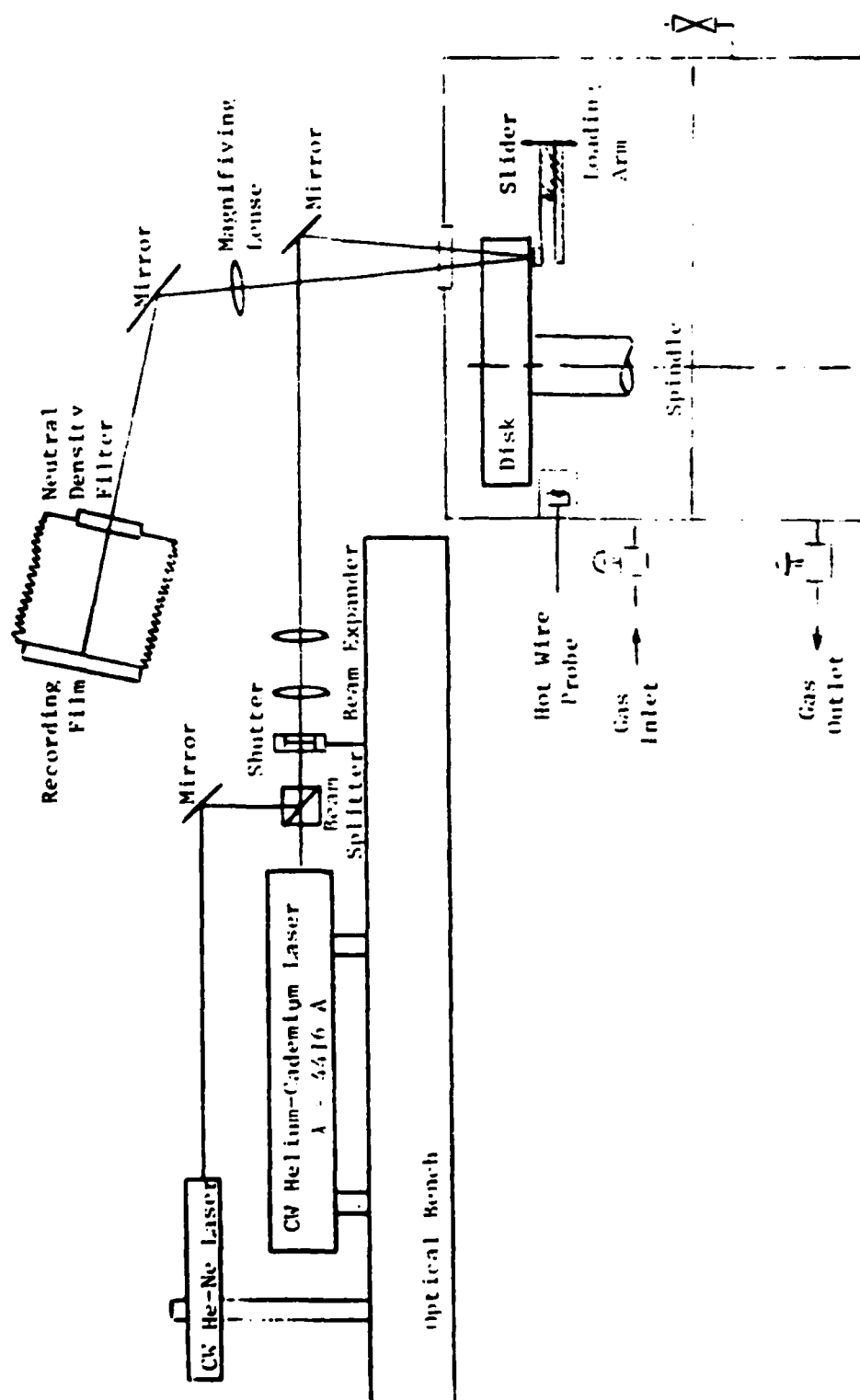
FIGURE 11-8: SCHEMATIC DIAGRAM OF INTERFEROMETRIC SETUP
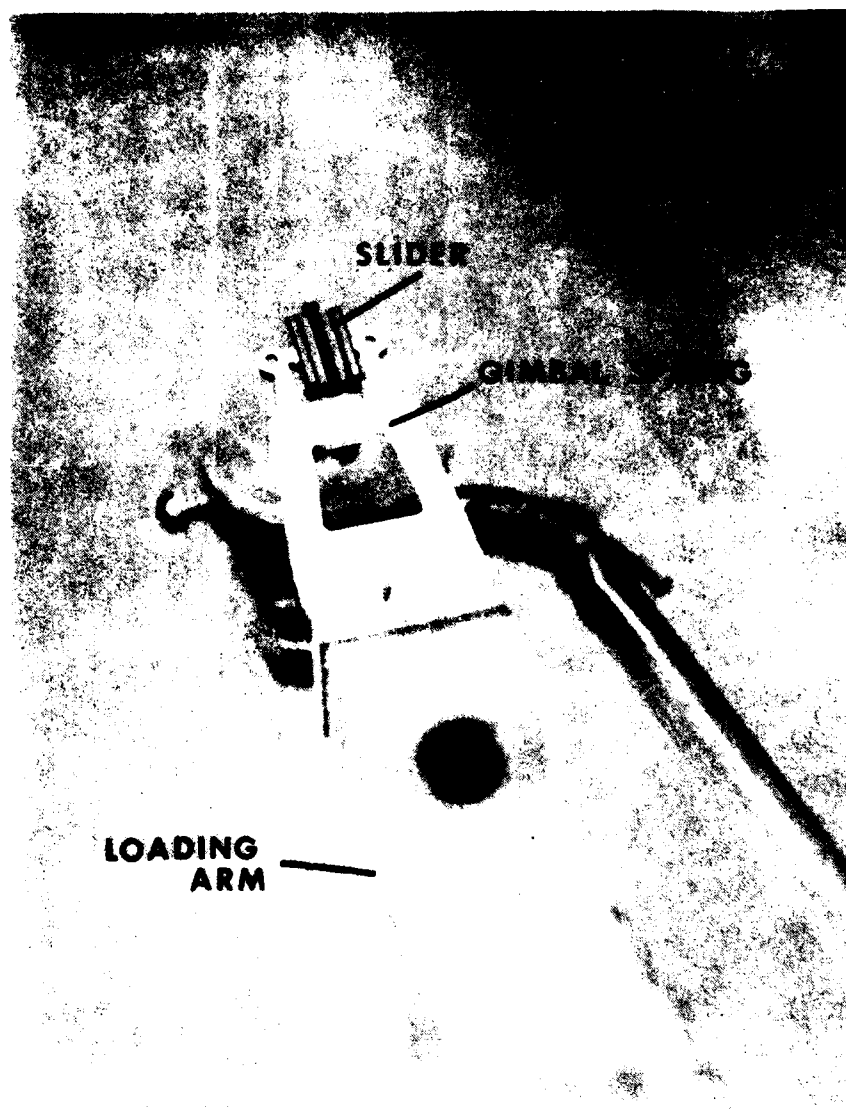
FIGURE 11-9: CLOSE-UP VIEW OF THE SLIDER ASSEMBLY

FIGURE 11-10: VIEW OF THE LOADING ARM ASSEMBLY
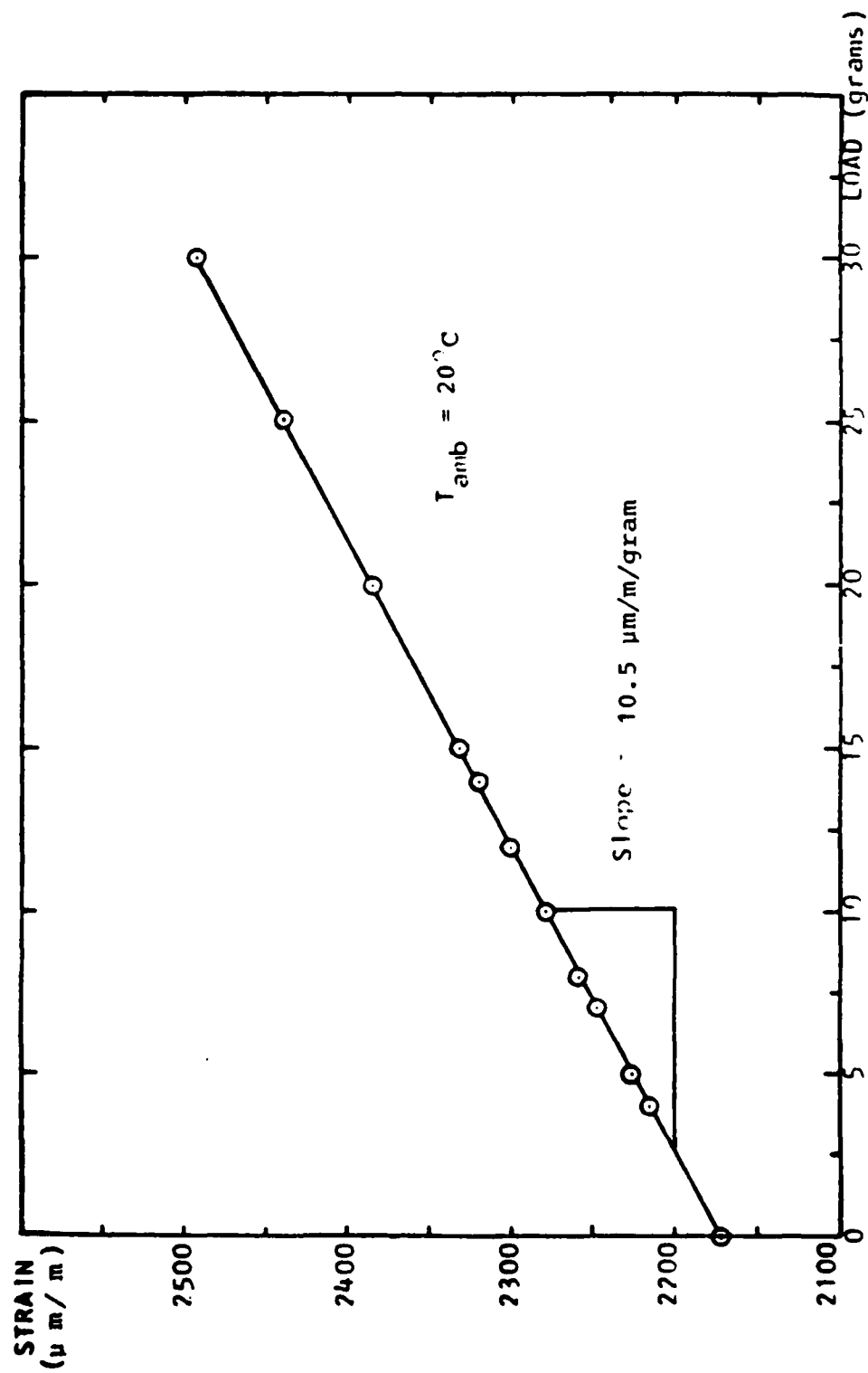
FIGURE 11-11: STRAIN RESPONSE CURVE FOR THE DELRIN LOADING ARM

61
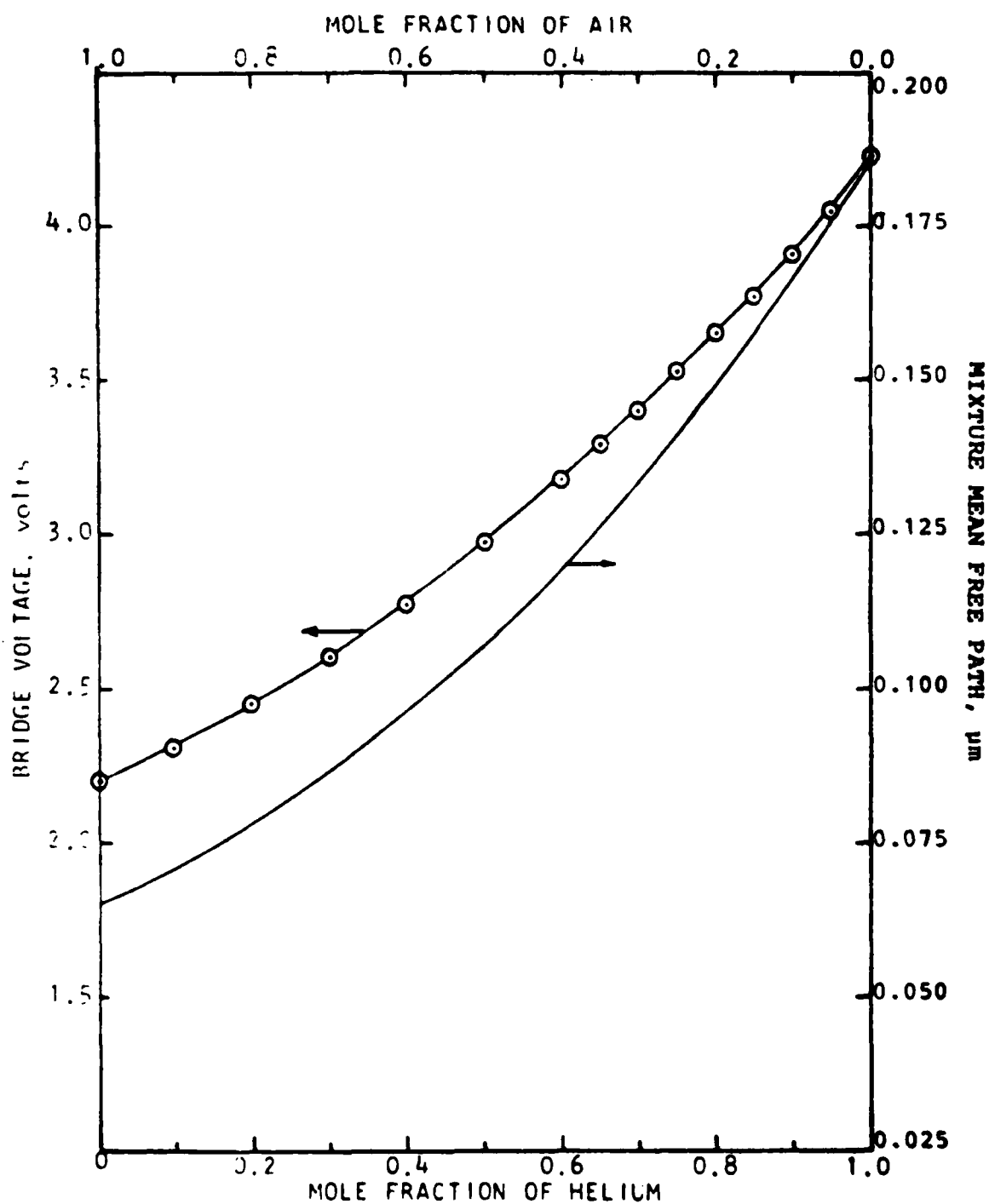
FIGURE 11-12: HOT WIRE PROBE RESPONSE CURVE FOR
HELIUM/AIR MIXTRUE

HELIUM-NEON LASER
(λ = 632.8 nm)

HELIUM-CADMIUM LASER
(λ = 441.6 nm)

FIGURE 11-13: TYPICAL INTERFERENCE FRINGE PATTERN – PA3 SLIDER IN HELIUM
U = 36.07 m/sec, W = 10.5 grams.
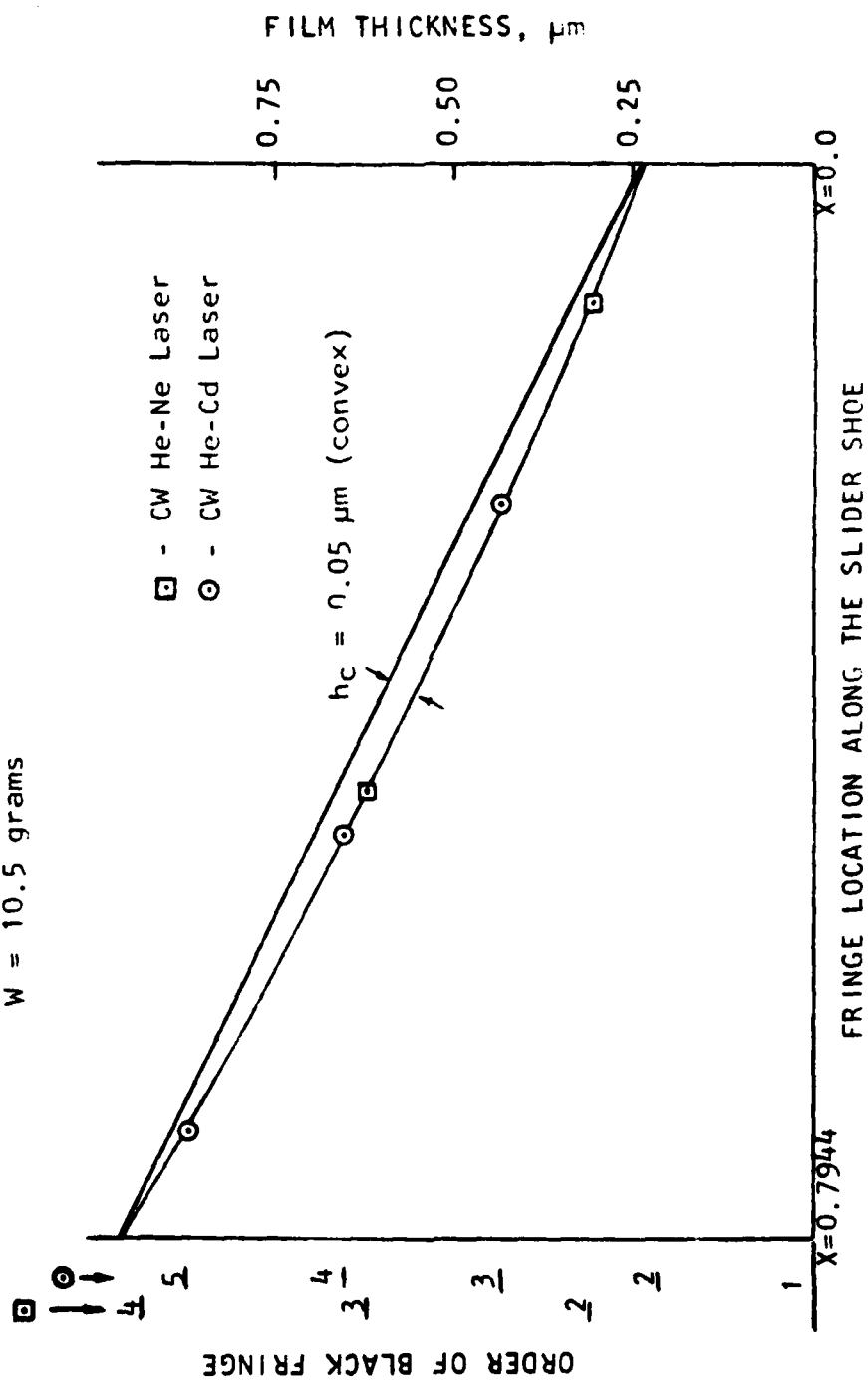
FIGURE 11-14: DATA PROCESSING AND CROWN DETERMINATION
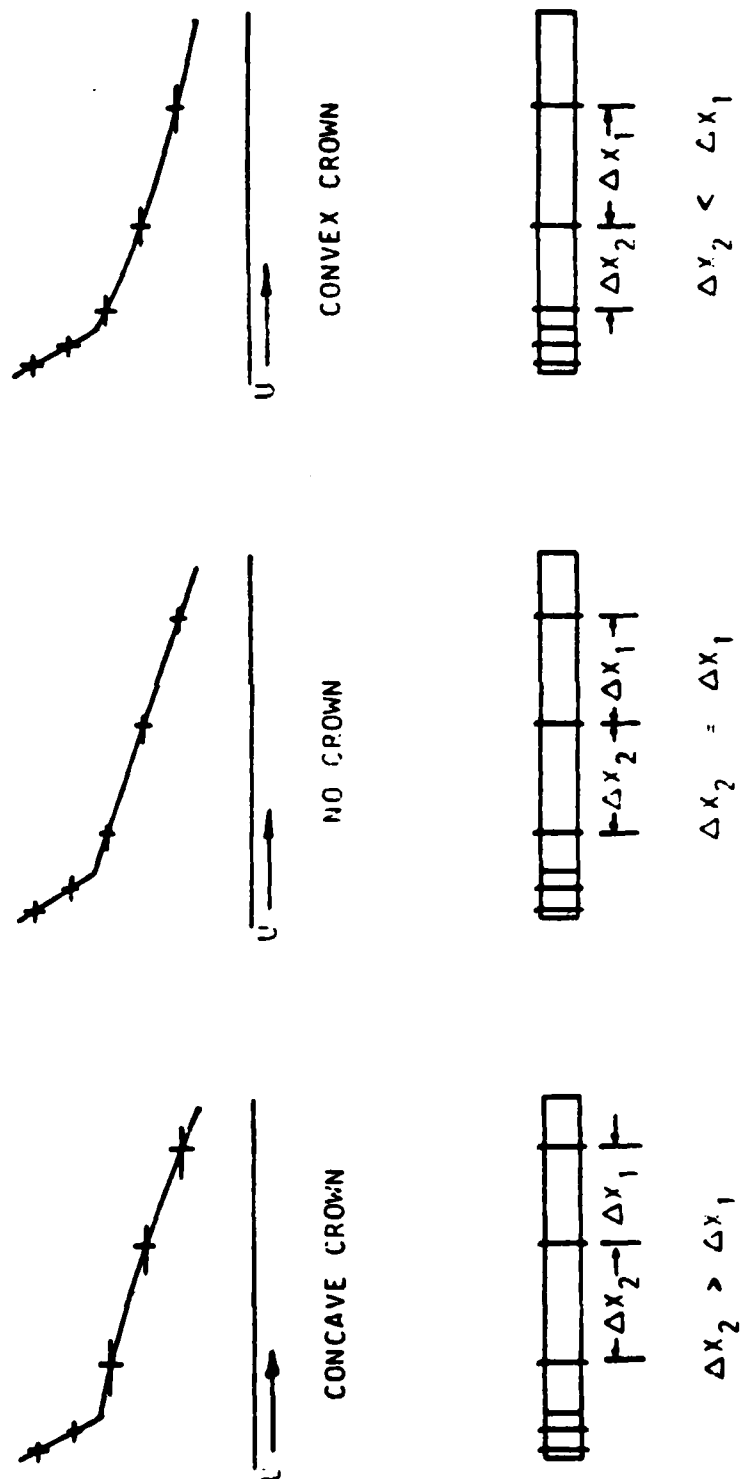
FIGURE 11-15 : TYPICAL FRINGE PATTERN APPEARING ON TAPER-LAND BEARING WITH OR WITHOUT CROWN

HELIUM-NEON LASER
($\lambda = 632.8$ nm)

HELIUM-CADMIUM LASER
($\lambda = 441.6$ nm)

FIGURE 11-16: TYPICAL INTERFERENCE FRINGE PATTERNS SHOWING THE "CRASH" PHENOMENON - PA3 SLIDER IN AIR - U = 36.07 m/sec, W = 25.0 grams.
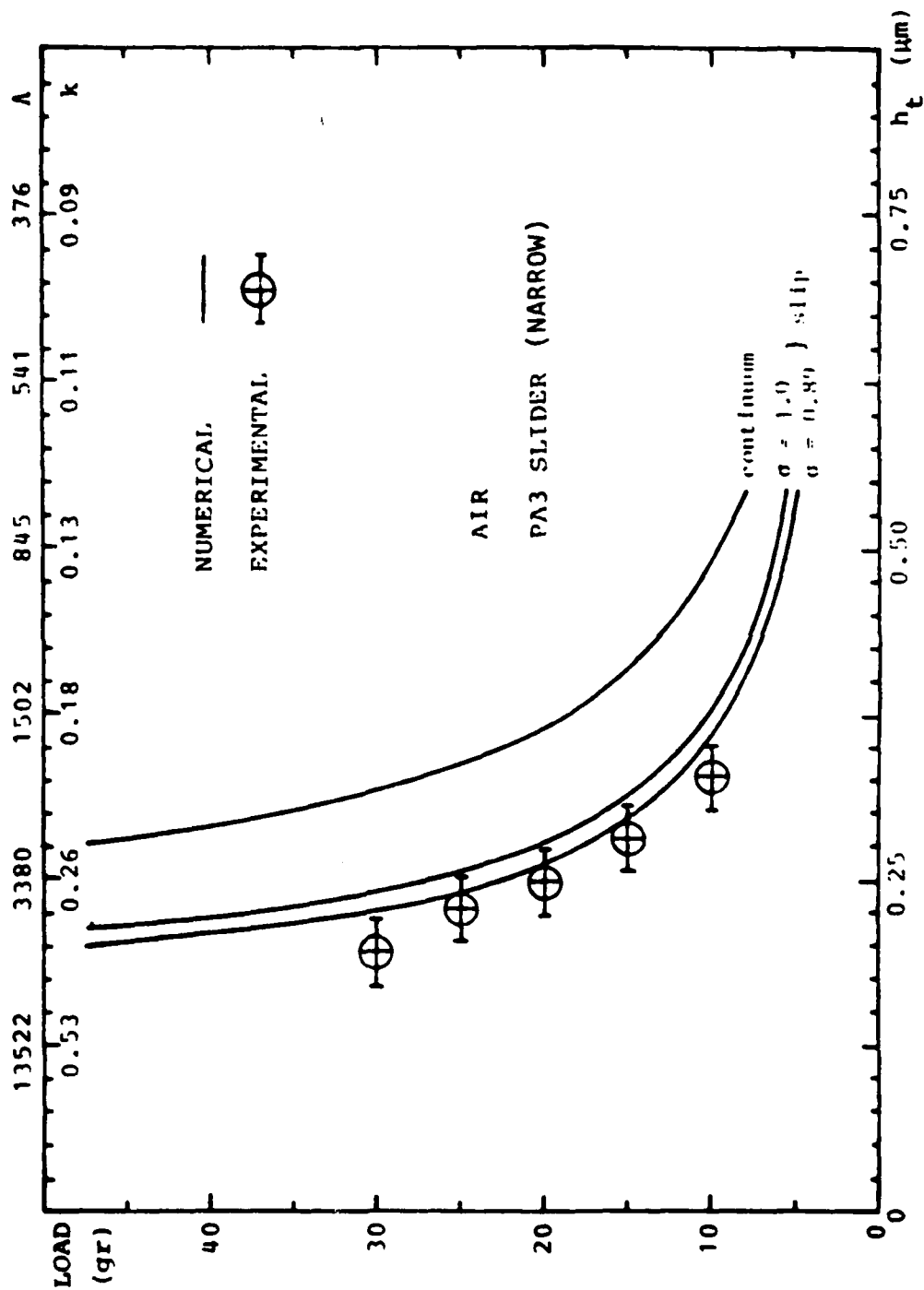
FIGURE 11-17: LOAD VS TRAILING EDGE CLEARANCE, U = 36.52 m/sec
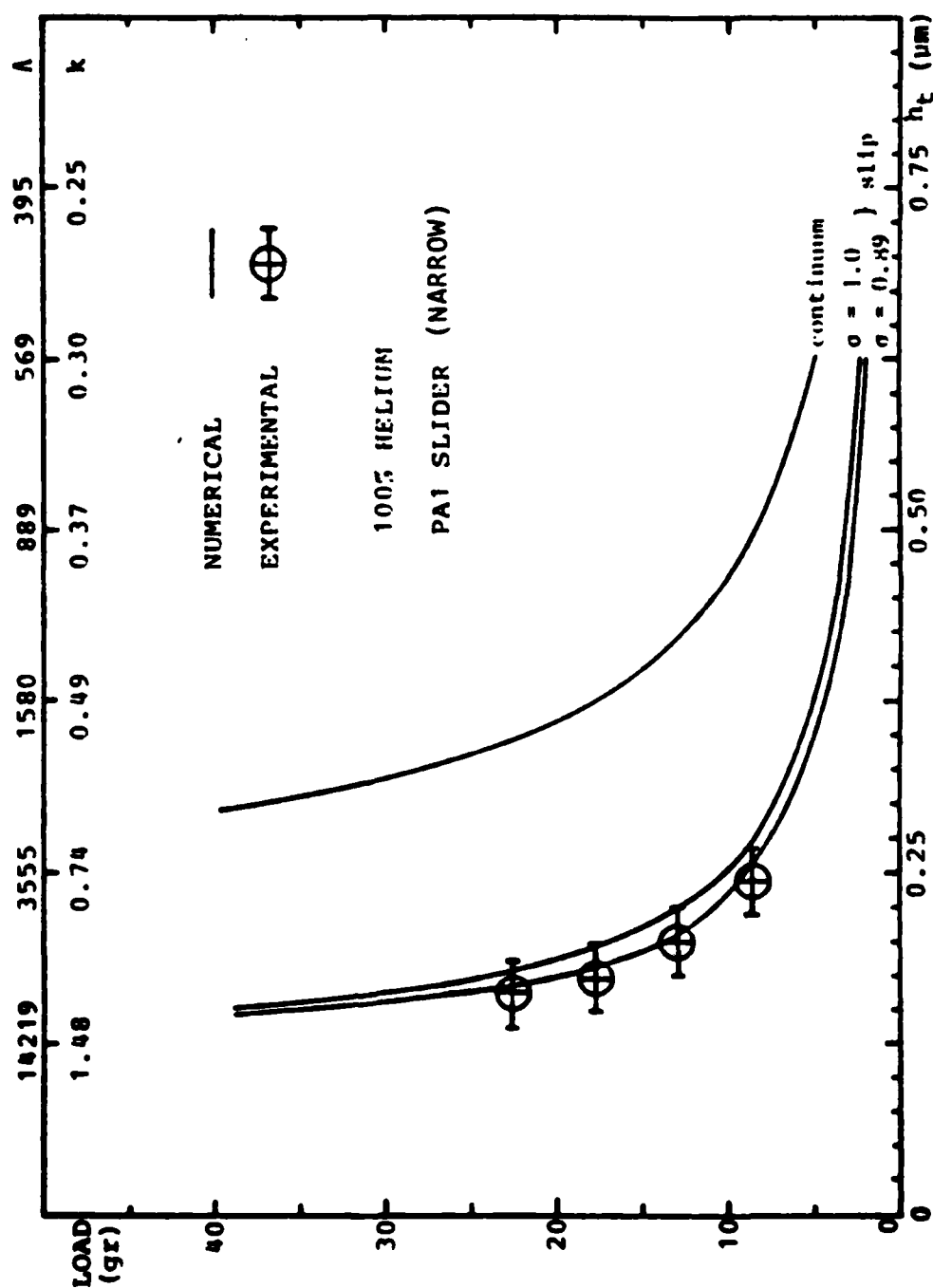
FIGURE 11-18 : LOAD VS TRAILING EDGE CLEARANCE, U = 36.13 m/sec
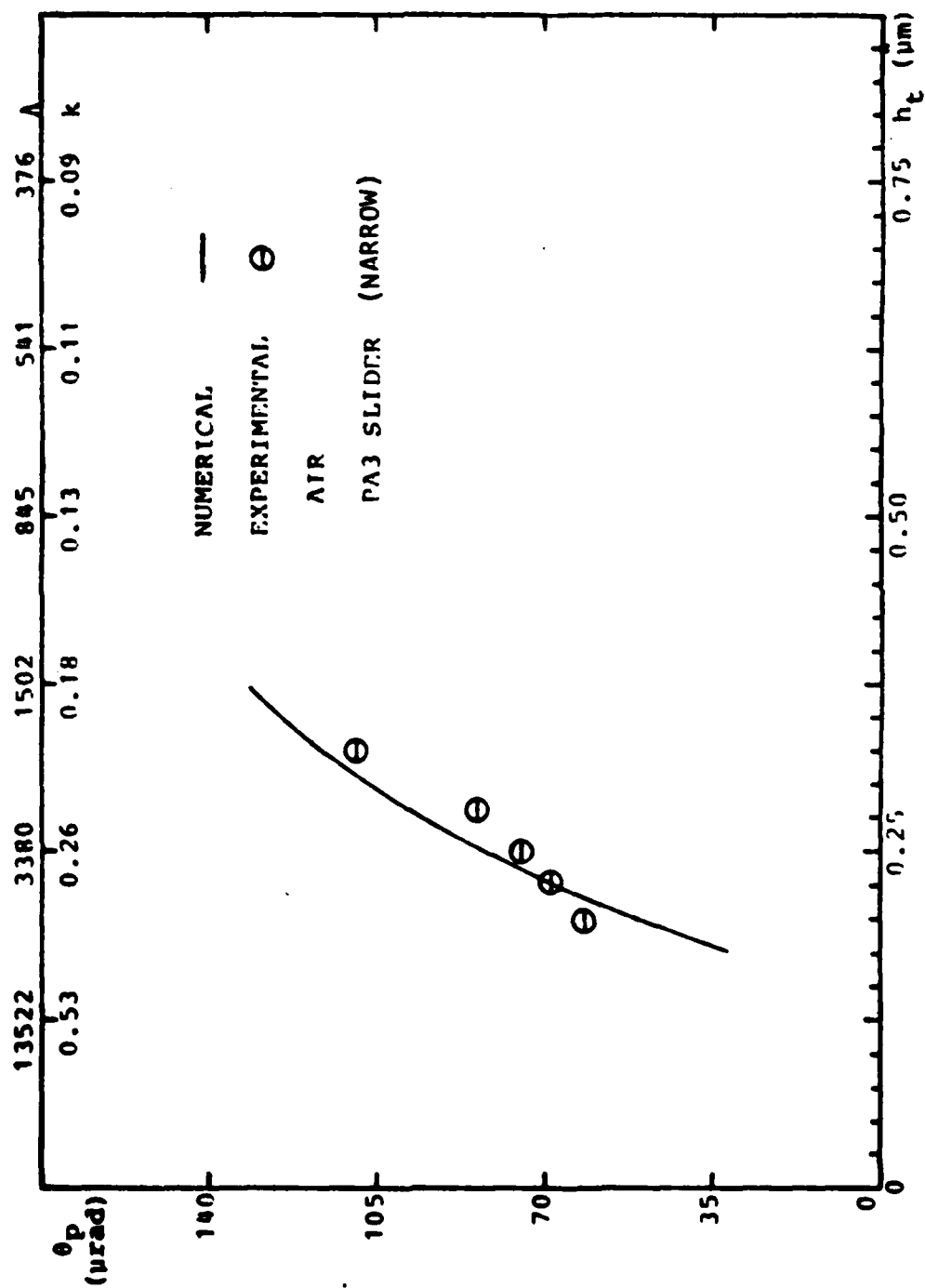
FIGURE 11-19: PITCH ANGLE VS TRAILING EDGE CLEARANCE, U = 36.52 m/sec

69
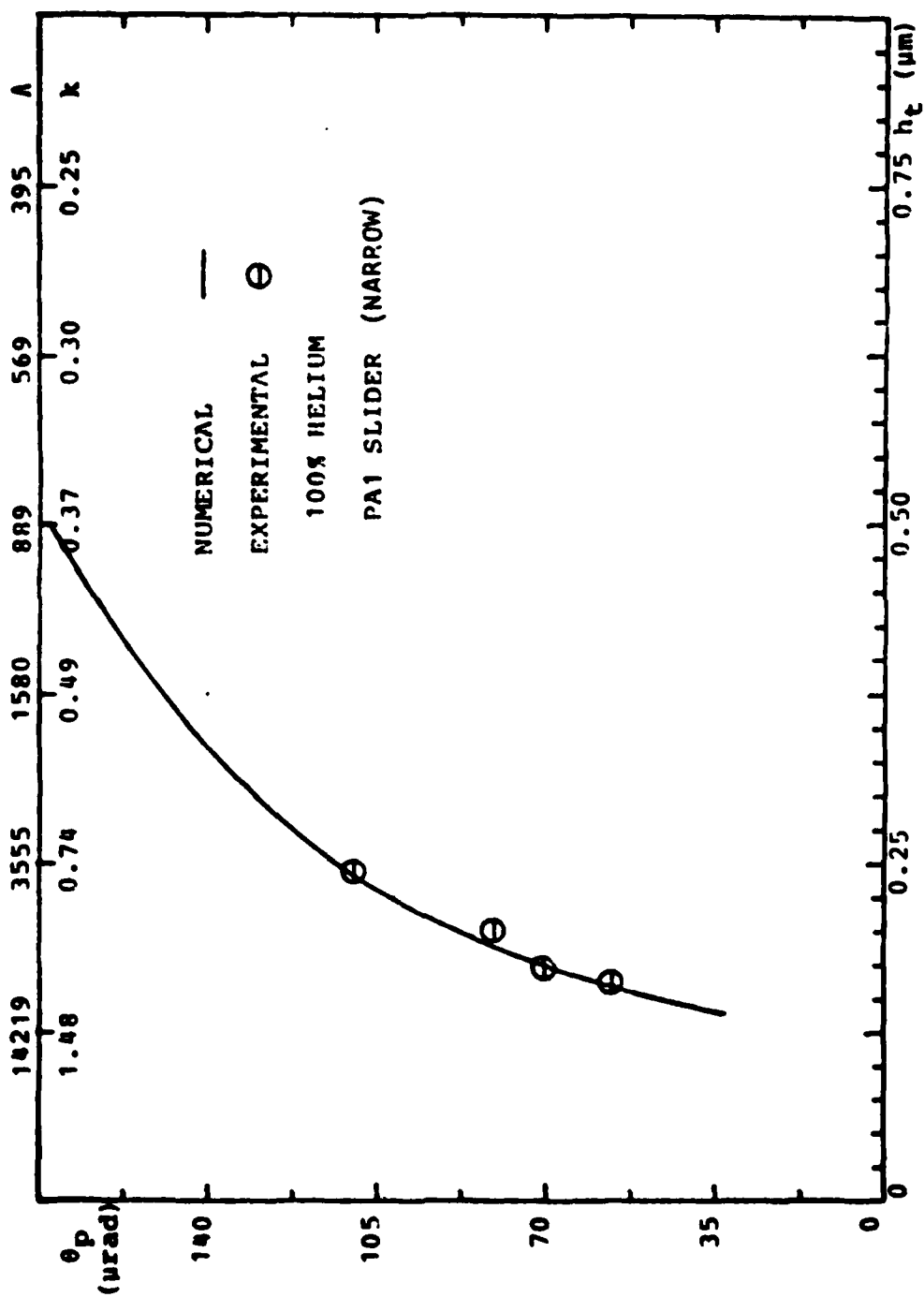
FIGURE 11-20: PITCH ANGLE VS TRAILING EDGE CLEARANCE, U = 36.13 m/sec
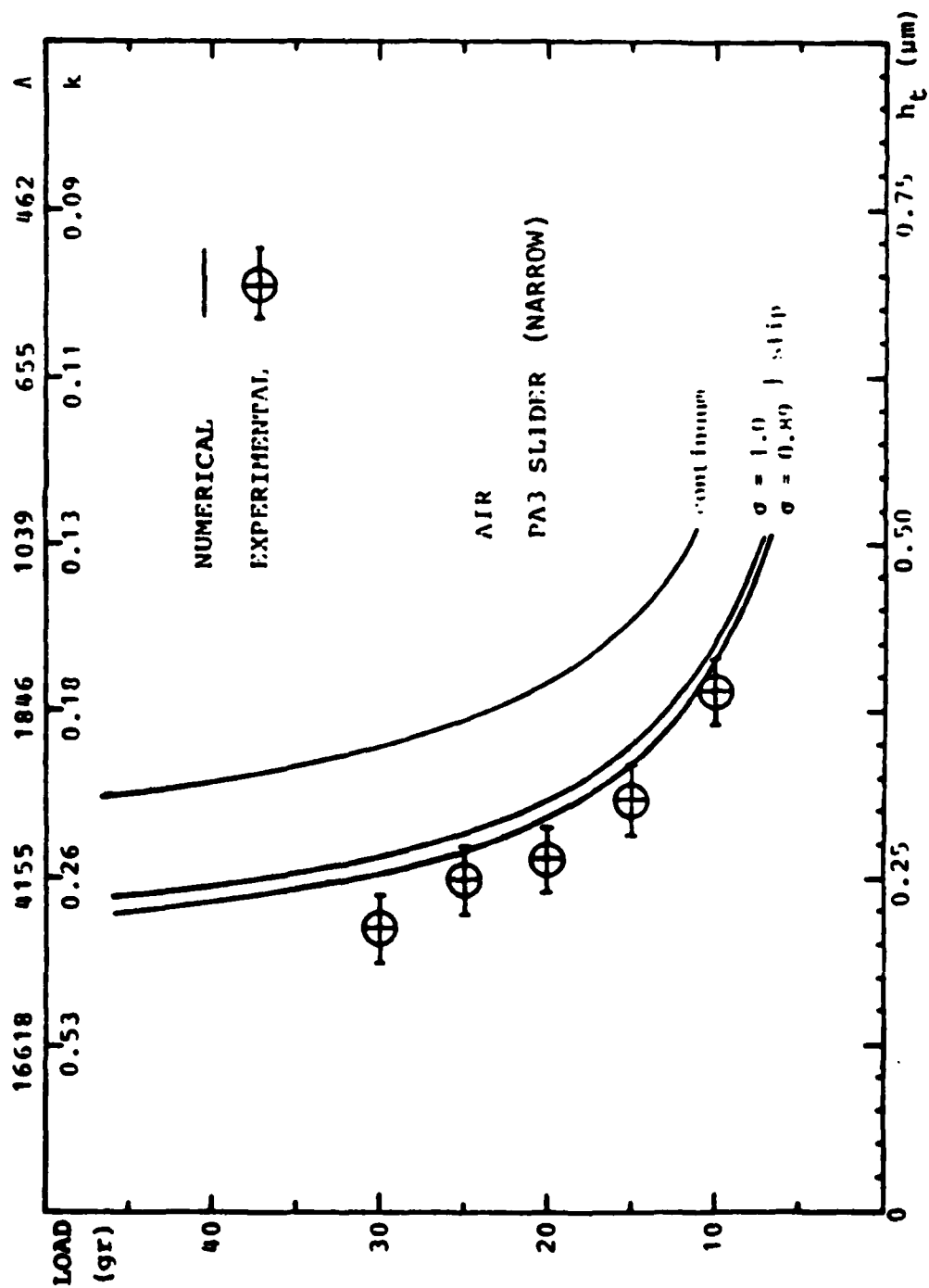
FIGURE 11-21:   LOAD VS TRAILING EDGE CLEARANCE, V = 44.88 m/sec
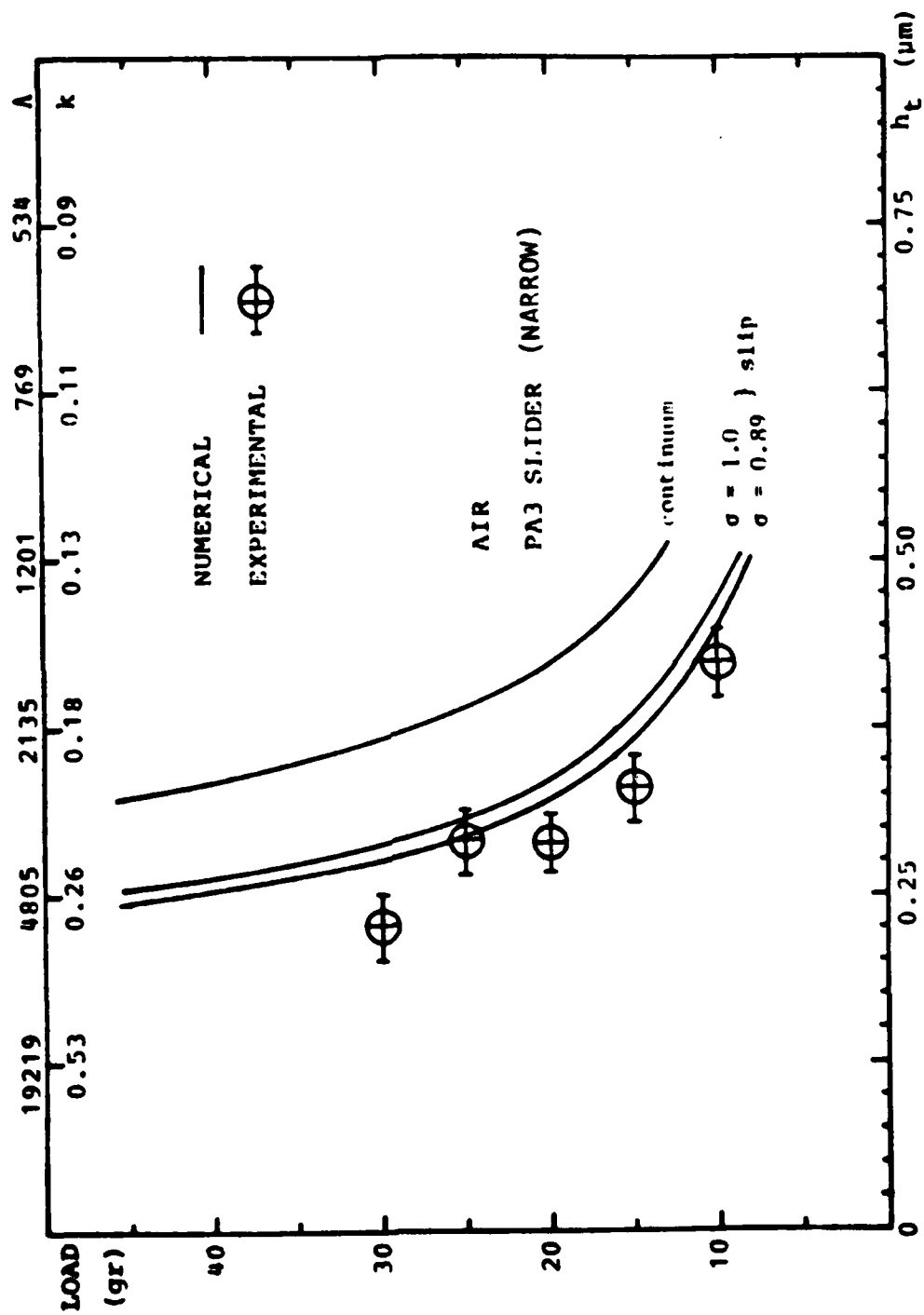
FIGURE 11-22: LOAD VS TRAILING EDGE CLEARANCE, U = 51.90 m/sec

72
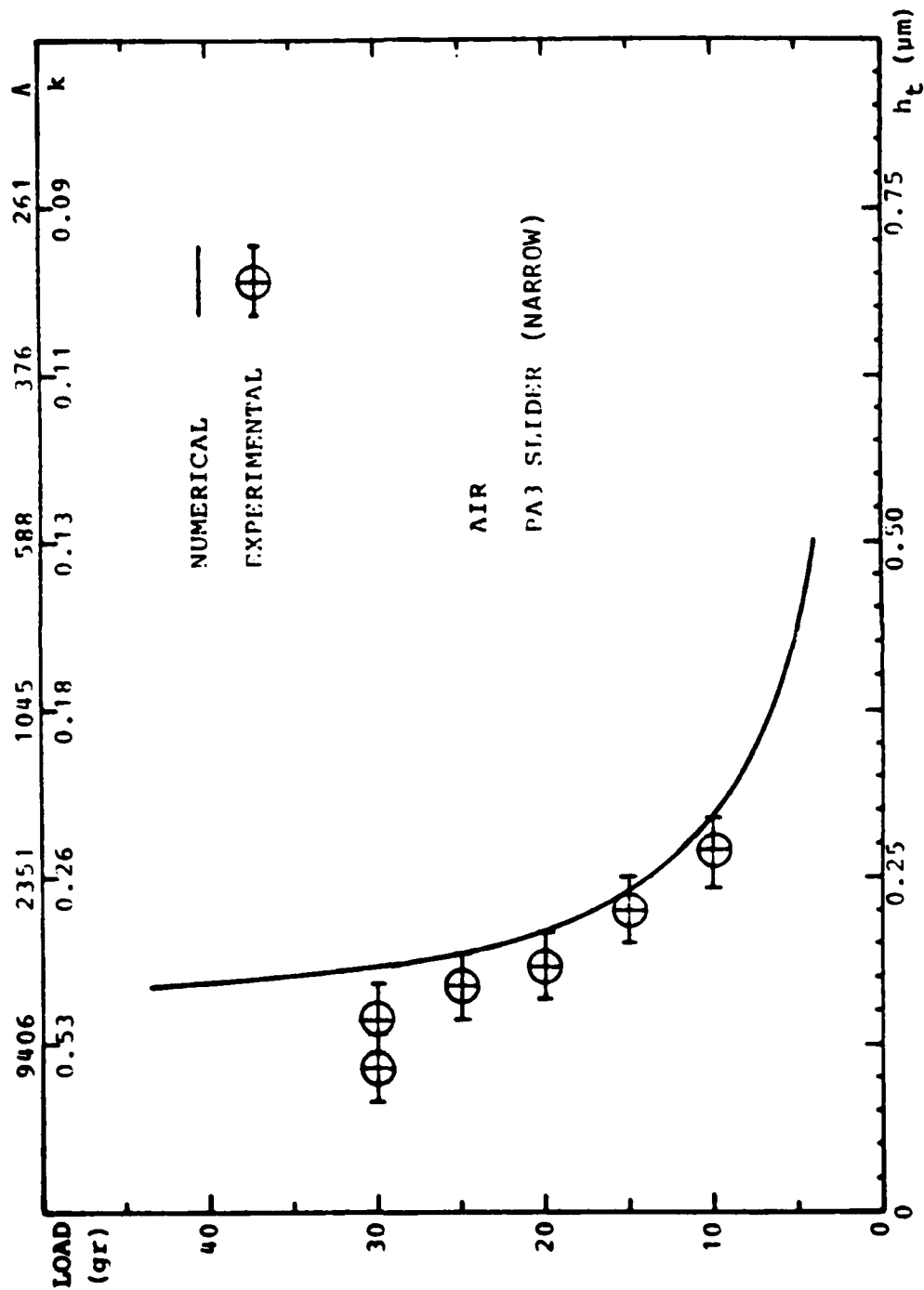
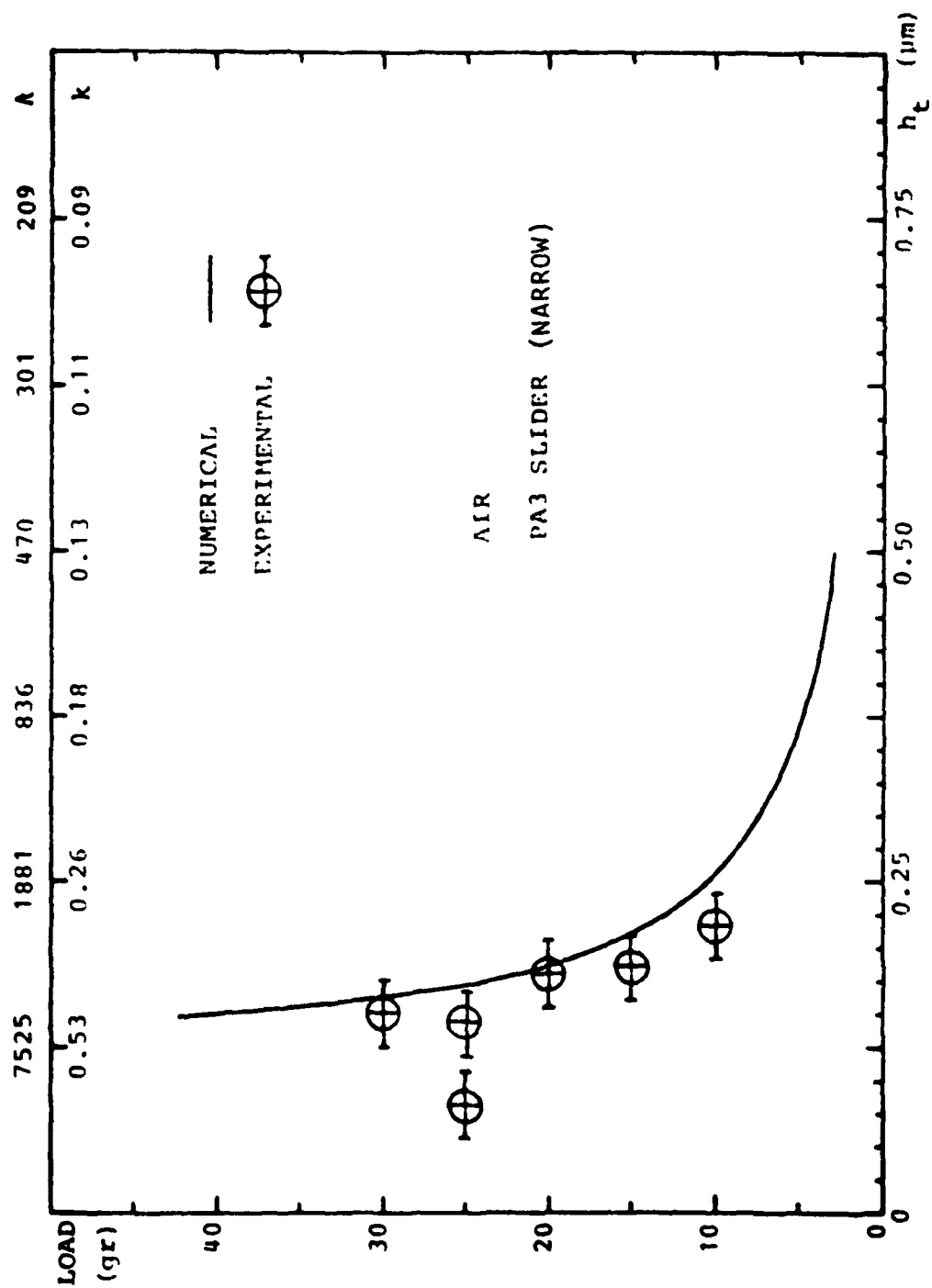FIGURE 11-23: LOAD VS TRAILING EDGE CLEARANCE, U = 25.40 m/sec

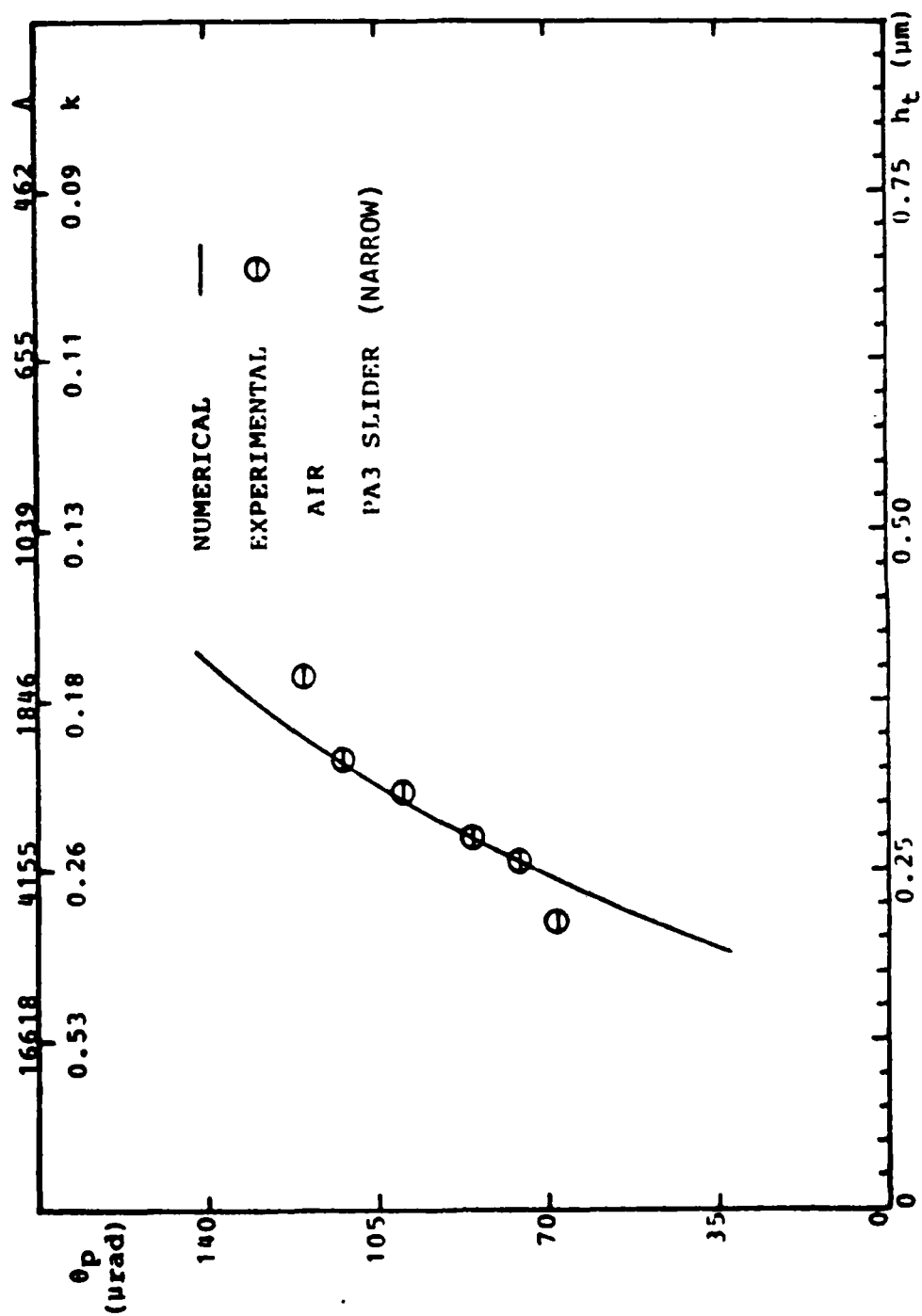Figure 11-24: LOAD VS TRAILING EDGE CLEARANCE, U = 20.32 m/sec

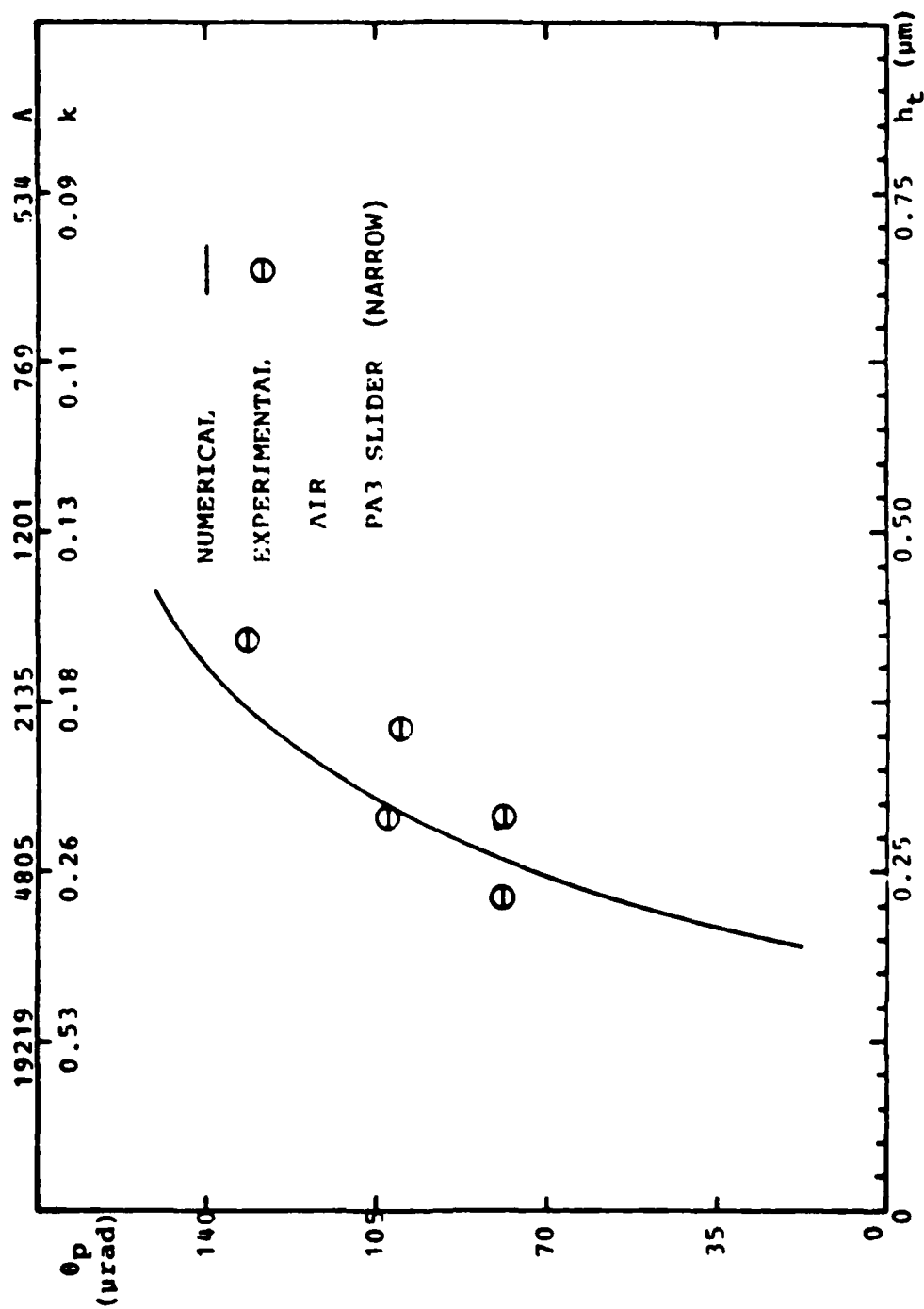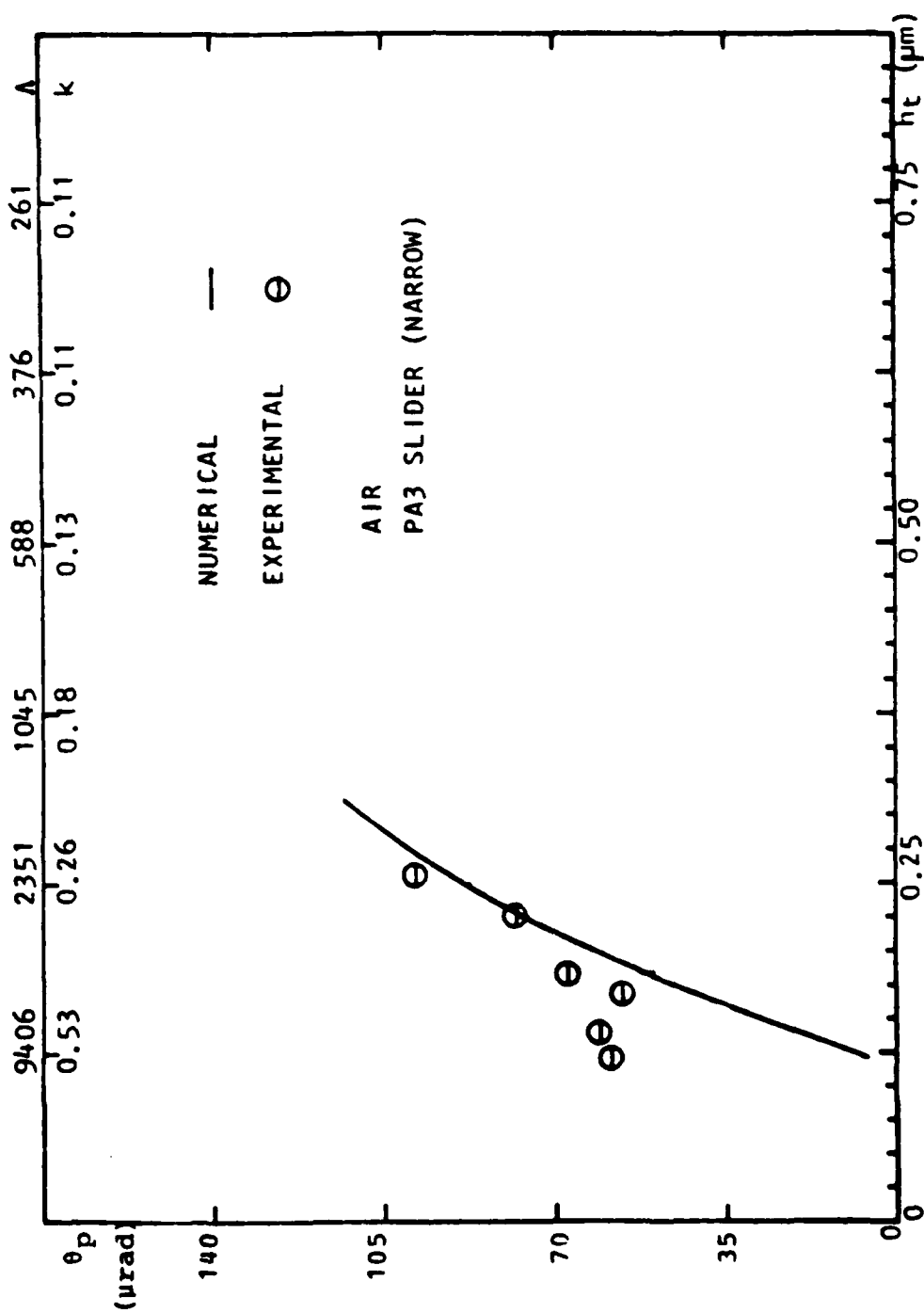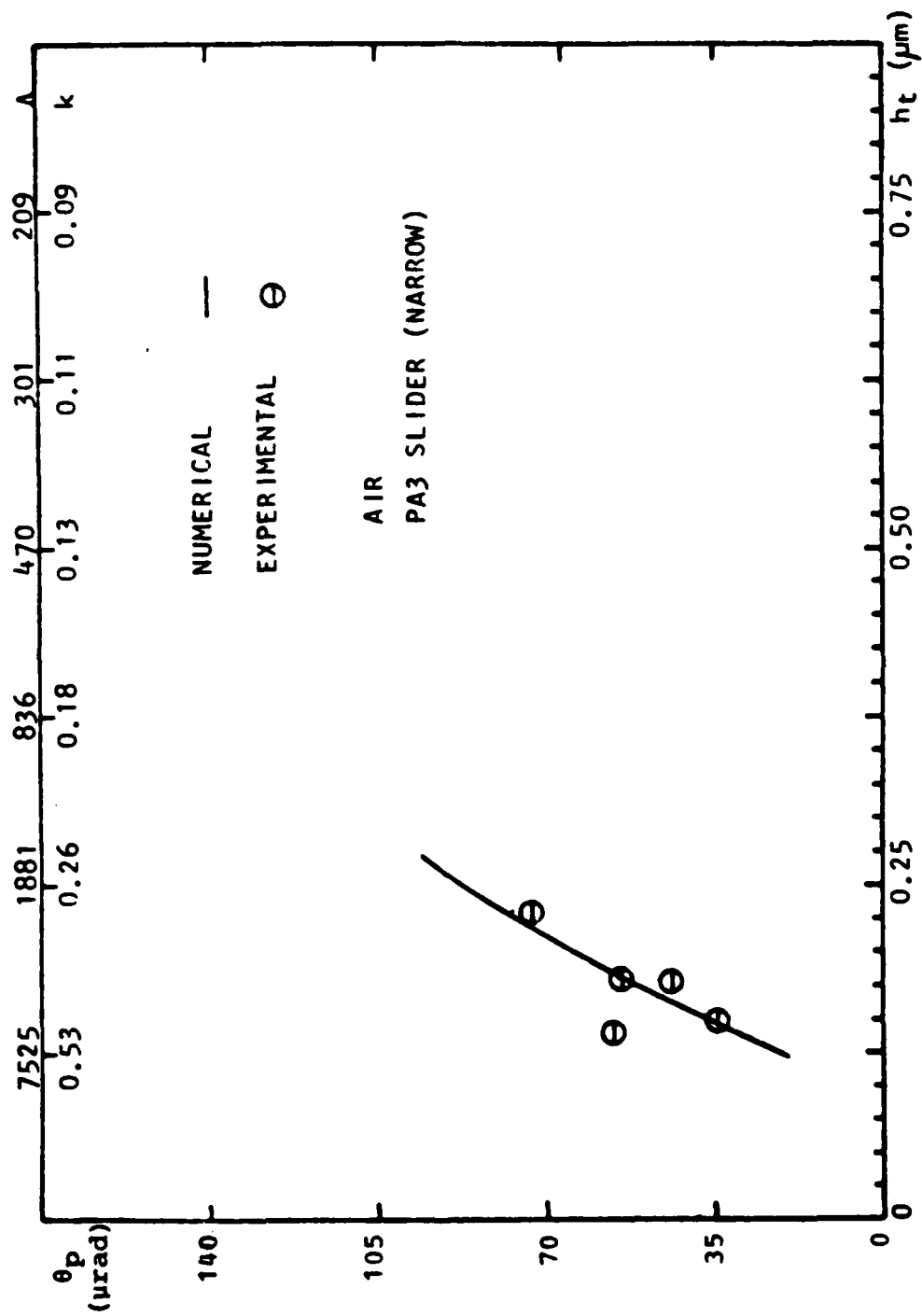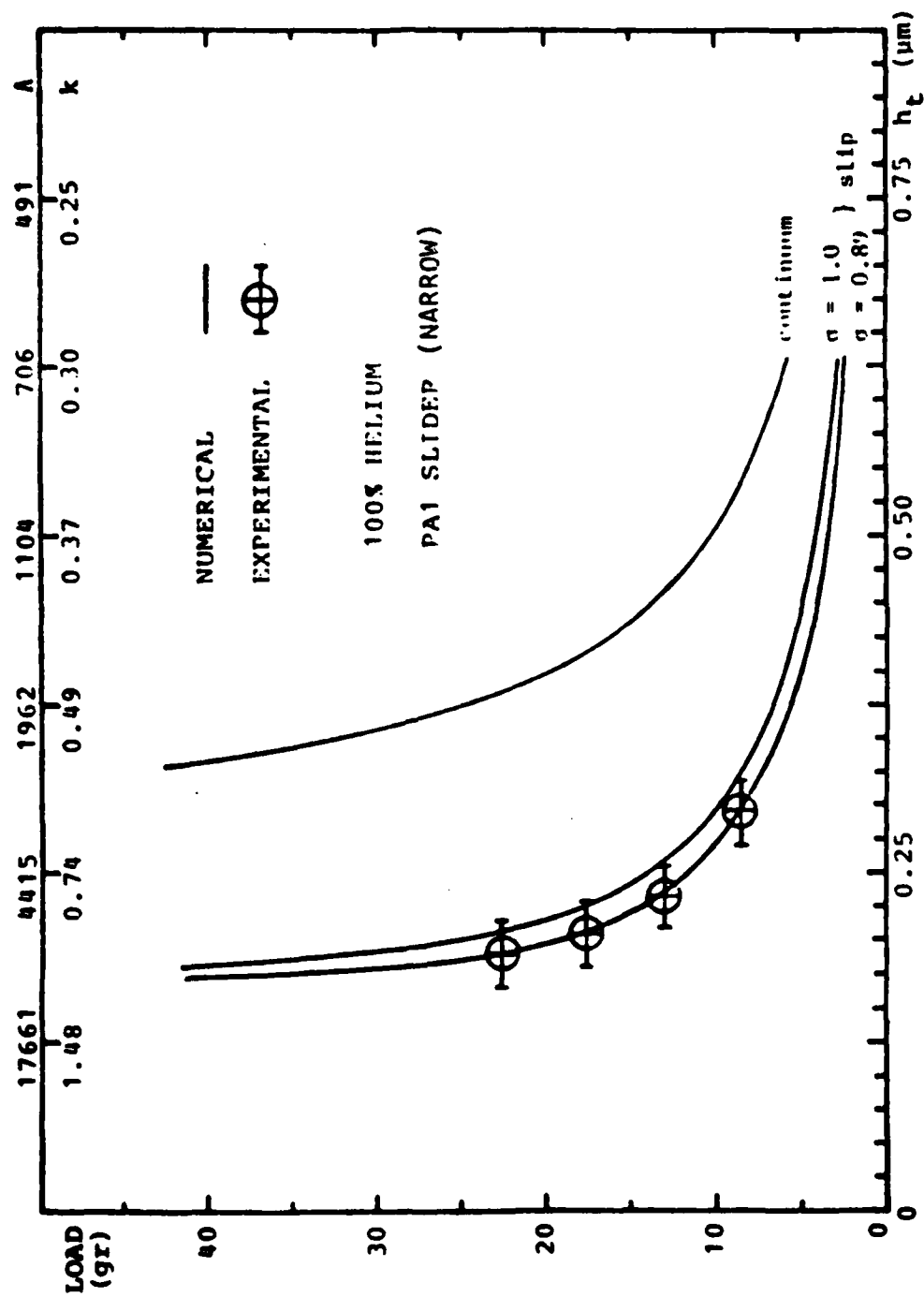FIGURE 11-25: PITCH ANGLE VS TRAILING EDGE CLEARANCE, U = 44.88 m/sec

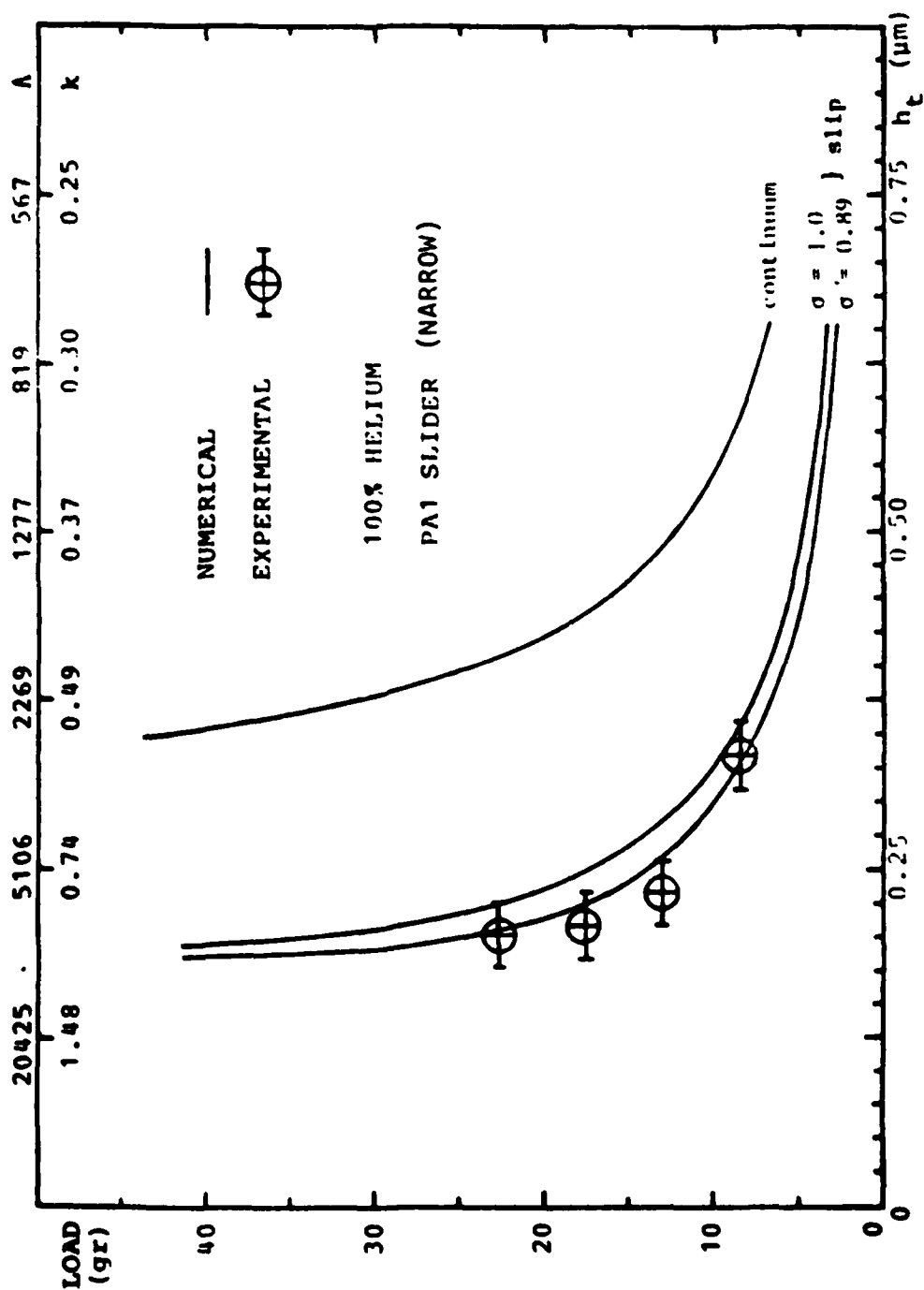FIGURE 11-26:   PITCH ANGLE VS TRAILING EDGE CLEARANCE, U = 51.90 m/sec

FIGURE 11-27: PITCH ANGLE VS TRAILING EDGE CLEARANCE, U = 25.40 m/sec

FIGURE 11-28: PITCH ANGLE VS TRAILING EDGE CLEARANCE, U = 20.32 m/sec

FIGURE 11-29: LOAD VS TRAILING EDGE CLEARANCE, U = 44.88 m/sec

FIGURE 11-30: LOAD VS TRAILING EDGE CLEARANCE, U = 51.90 m/sec

FIGURE 11-31: PITCH ANGLE VS TRAILING EDGE CLEARANCE, U = 44.88 m/sec

FIGURE 11-32: PITCH ANGLE VS TRAILING EDGE CLEARANCE, U = 51.90 m/sec

FIGURE 11-33: LOAD VS TRAILING EDGE CLEARANCE, U = 36.13 m/sec

FIGURE 11-34: LOAD VS TRAILING EDGE CLEARANCE, U = 44.88 m/sec

FIGURE 11-35: LOAD VS TRAILING EDGE CLEARANCE, U = 51.90 m/sec

A

k

373   0.09

537   0.11

NUMERICAL

EXPERIMENTAL

839   0.13   AIR

R2 SLIDER (STANDARD)

1491   0.19

3354   0.26

13418 0.53

θp
(μrad)

140

105

70

35

0

0   0.25   0.50   0.75 h_t (μm)

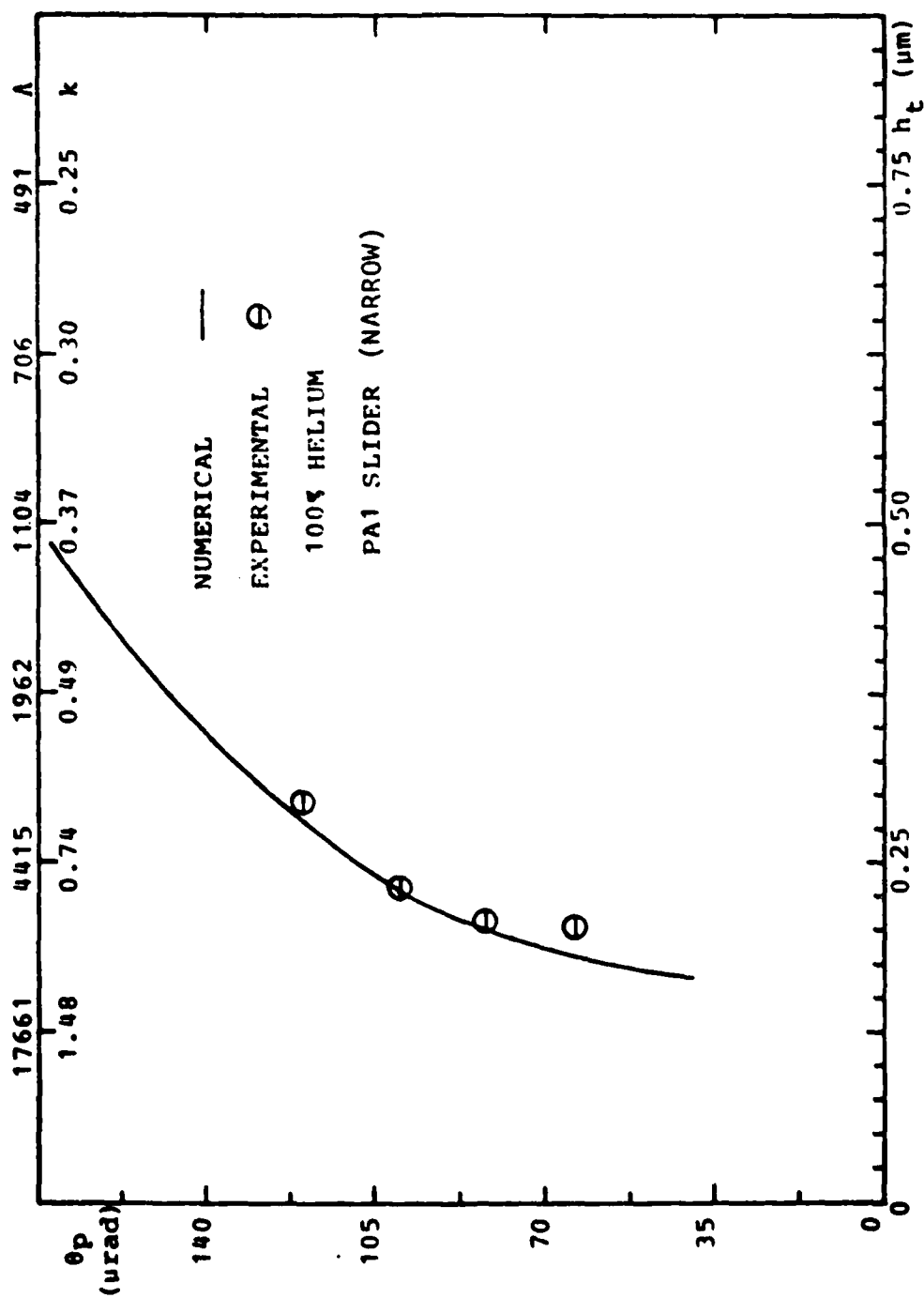FIGURE 11-36:   PITCH ANGLE VS TRAILING EDGE CLEARANCE, U = 36.13 m/sec

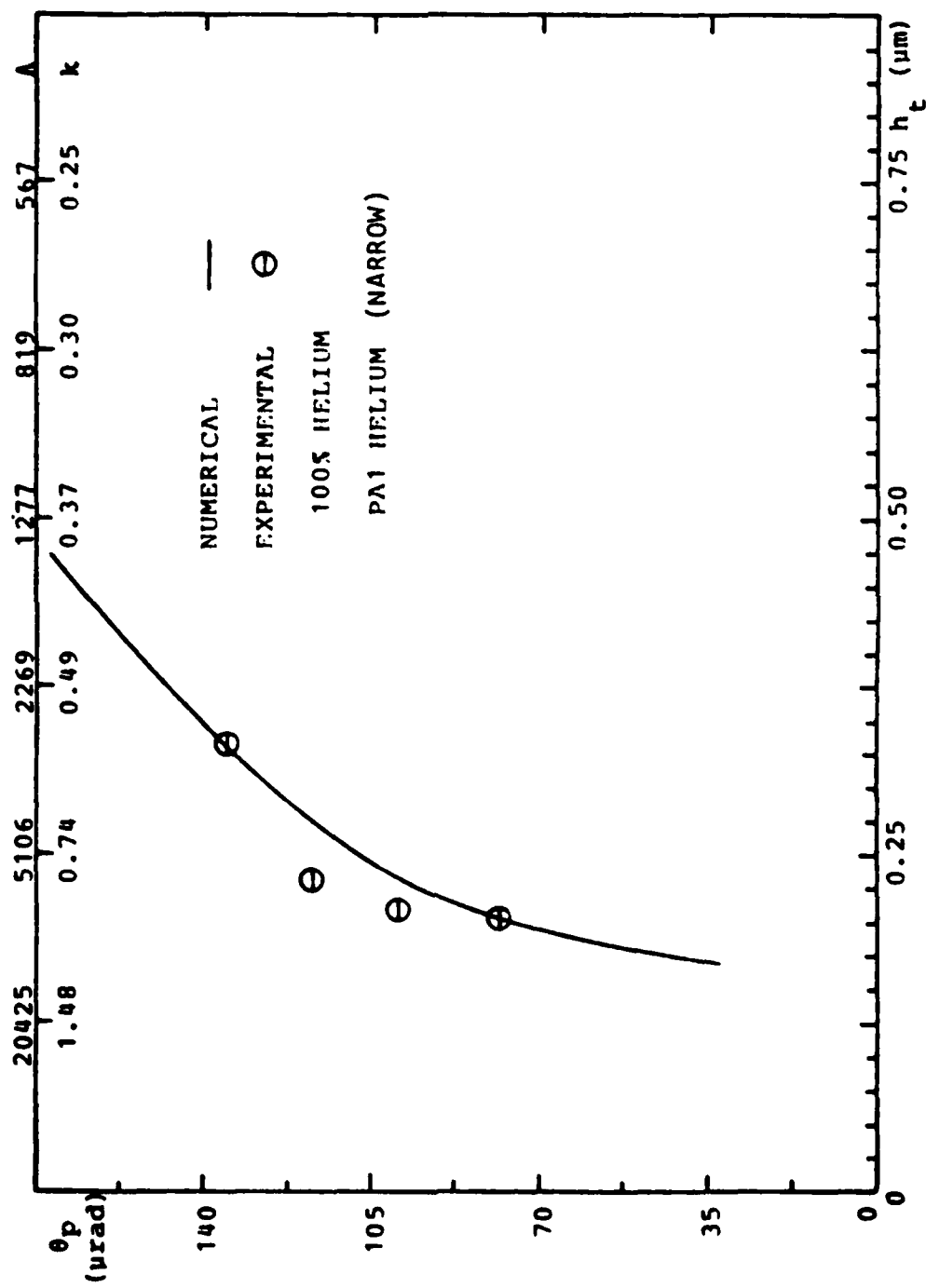FIGURE 11-37: PITCH ANGLE VS TRAILING EDGE CLEARANCE, U = 44.88 m/sec
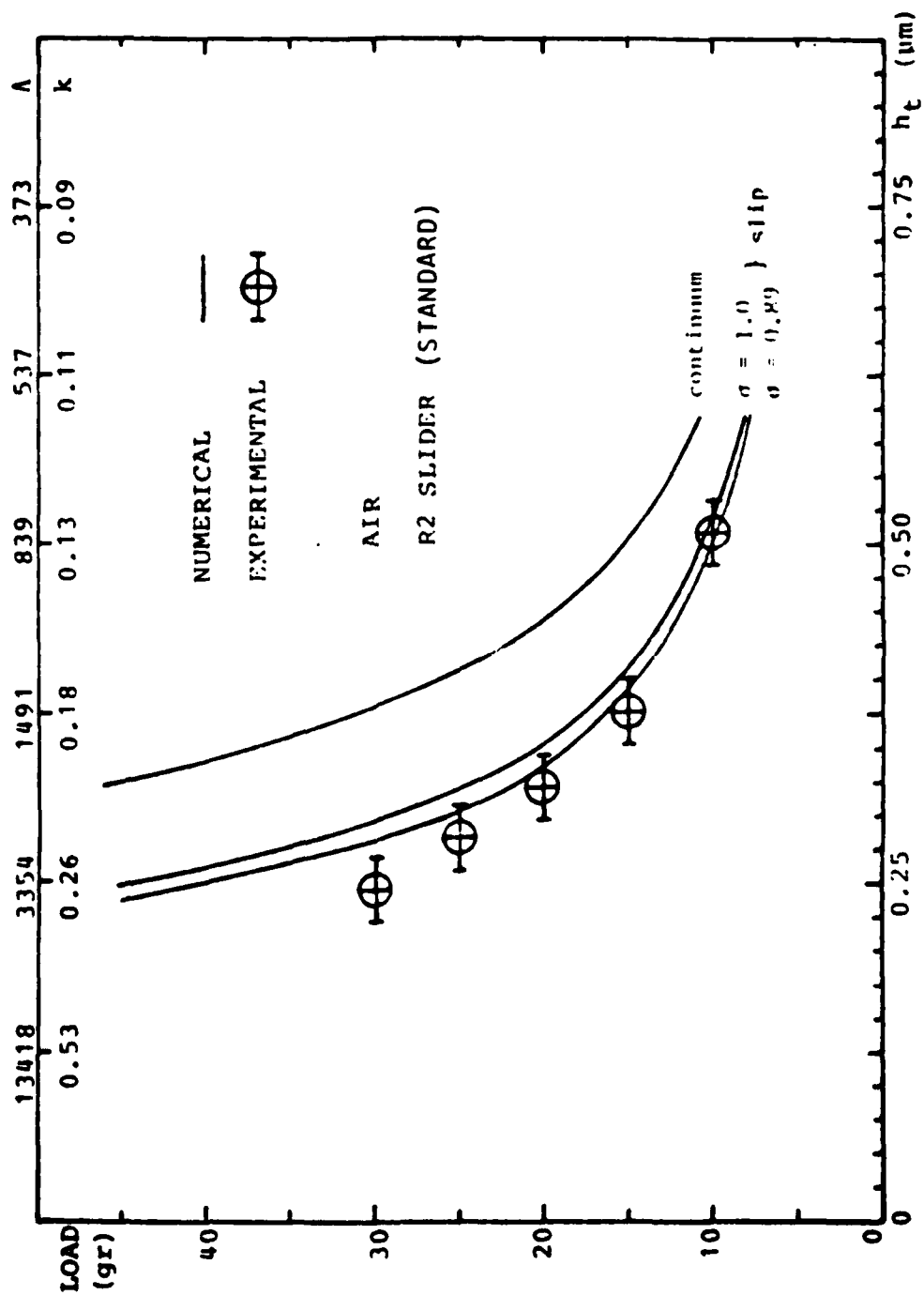
FIGURE 11-38: PITCH ANGLE VS TRAILING EDGE CLEARANCE, U = 51.90 m/sec

FIGURE 11-39 : LOAD VS TRAILING EDGE CLEARANCE, U = 17.43 m/sec

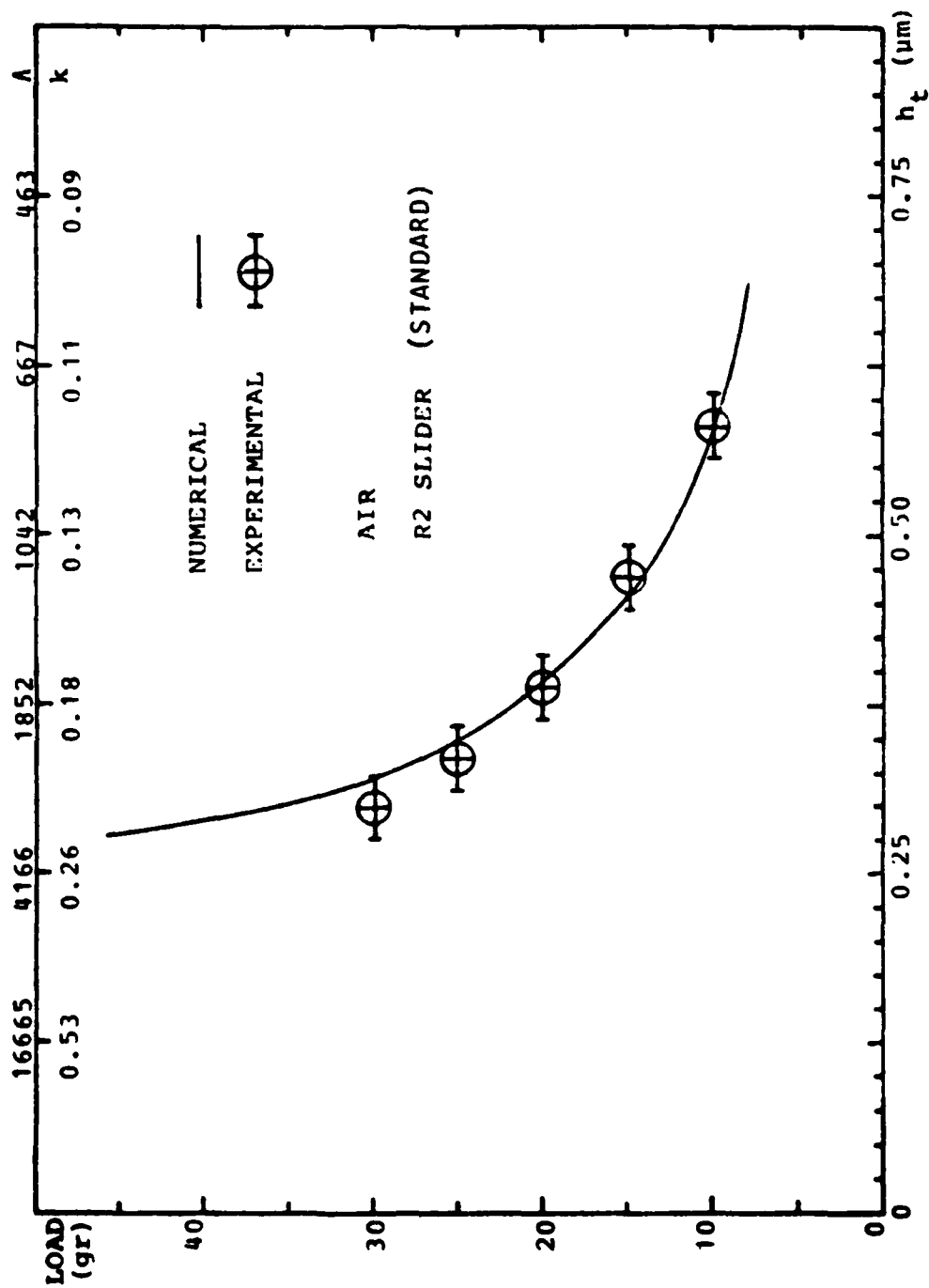FIGURE 11-40: LOAD VS TRAILING EDGE CLEARANCE. U = 24.59 m/sec
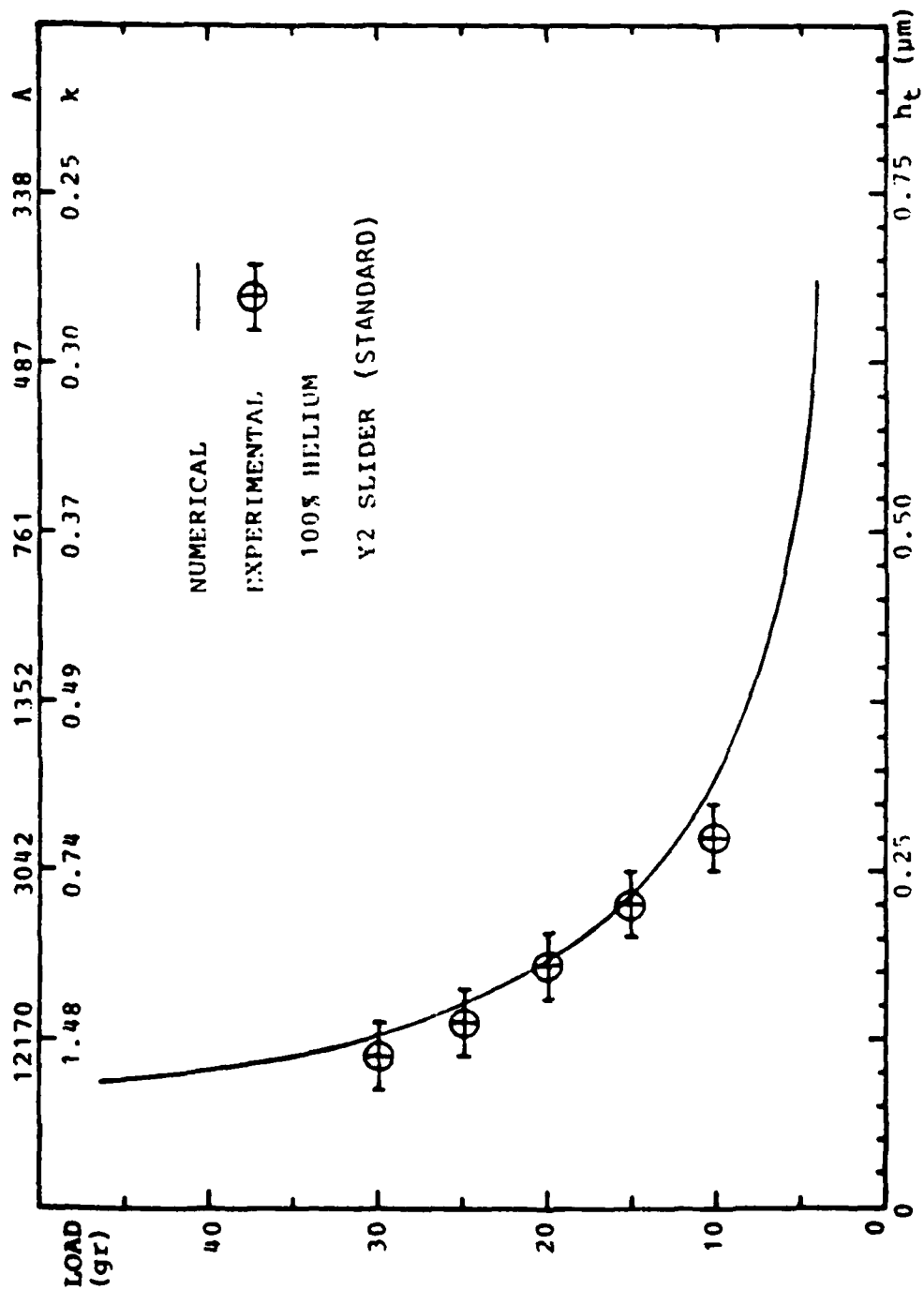
FIGURE 11-41:   LOAD VS TRAILING EDGE CLEARANCE, U = 30.53 m/sec

2·2

END
DATE
FILMED
9 80
DTIC

1.0

1.1

1.25   1.4   1.6

2.8   2.5

3.2   2.2

3.6

4.0   2.0

1.8

MICROCOPY RESOLUTION TEST CHART
NATIONAL BUREAU OF STANDARDS 1963-A
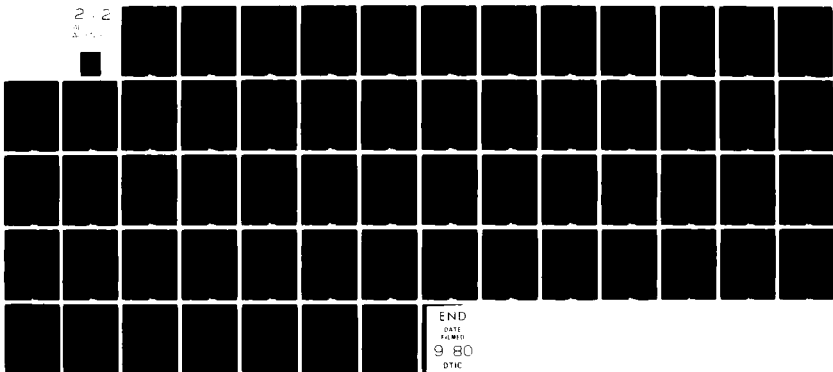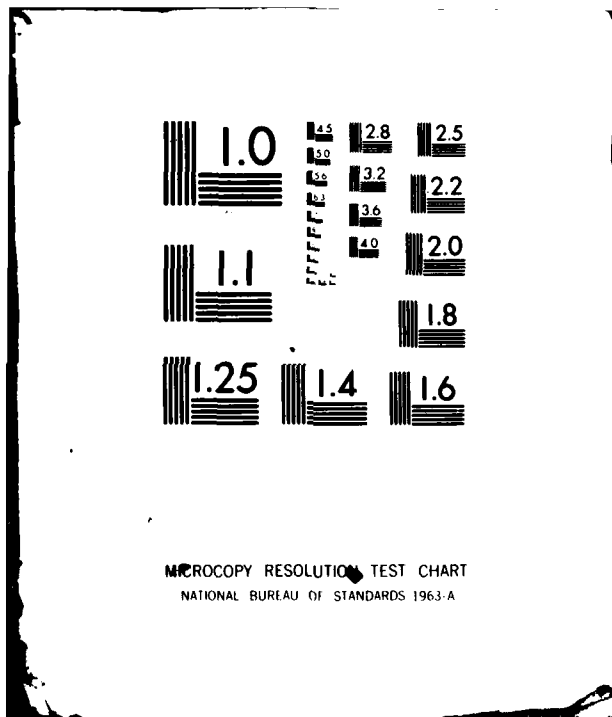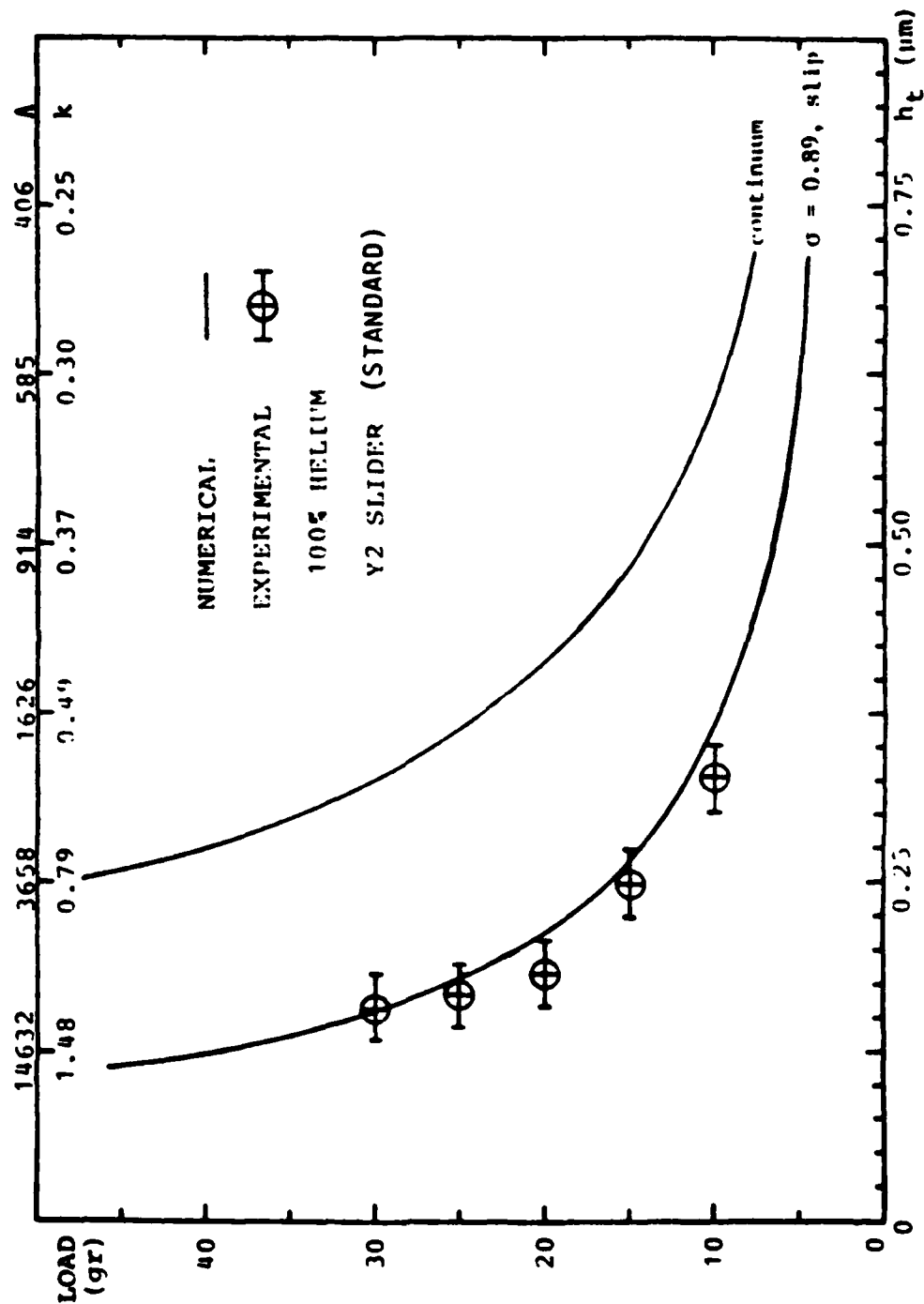
FIGURE 11-42 : LOAD VS TRAILING EDGE CLEARANCE, U = 36.71 m/sec
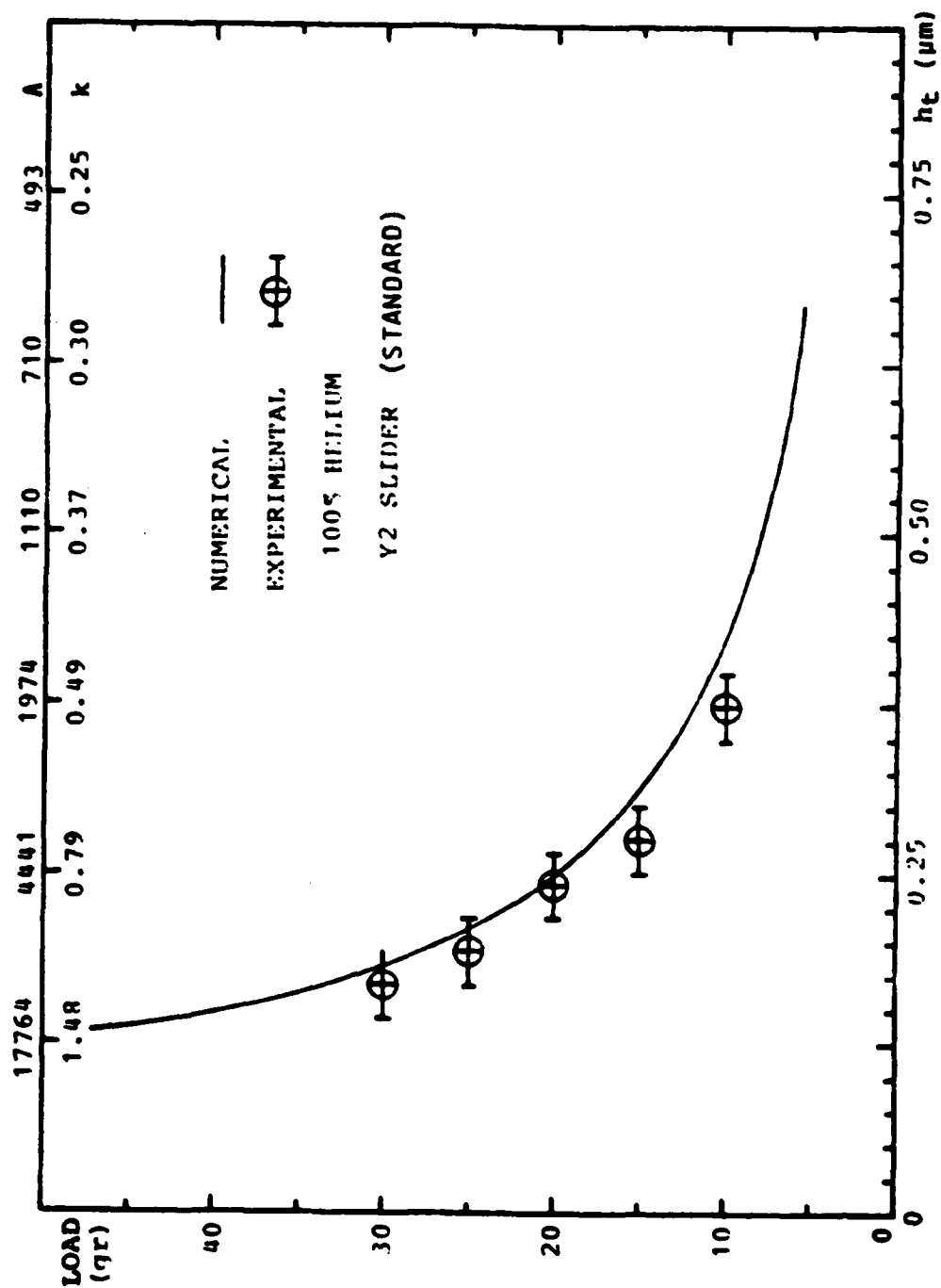
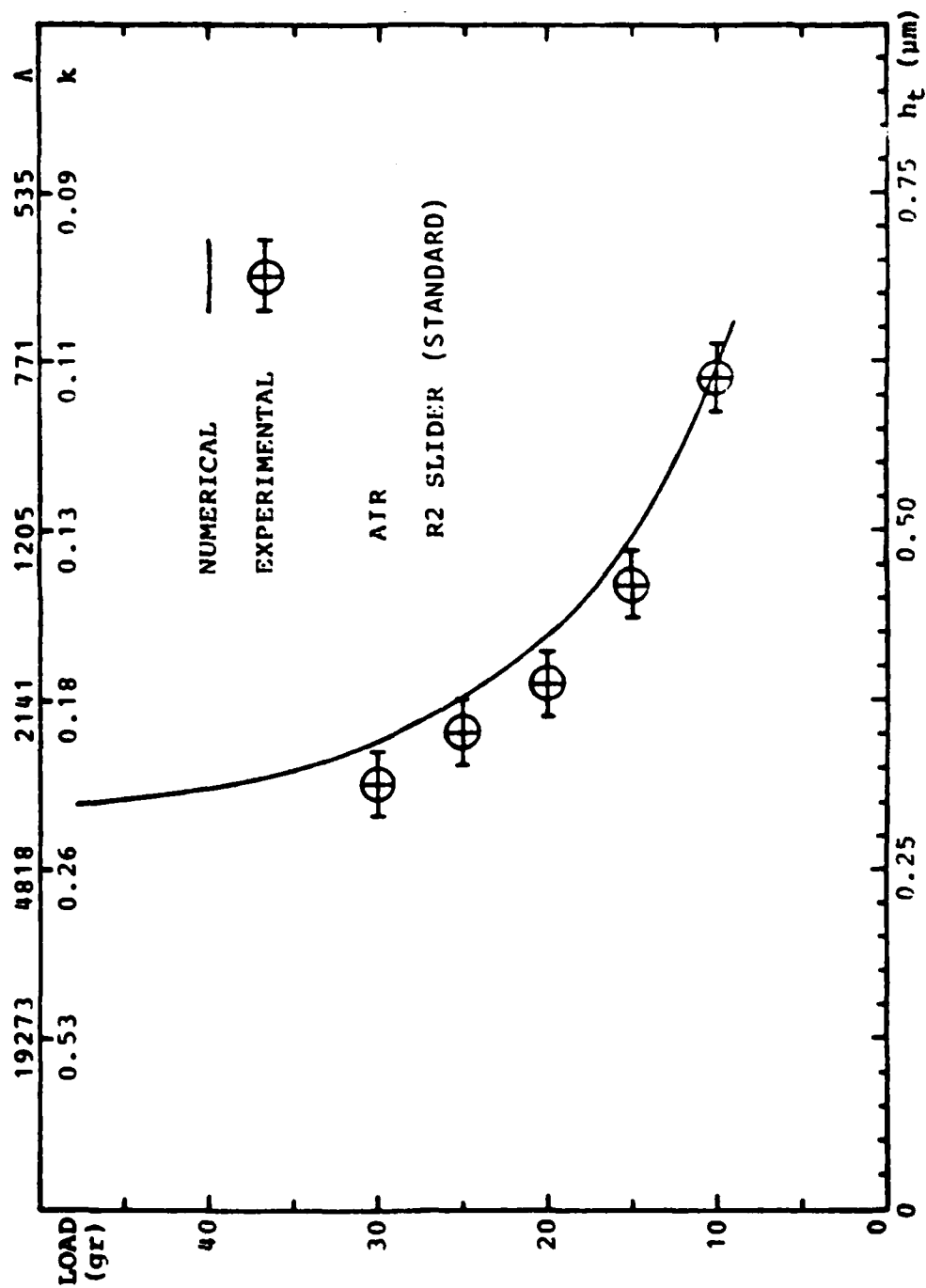FIGURE 11-43: LOAD VS TRAILING EDGE CLEARANCE, U = 44.56 m/sec
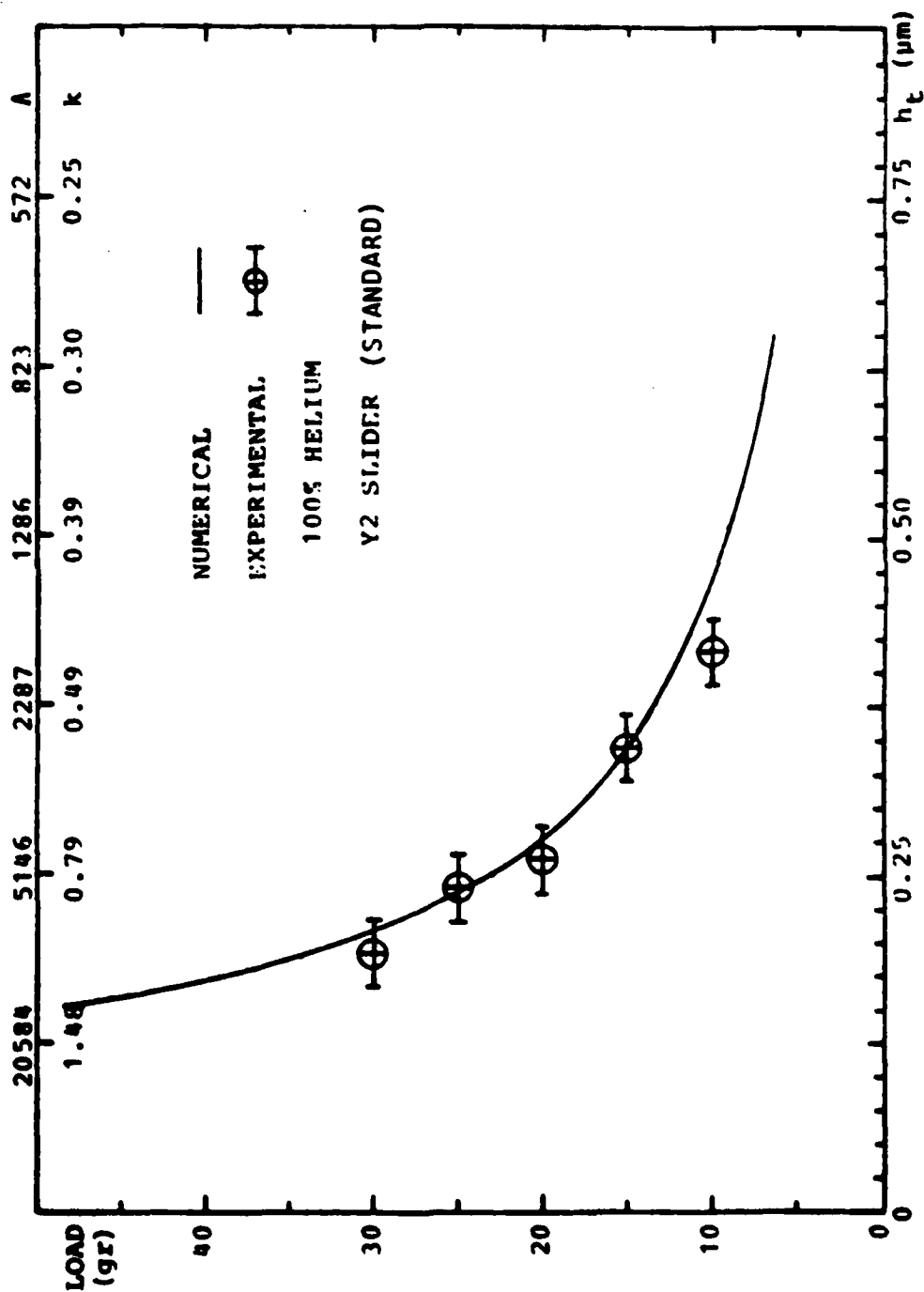
FIGURE 11-44 : LOAD VS TRAILING EDGE CLEARANCE, U = 51.63 m/sec
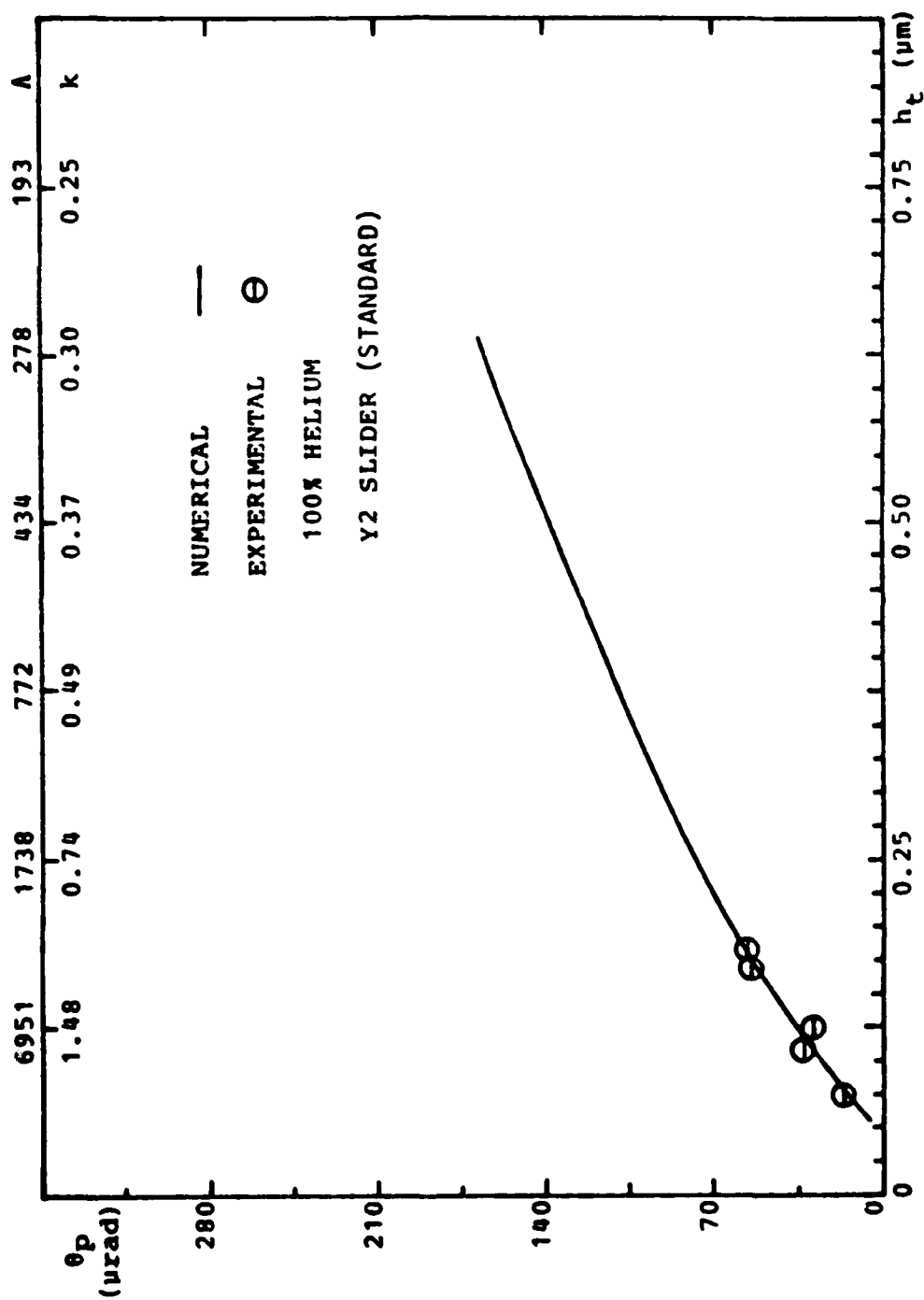
FIGURE 11-45: PITCH ANGLE VS TRAILING EDGE CLEARANCE, U = 17.43 m/sec
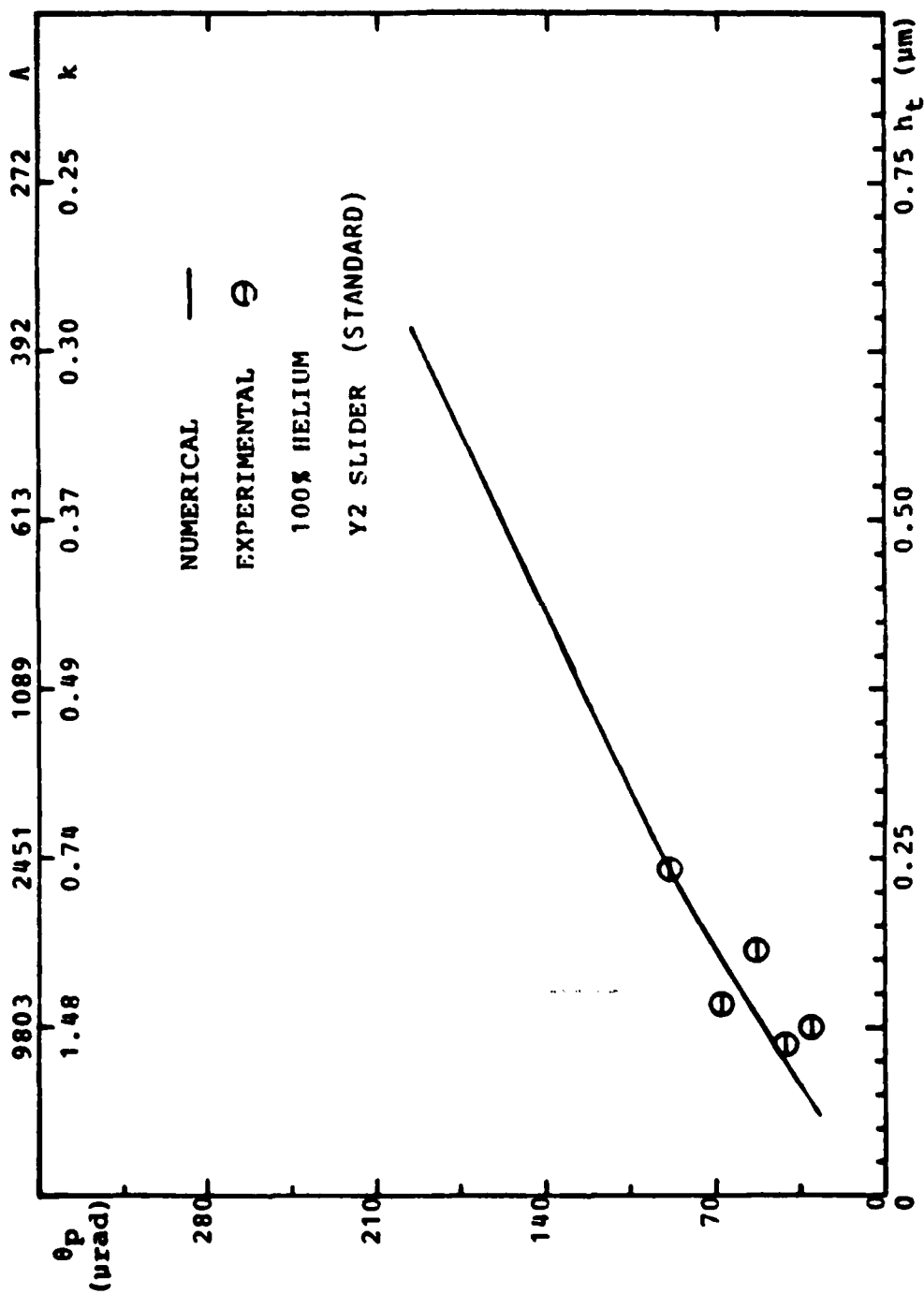
FIGURE 11-46 : PITCH ANGLE VS TRAILING EDGE CLEARANCE, U = 24.59 m/sec
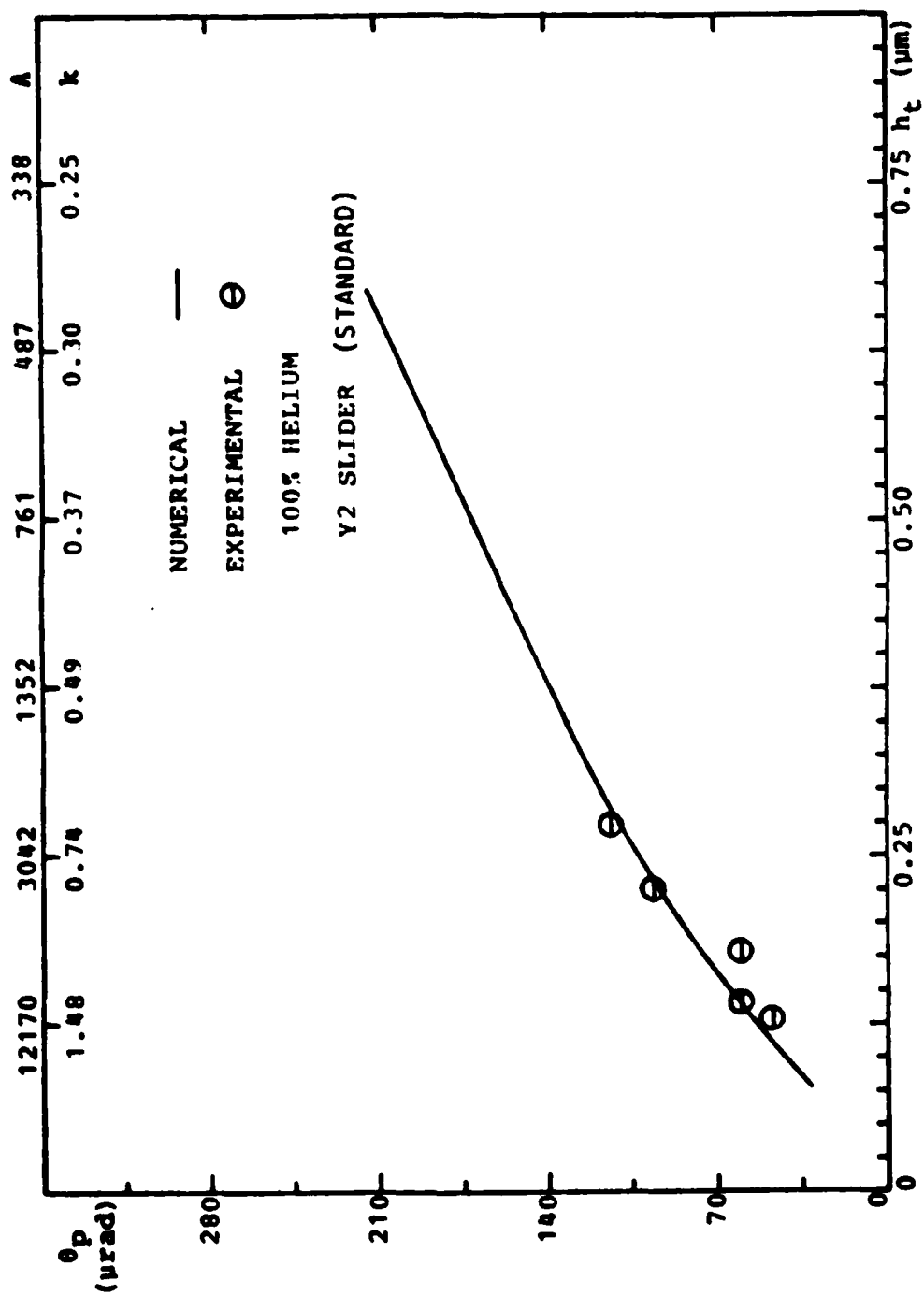
FIGURE 11-47 : PITCH ANGLE VS TRAILING EDGE CLEARANCE, U = 30.54 m/sec
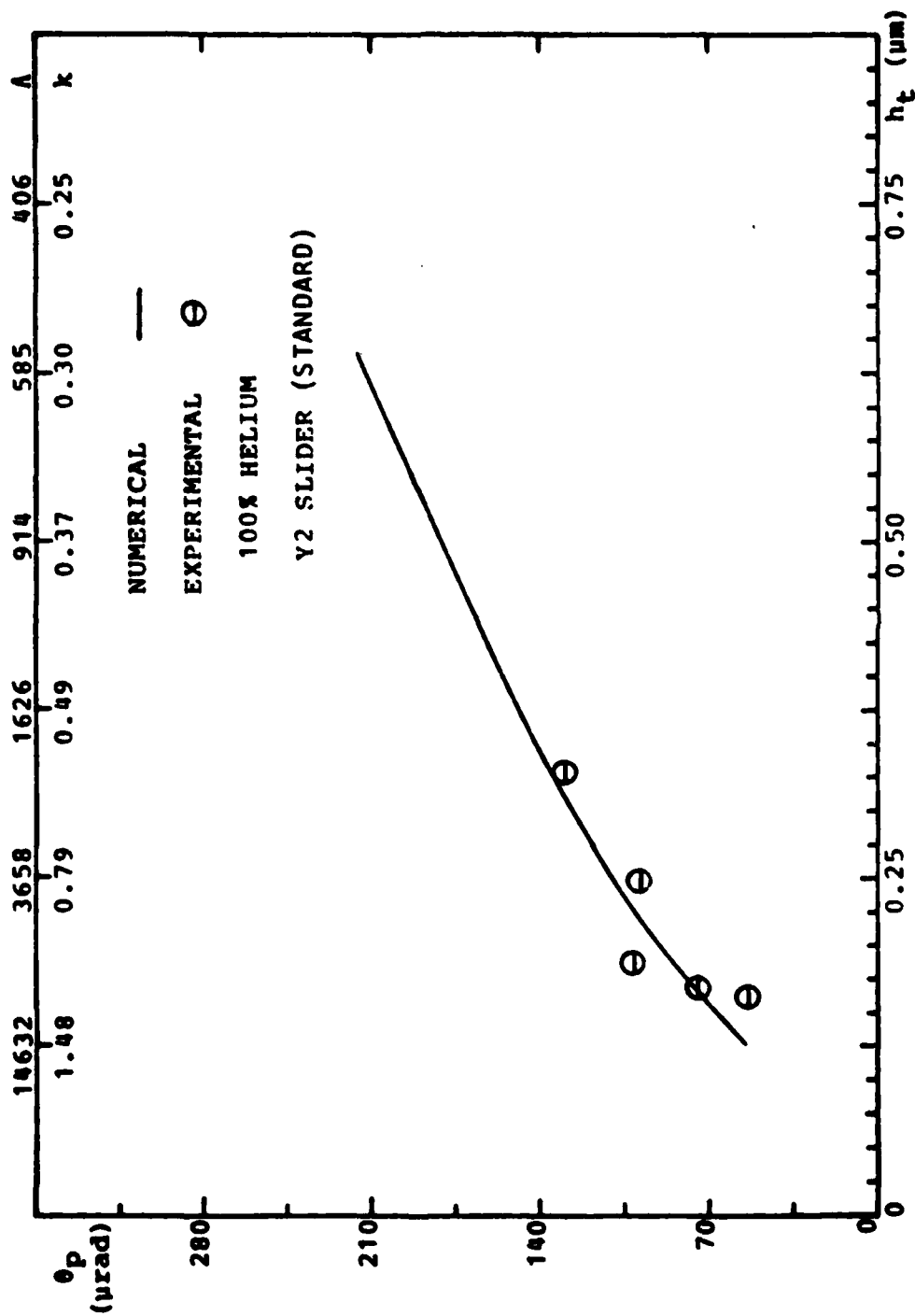
FIGURE 11-48: PITCH ANGLE VS TRAILING EDGE CLEARANCE, U = 36.71 m/sec
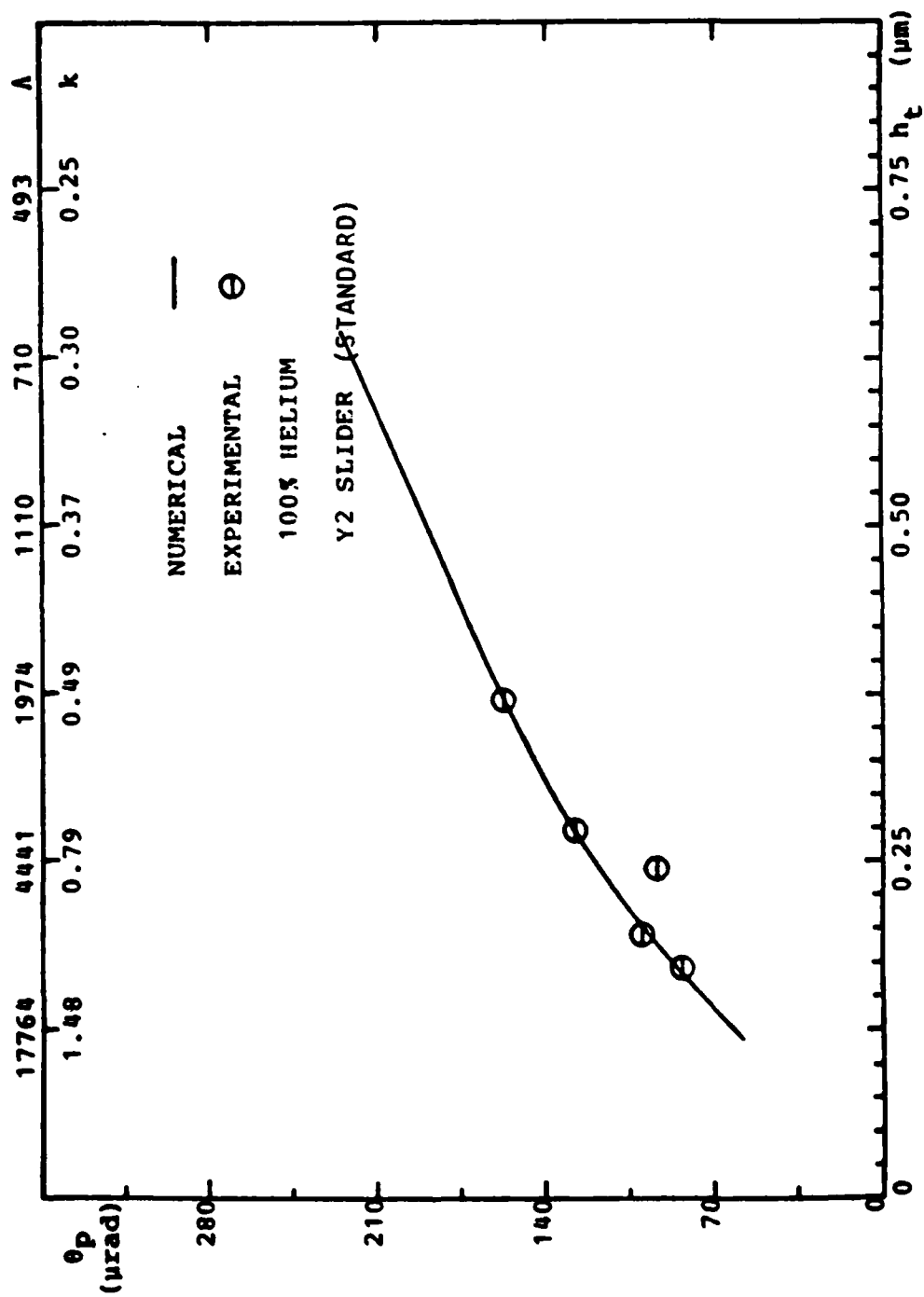
FIGURE 11-49: PITCH ANGLE VS TRAILING EDGE CLEARANCE, U = 44.56 m/sec
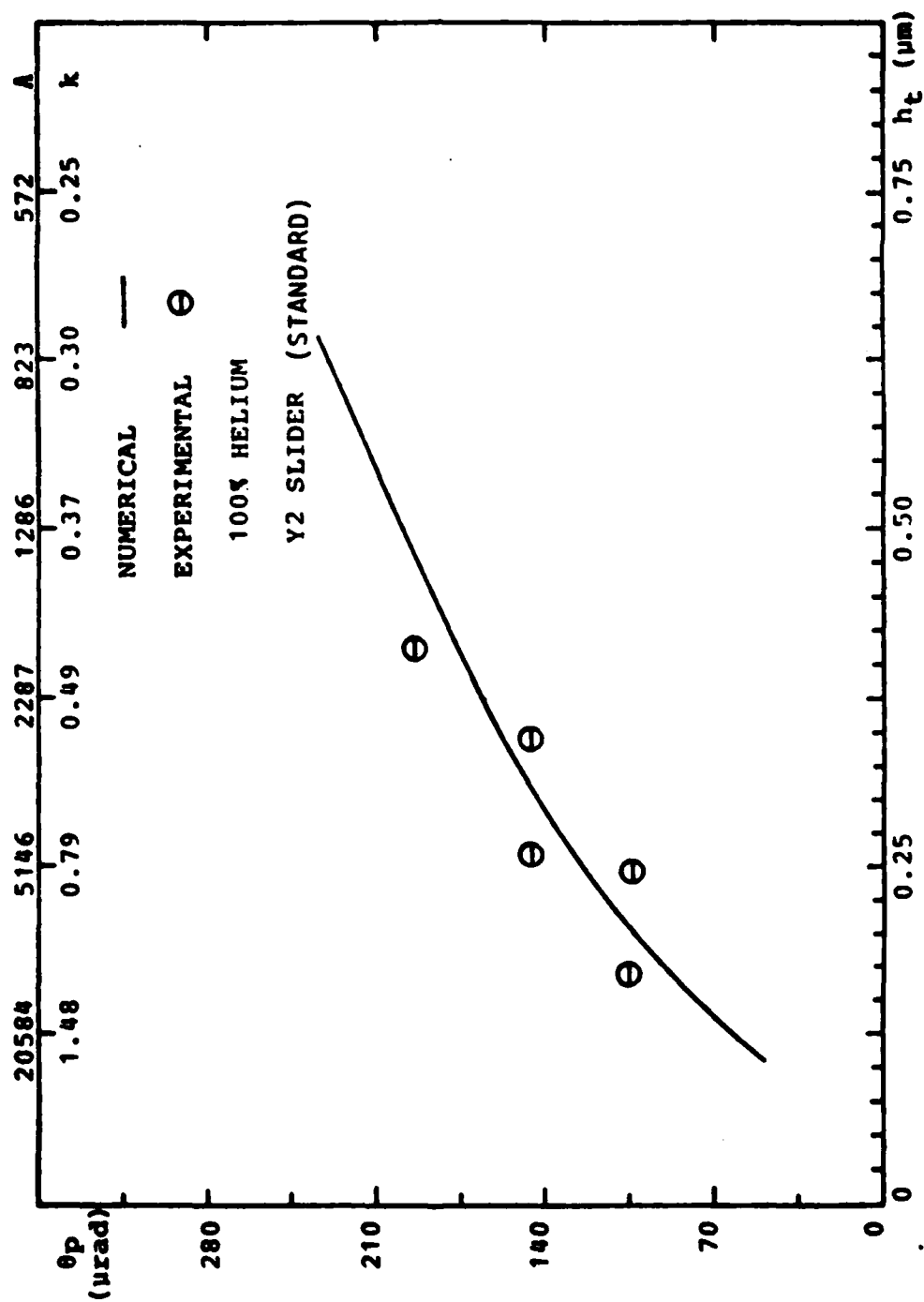
FIGURE 11-50: PITCH ANGLE VS TRAILING EDGE CLEARANCE, U = 51.63 m/sec
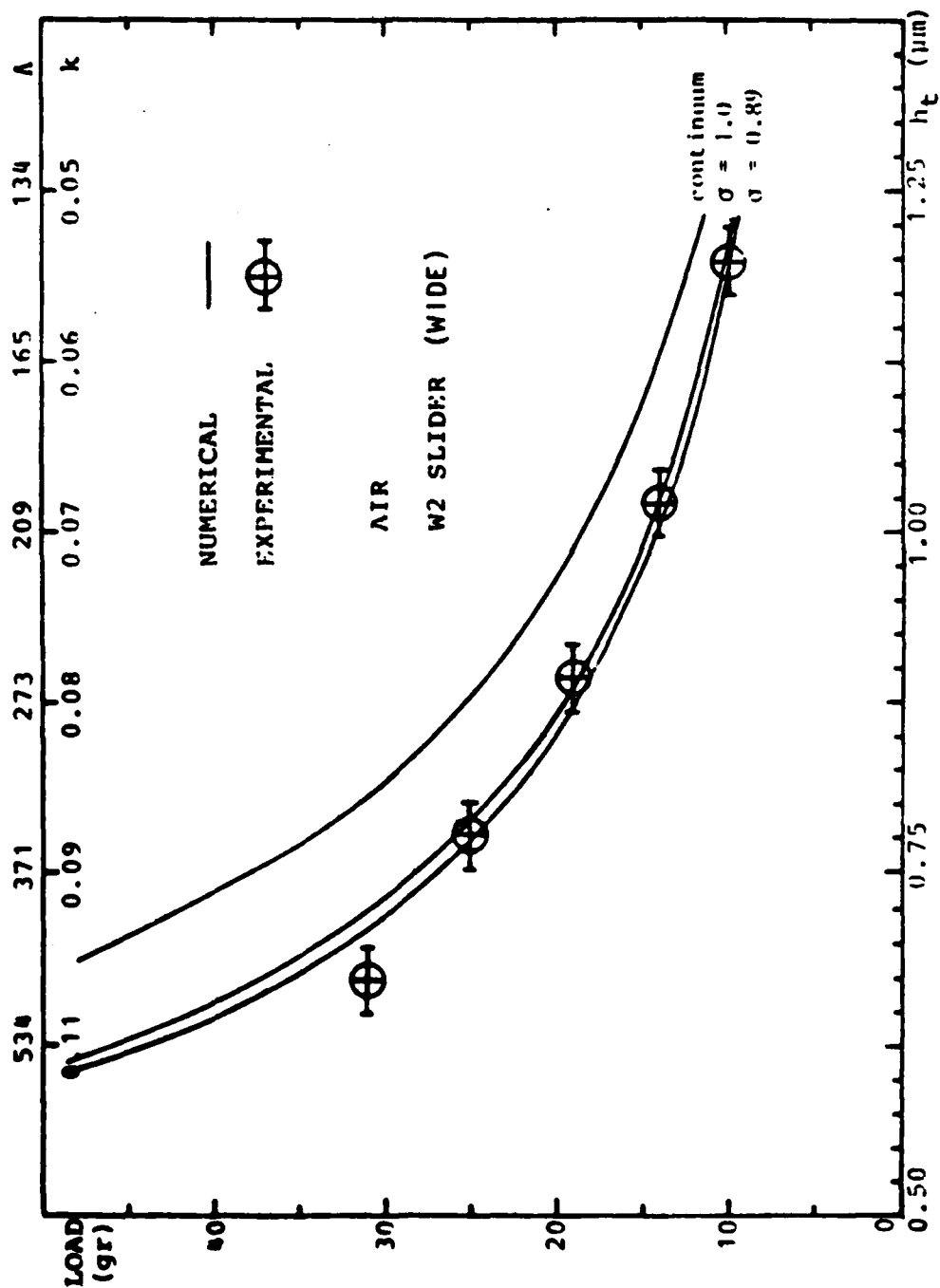
FIGURE 11-51: LOAD VS TRAILING EDGE CLEARANCE, U = 36.13 m/sec
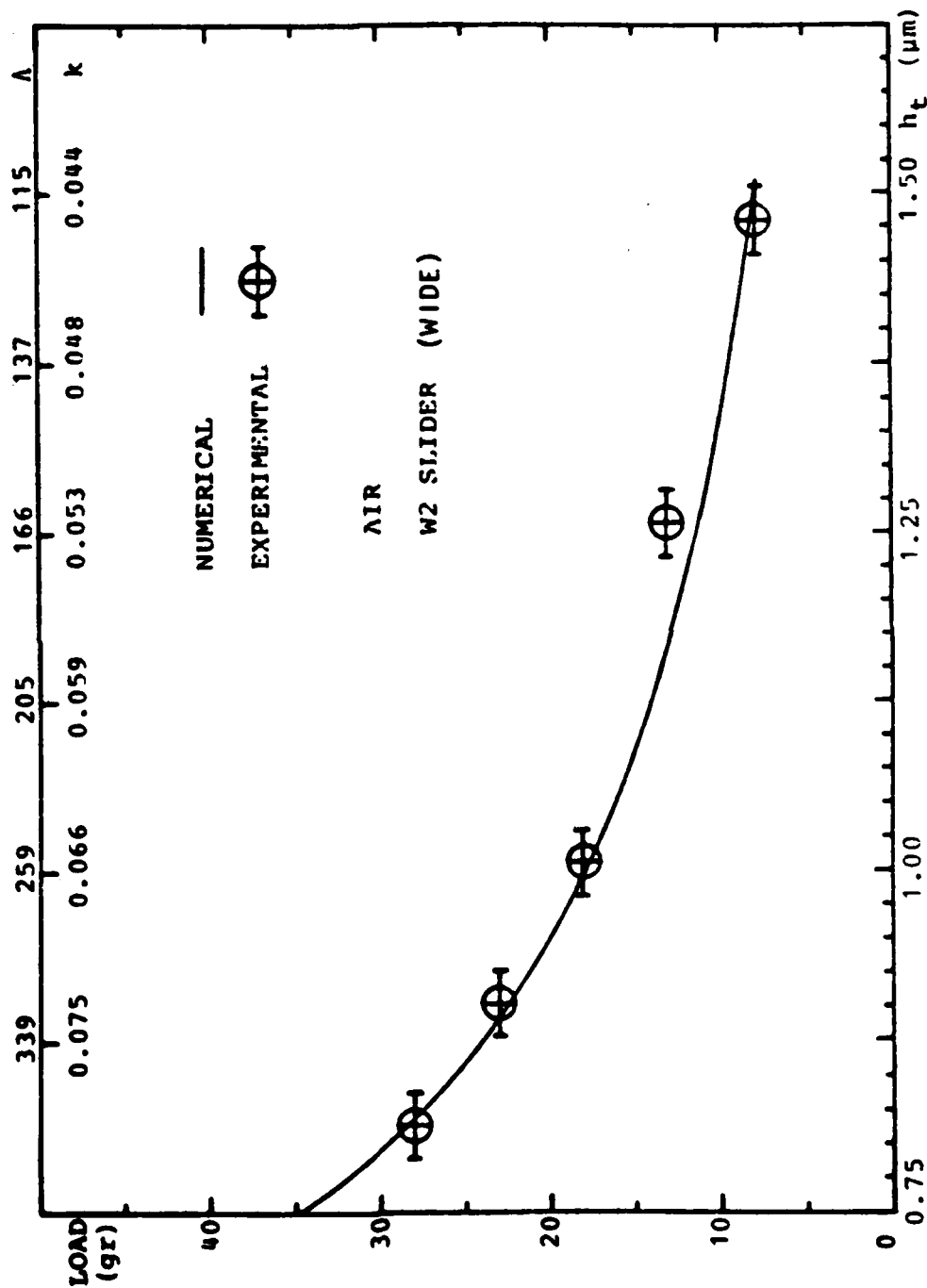
FIGURE 11-52: LOAD VS TRAILING EDGE CLEARANCE, U = 44.88 m/sec
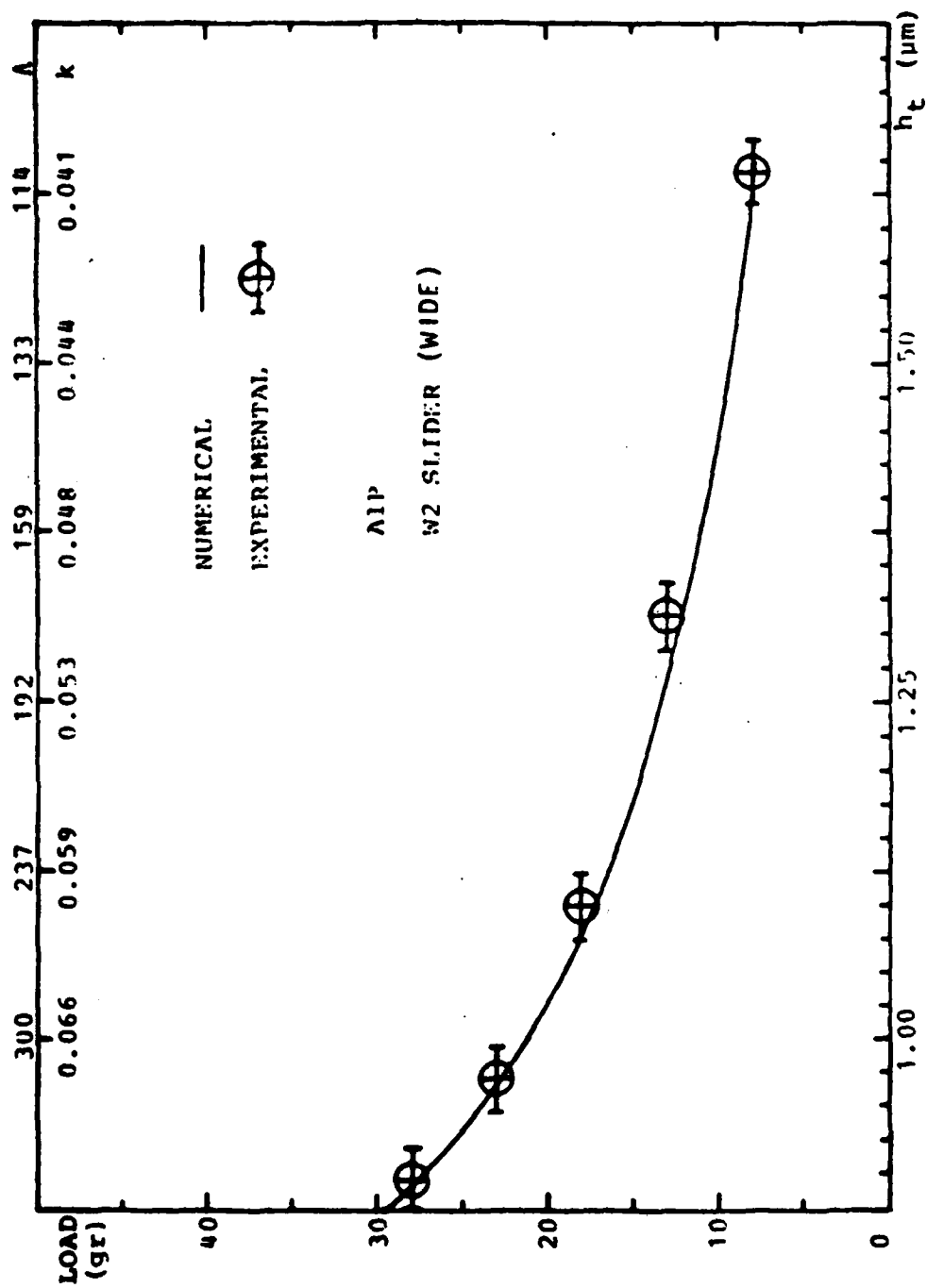
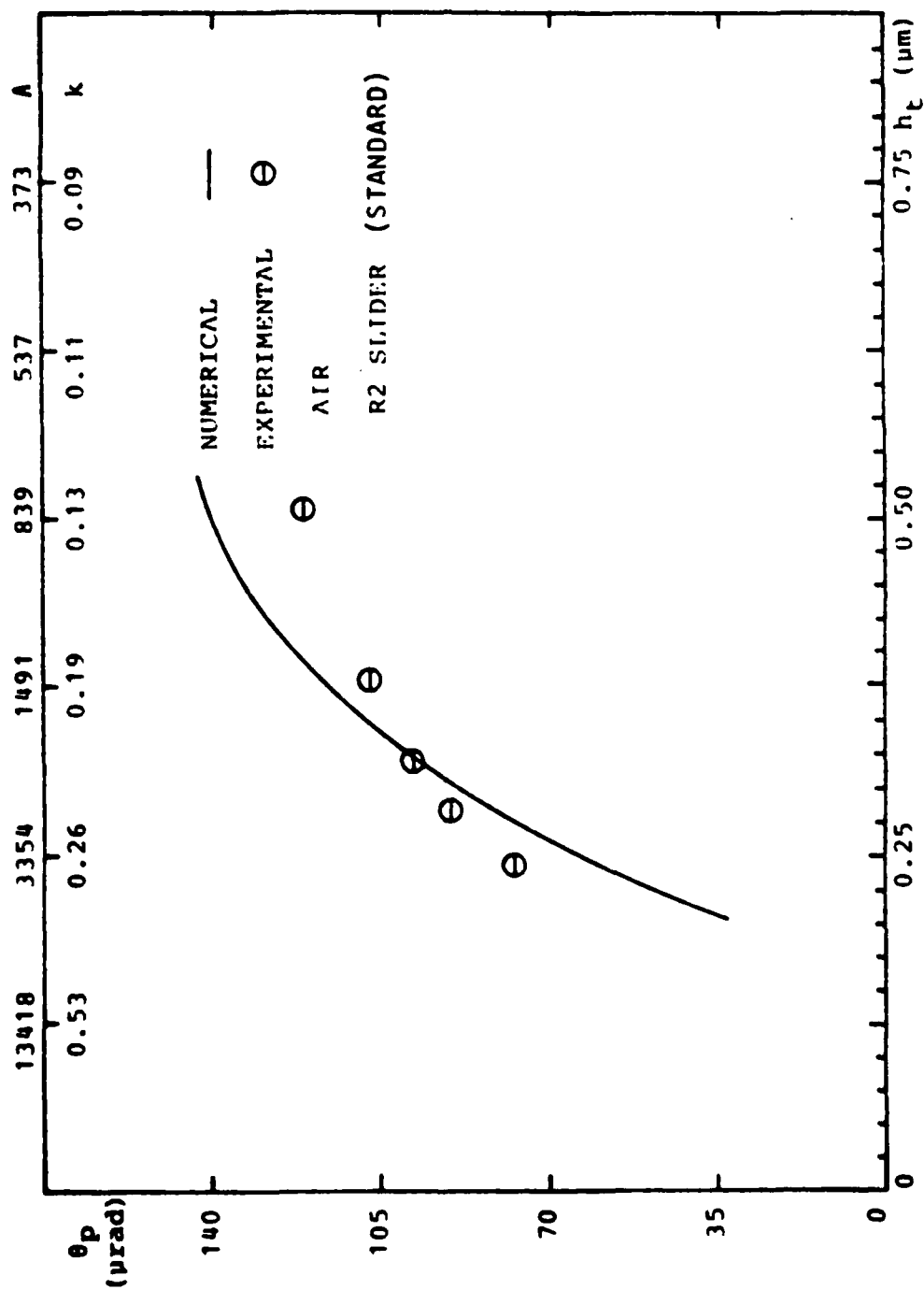FIGURE 11-53: LOAD VS TRAILING EDGE CLEARANCE, U = 51.90 m/sec
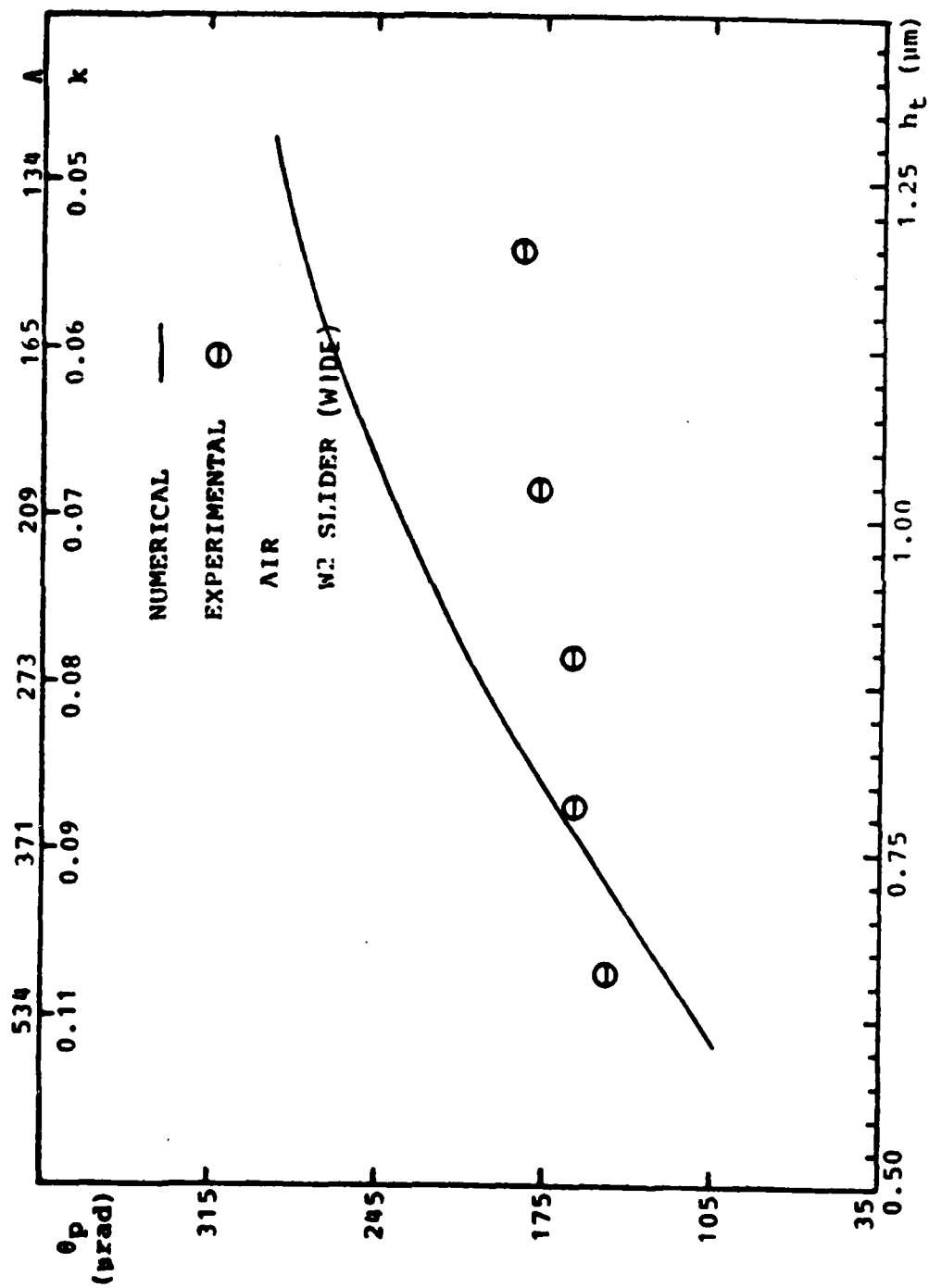
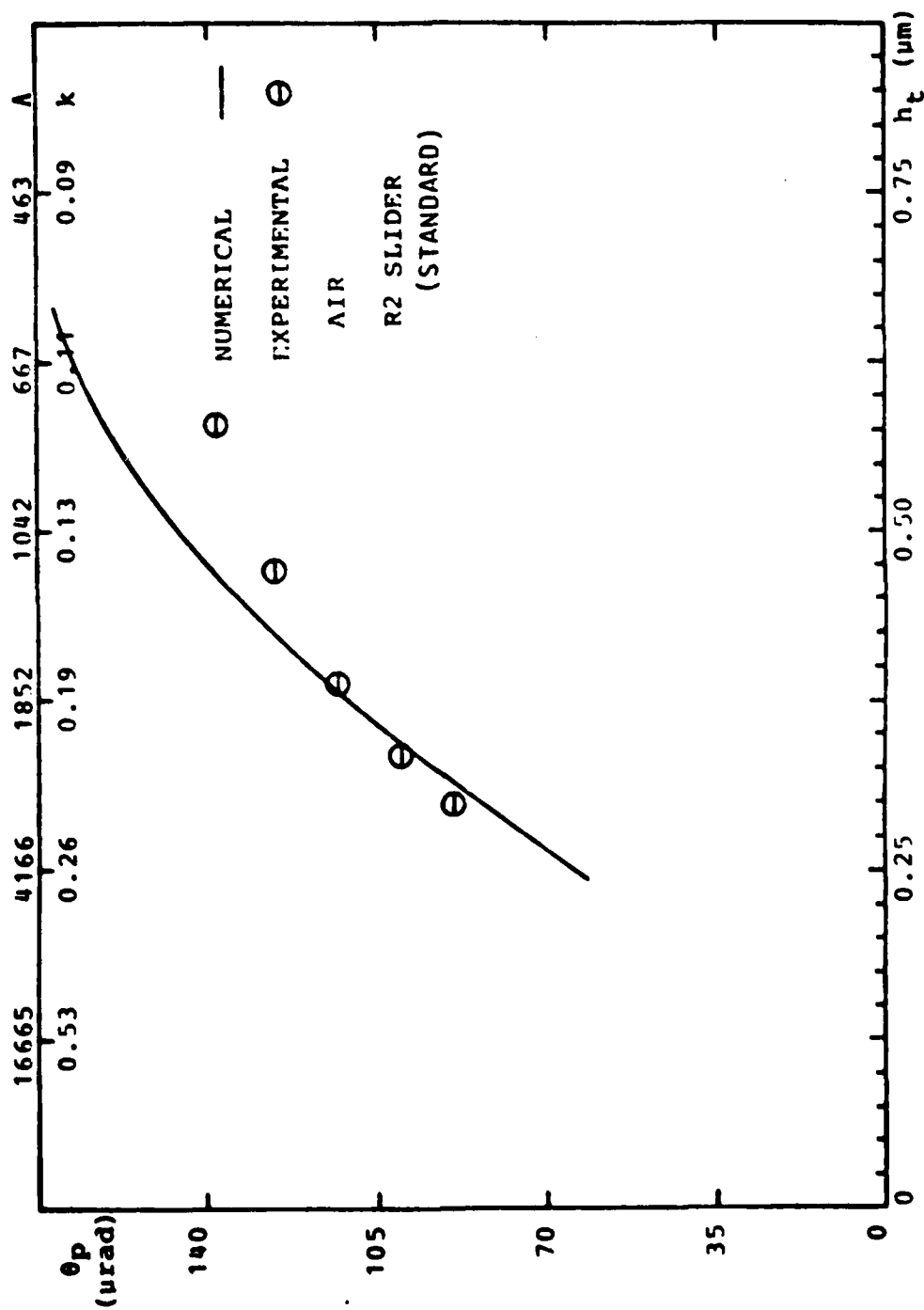FIGURE 11-54: PITCH ANGLE VS TRAILING EDGE CLEARANCE, U = 36.13 m/sec
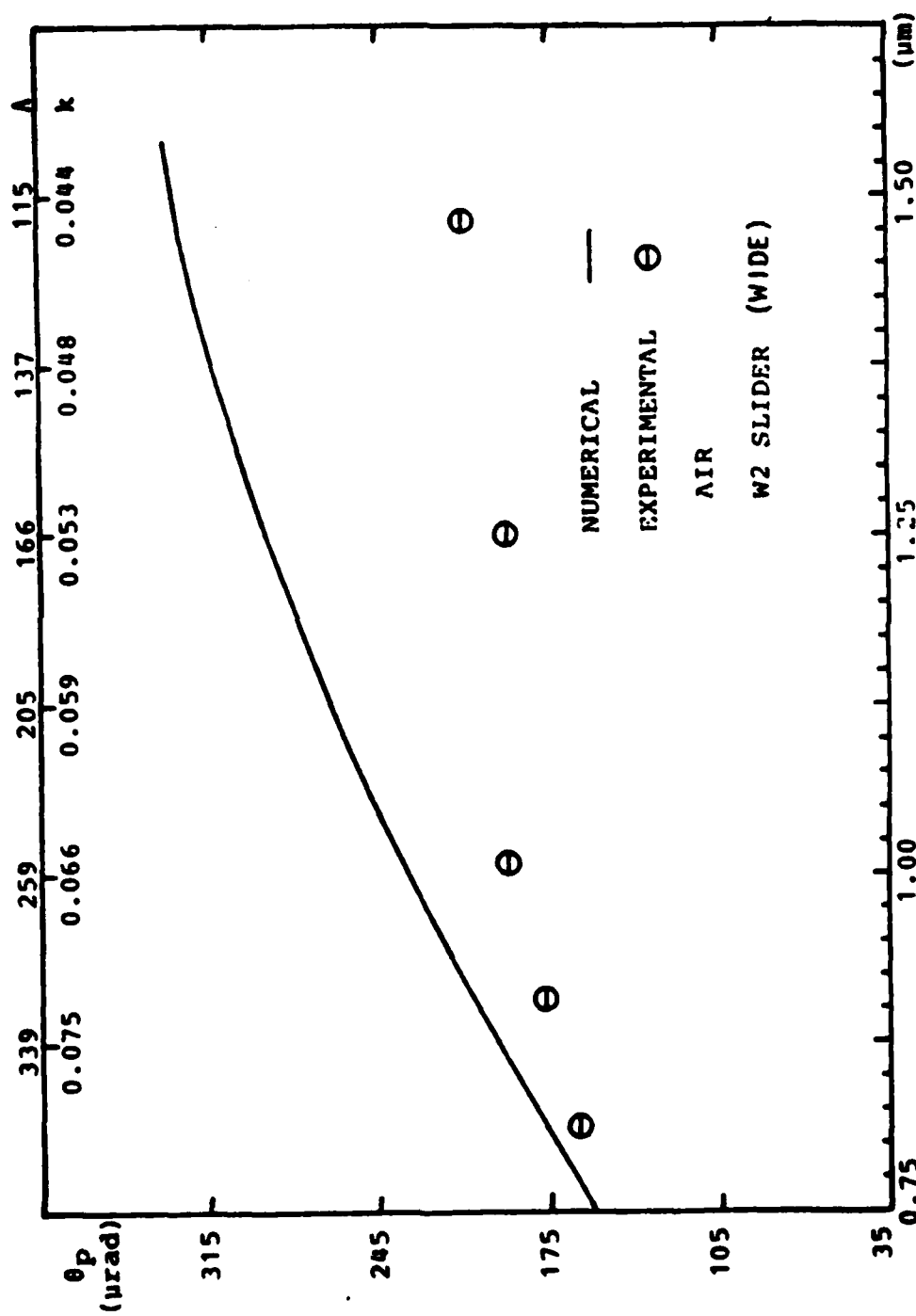
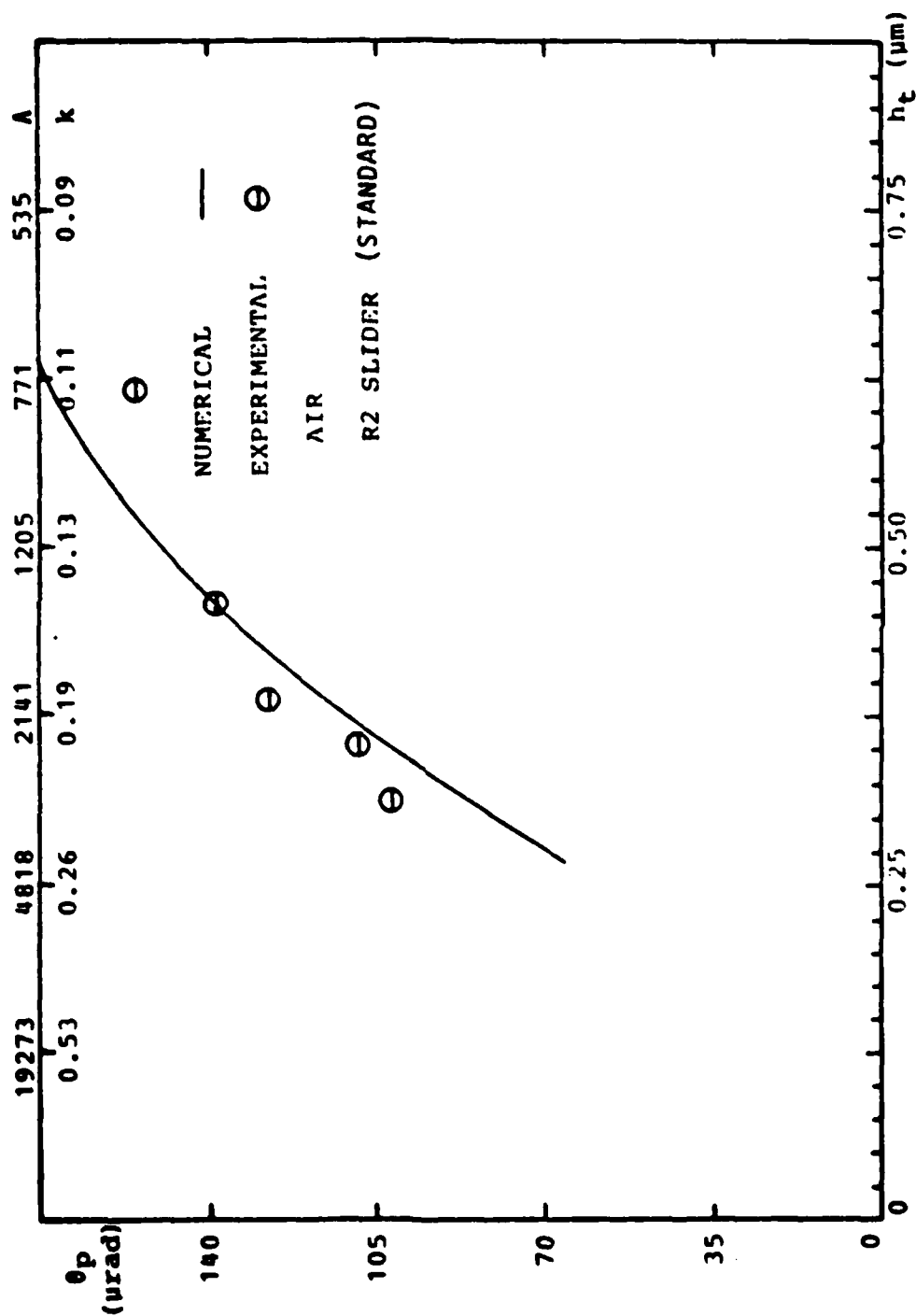FIGURE 11-55: PITCH ANGLE VS TRAILING EDGE CLEARANCE, U = 44.88 m/sec
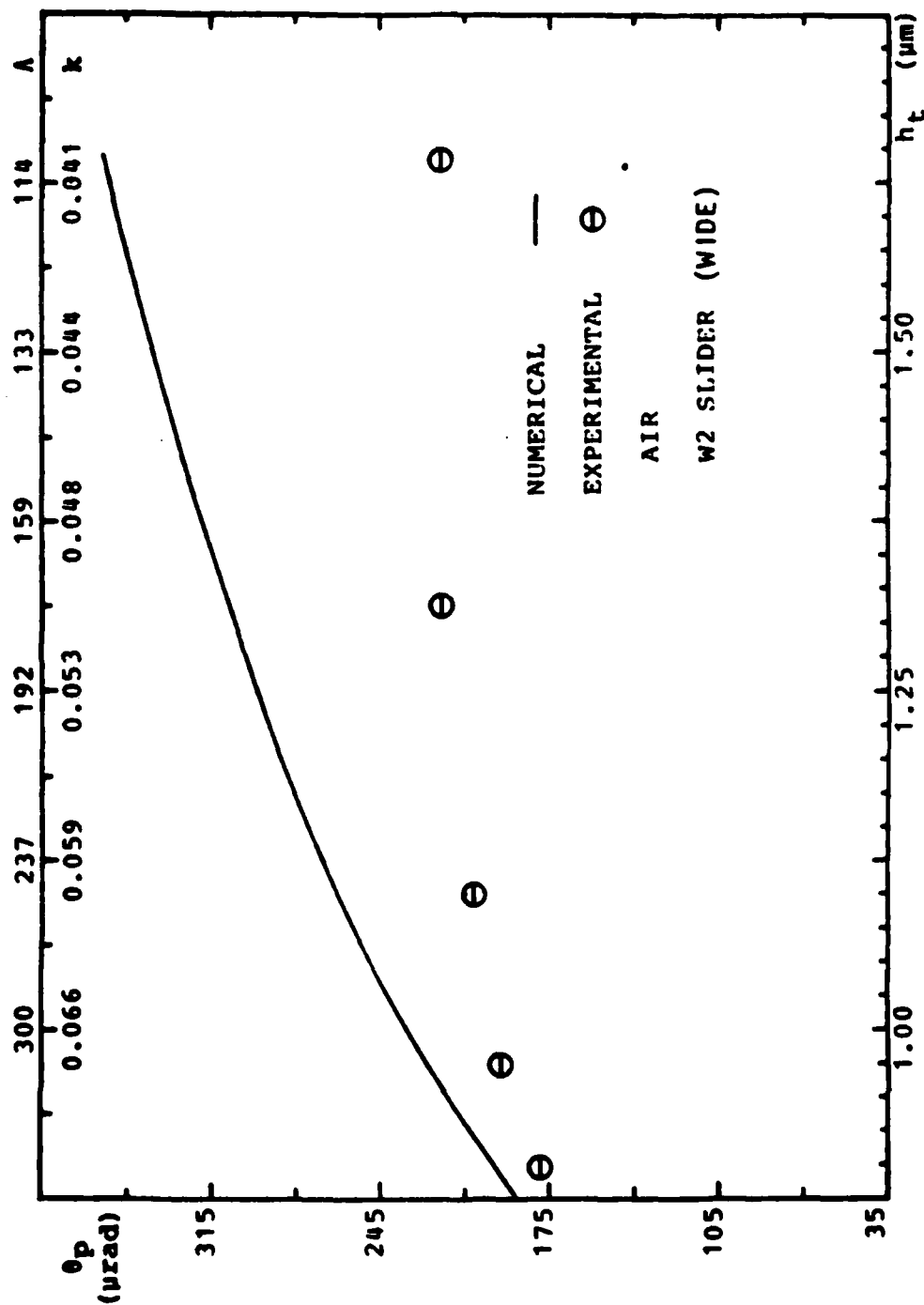
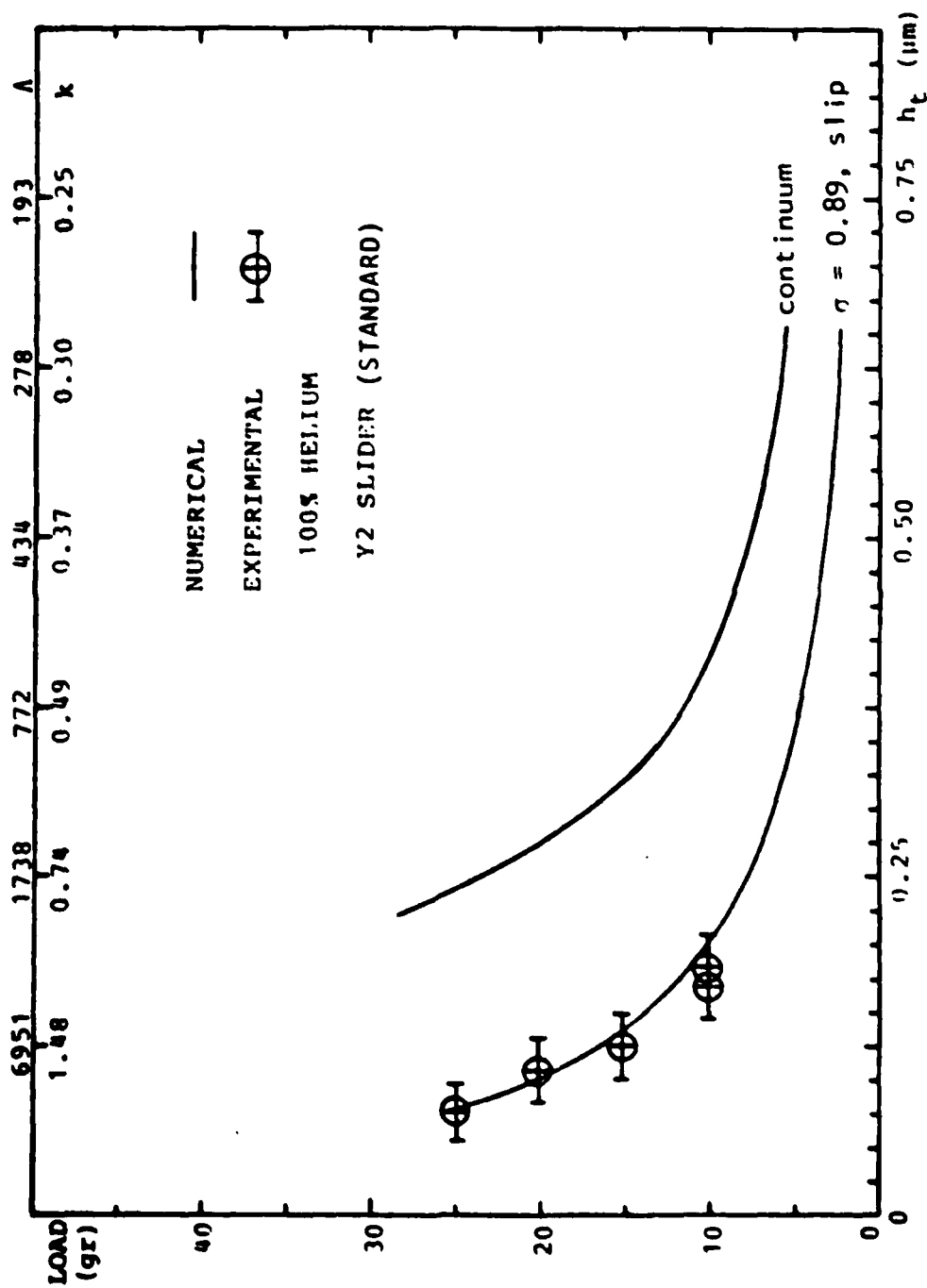FIGURE 11-56: PITCH ANGLE VS TRAILING EDGE CLEARANCE, U = 51.90 m/sec

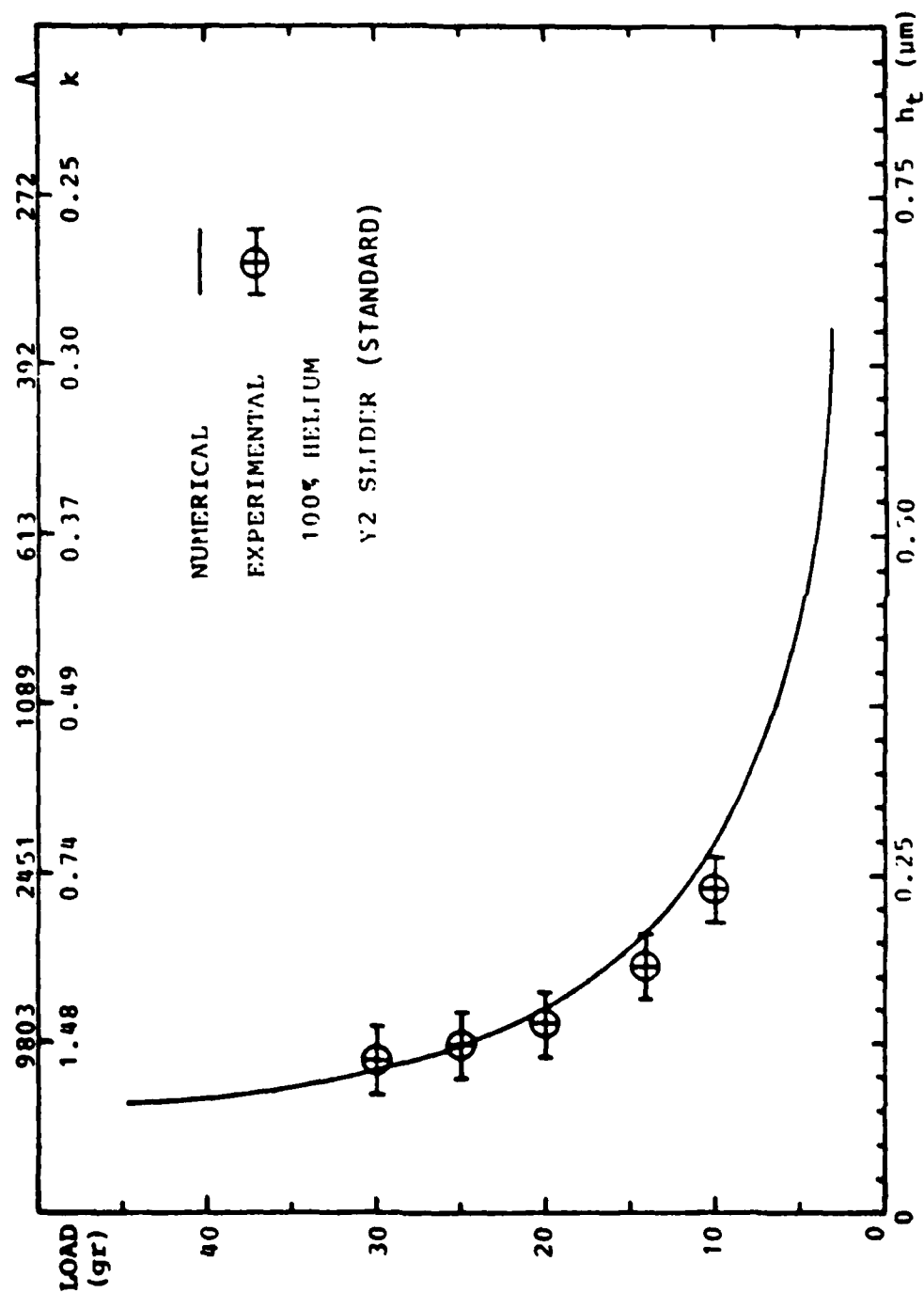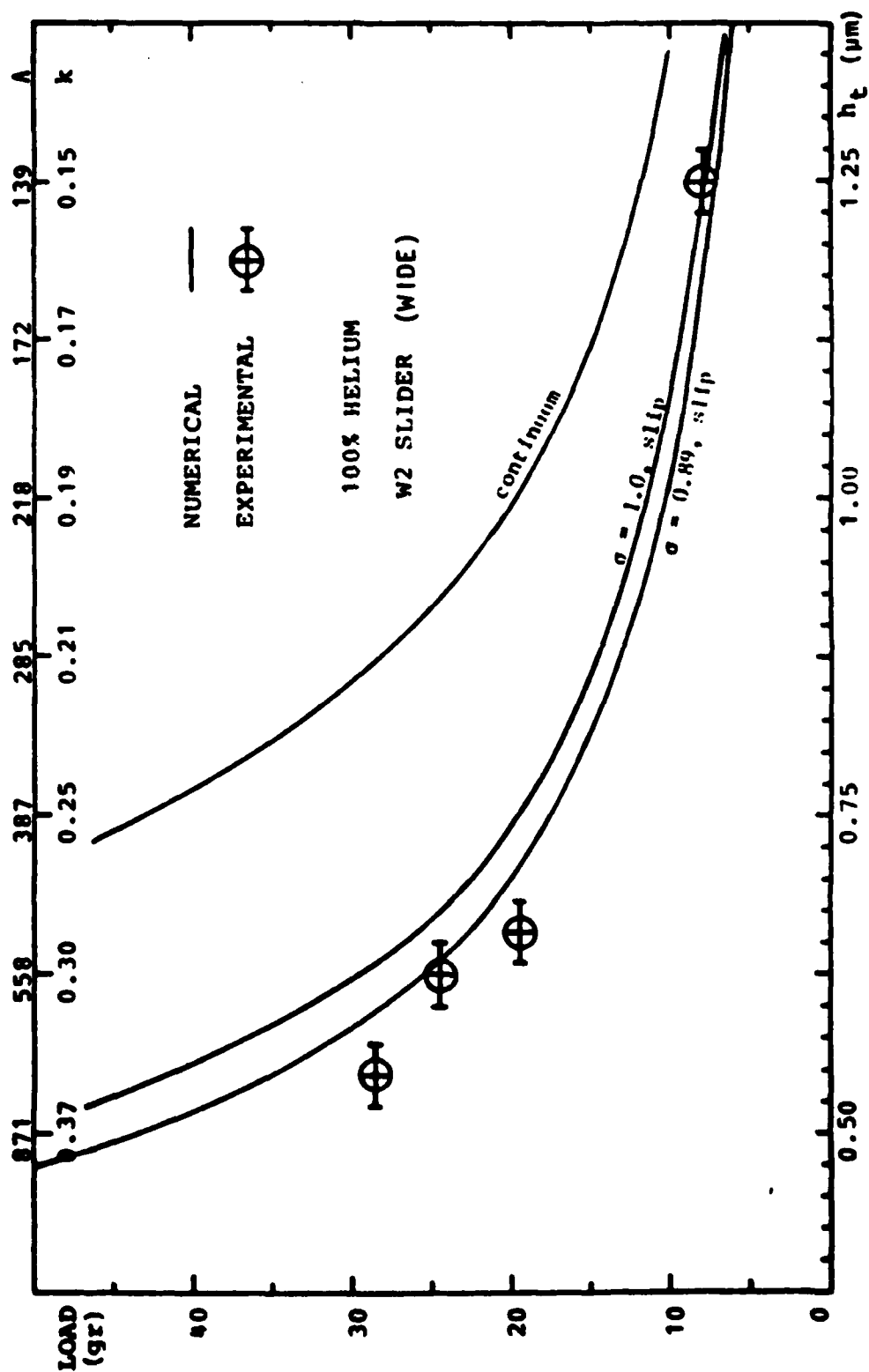FIGURE 11-57: LOAD VS TRAILING EDGE CLEARANCE, U = 35.35 m/sec
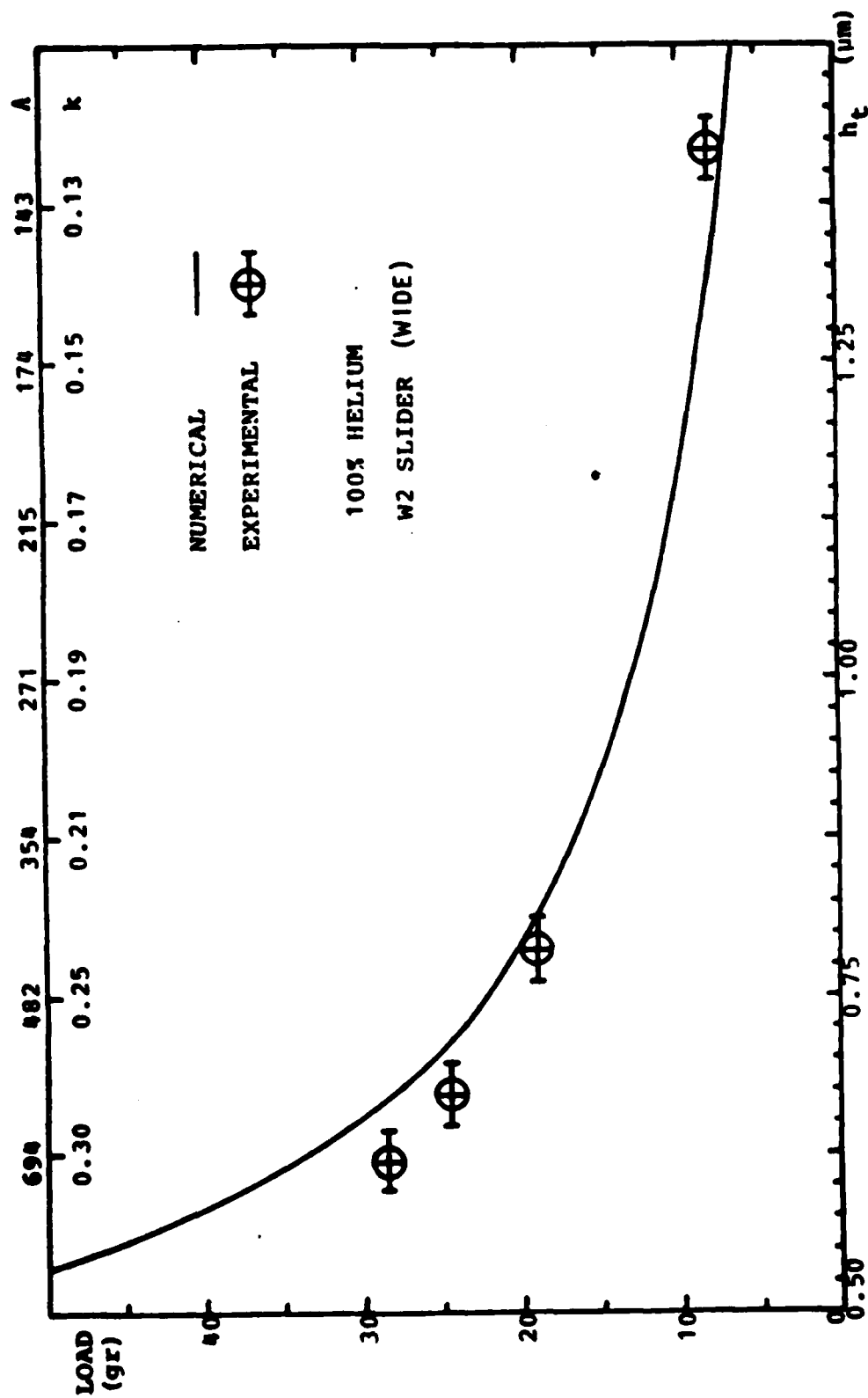
FIGURE 11-58: LOAD VS TRAILING EDGE CLEARANCE, U = 44.01 m/sec

108
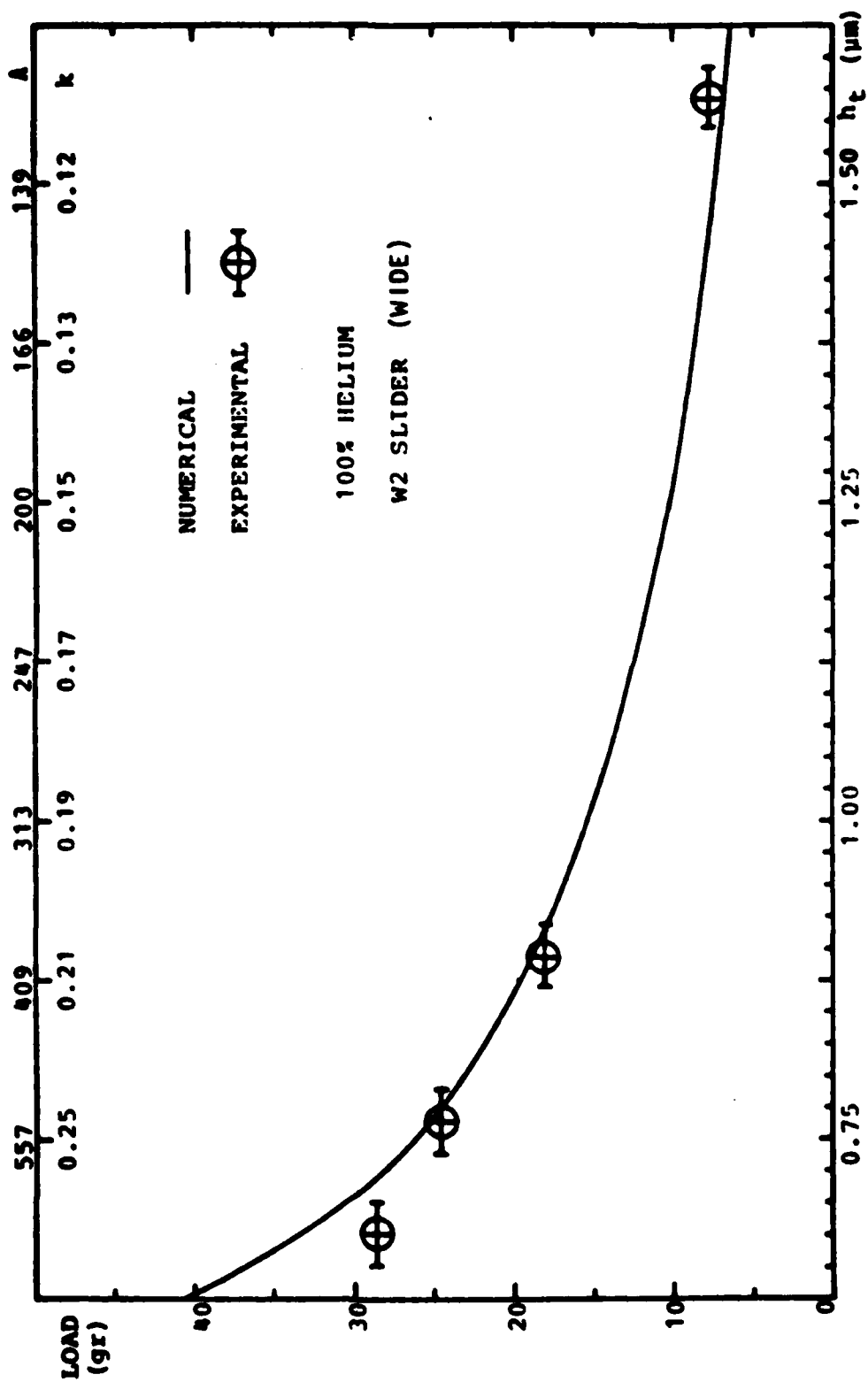
FIGURE 11-59: LOAD VS TRAILING EDGE CLEARANCE, U = 50.81 m/sec
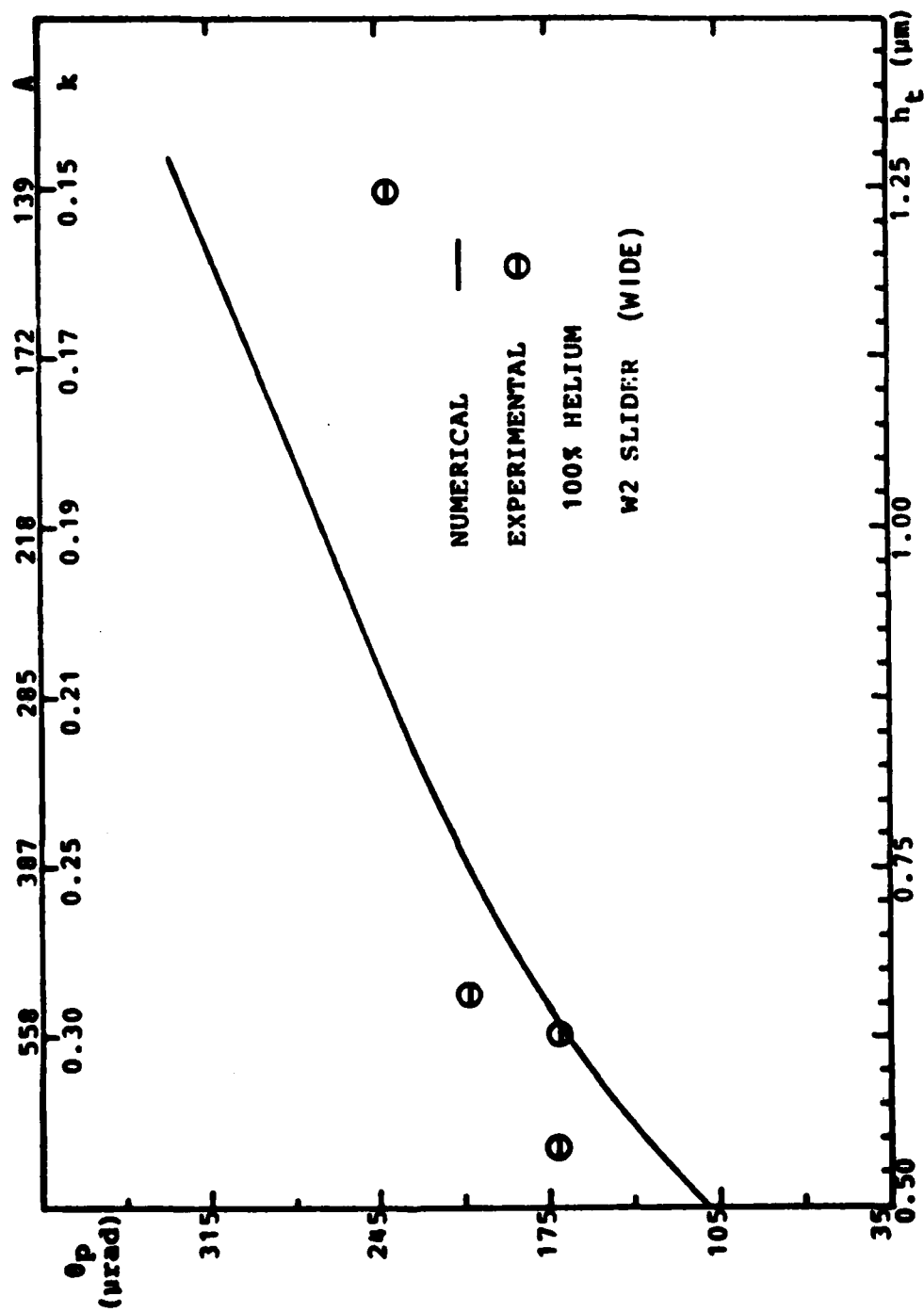
FIGURE 11-60: PITCH ANGLE VS TRAILING EDGE CLEARANCE, U = 35.35 m/sec

NUMERICAL

EXPERIMENTAL

100% HELIUM

W2 SLIDER (WIDE)
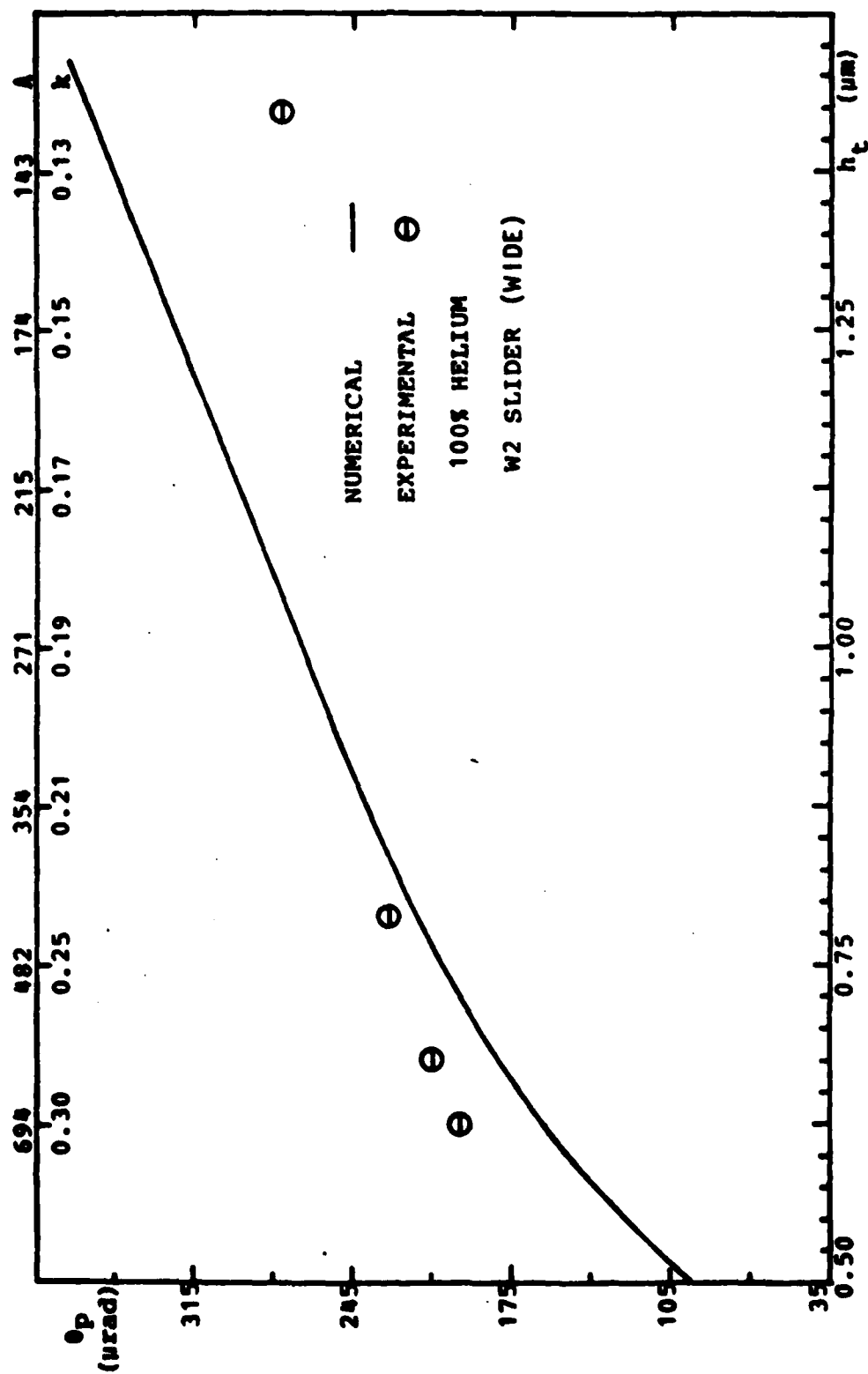
FIGURE 11-61: PITCH ANGLE VS TRAILING EDGE CLEARANCE, U = 44.01 m/sec
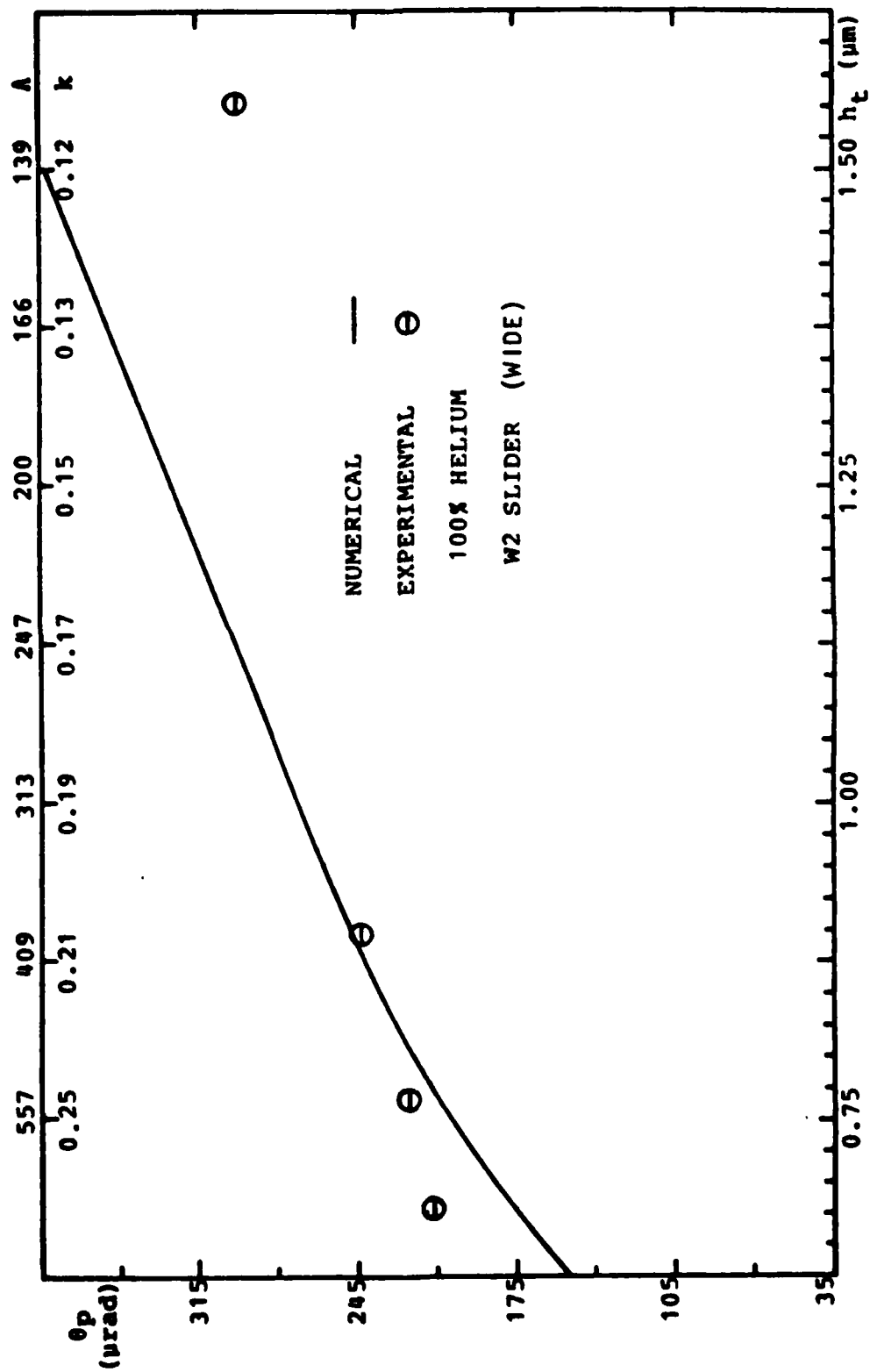
FIGURE 11-62:   PITCH ANGLE VS TRAILING EDGE CLEARANCE, U = 50.81 m/sec
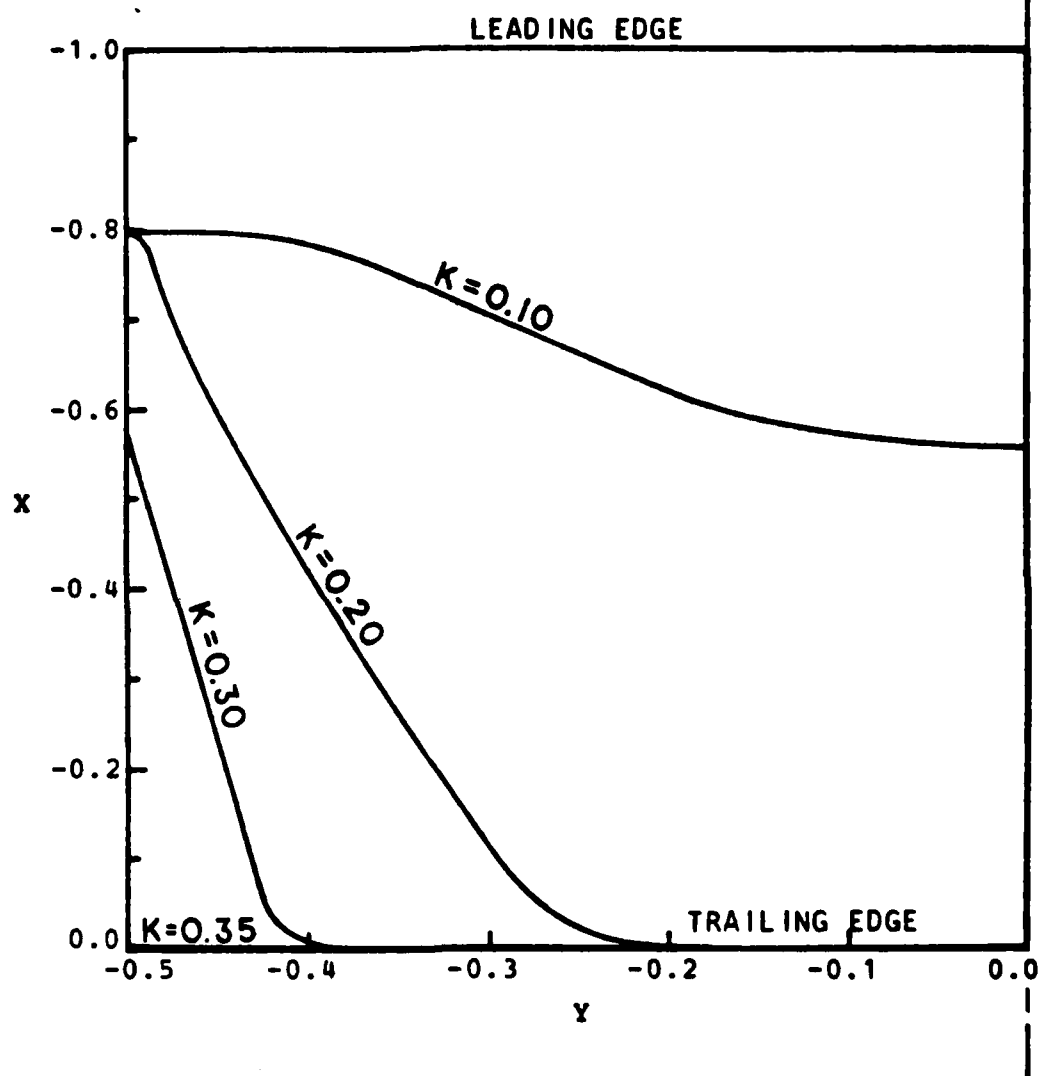
FIGURE 11-63 : CONTOUR PLOT OF LOCAL KNUDSEN NUMBER UNDER A SLIDER PAD (PX3 SLIDER at h_t = 0.1905 μm, Λ = 6091, K_∞ = 0.35)
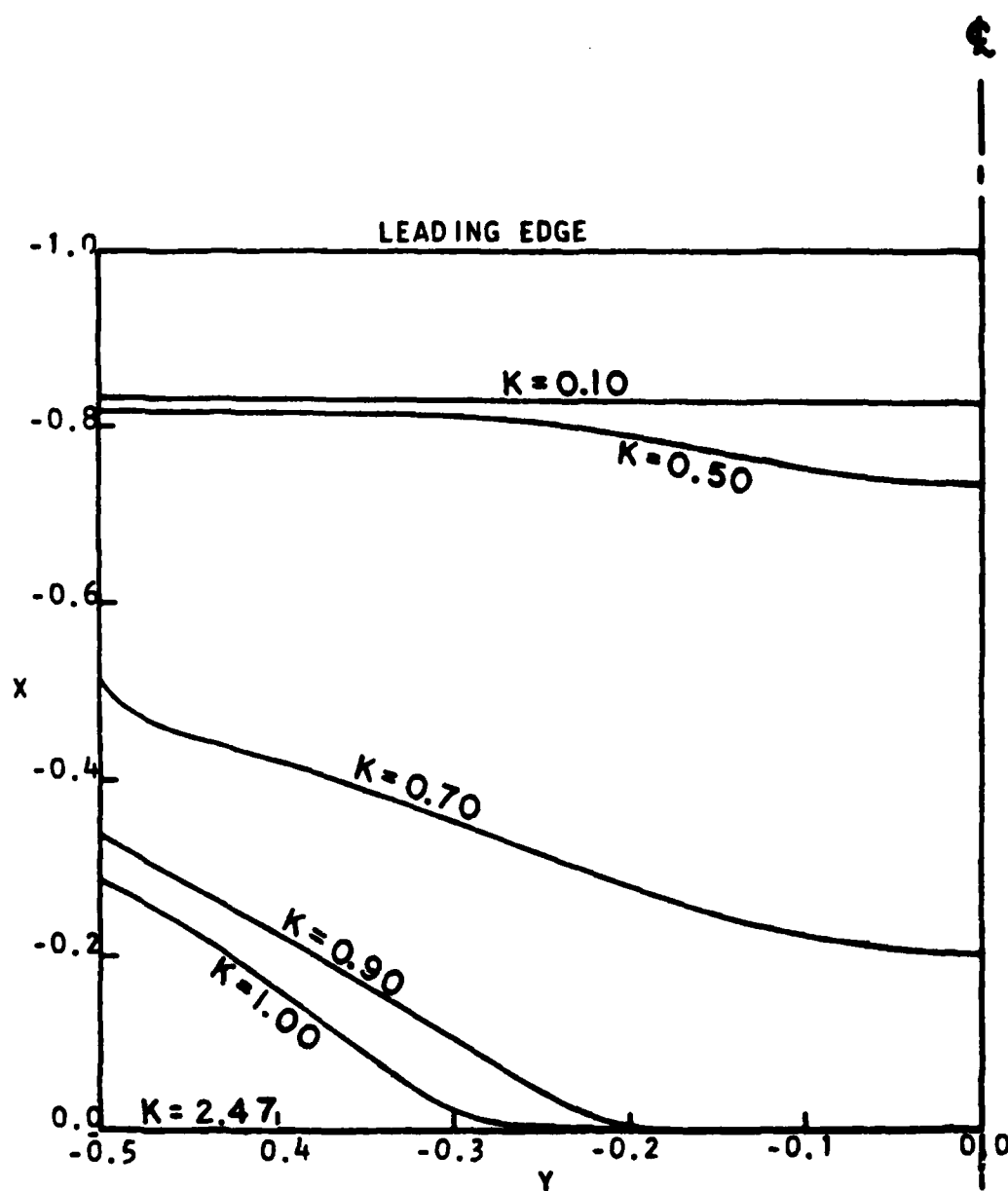
FIGURE 11-64: CONTOUR PLOT OF LOCAL KNUDSEN NUMBER UNDER A SLIDER PAD (Y2 SLIDER at h_t = 0.075 um, Λ = 19308, K_∞ = 2.47)

PA3 SLIDER: (SHOE A)   AIR
(NARROW)

h_t = 0.1905 μm

θ_p = 38.92 μrad

Λ = 6091

K = 0.35

X=-0.7944;H=1.909 (BREAK)

X=-0.0090;H=1.005
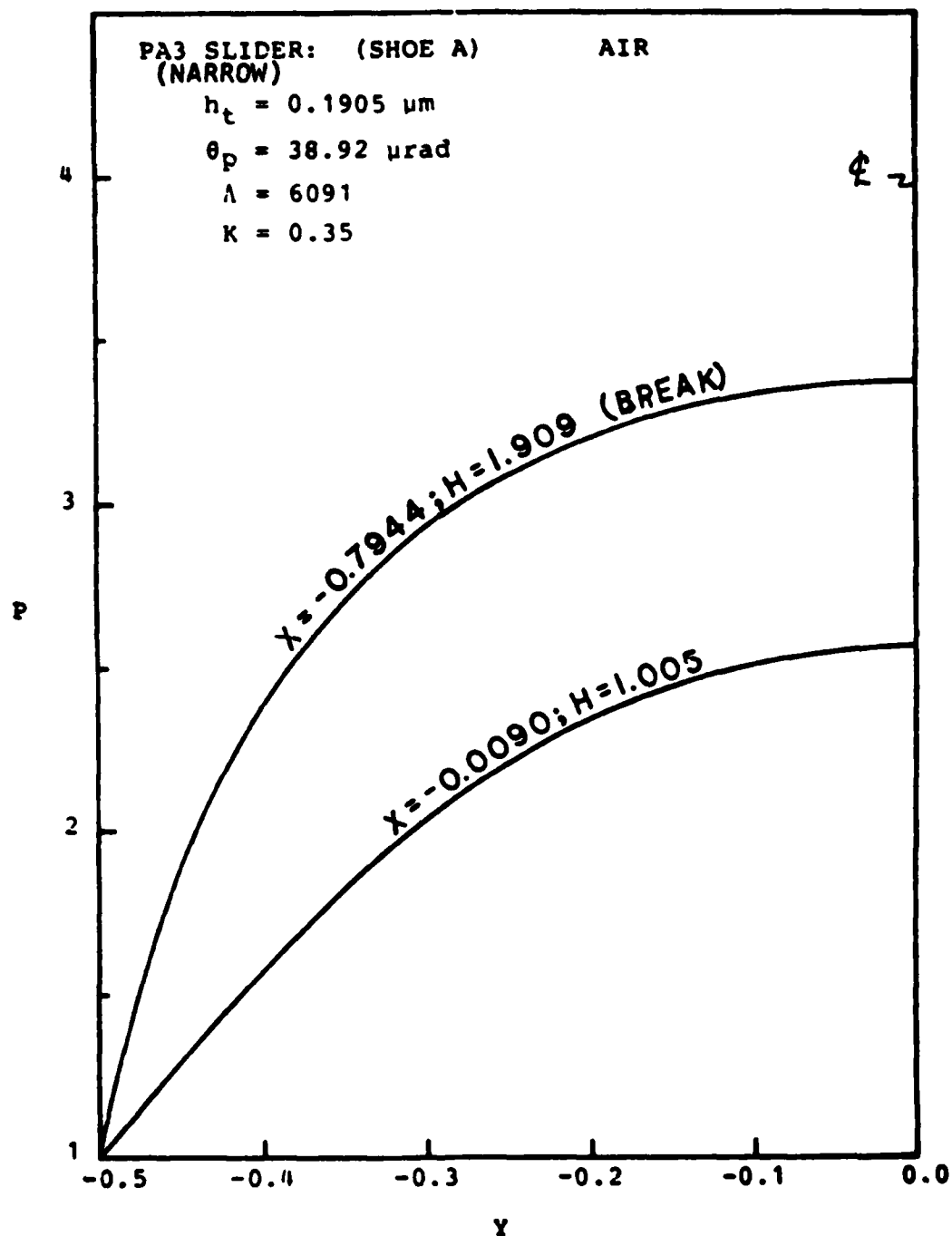
FIGURE 11-65   PRESSURE ACROSS THE BEARING, AT
THE BREAK AND NEAR THE TRAILING
EDGE.
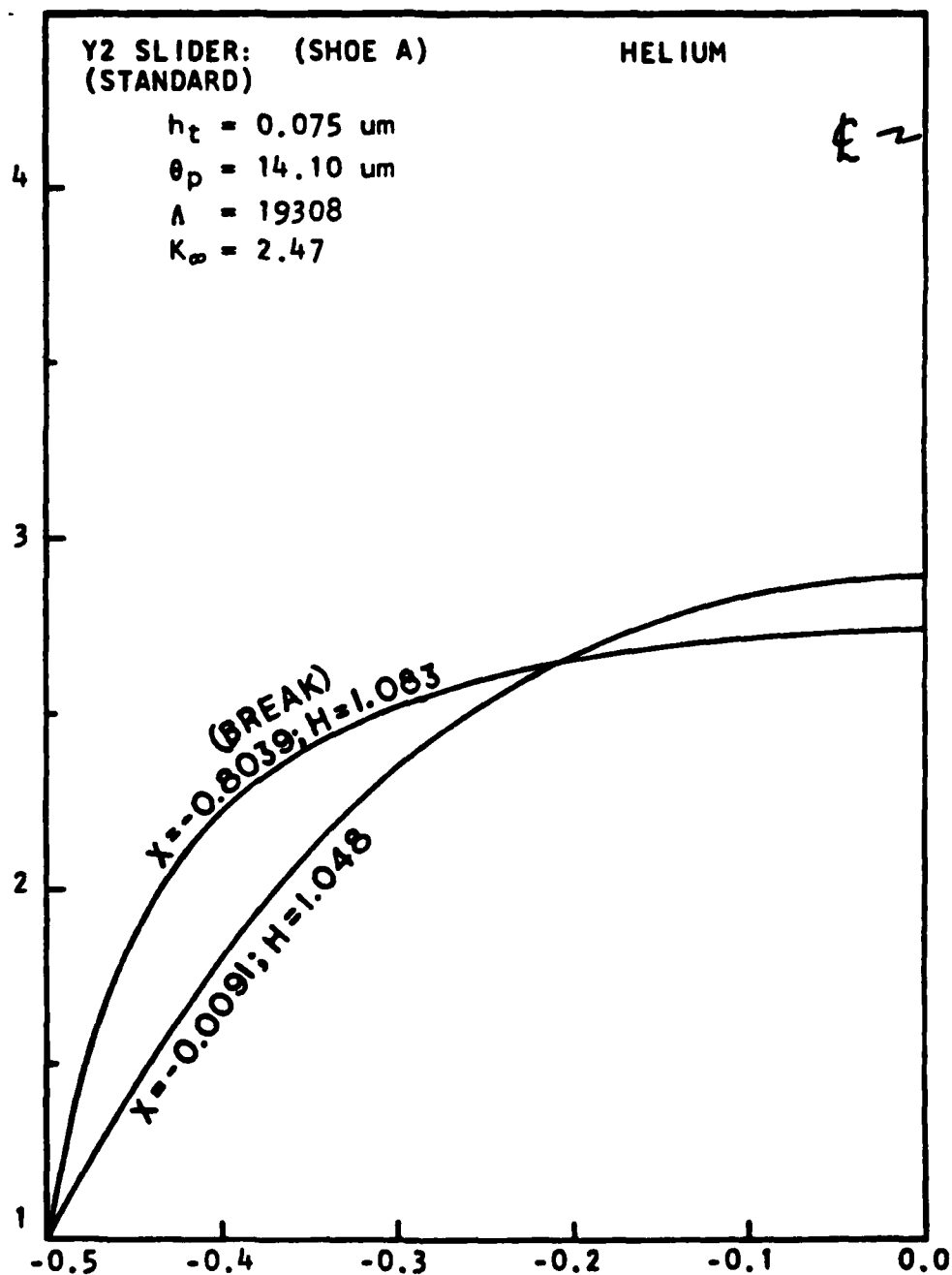
FIGURE 11-66: PRESSURE ACROSS THE BEARING, AT THE BREAK AND NEAR THE TRAILING EDGE

116

TEST CASE: R2 Slider with h_t = 0.438 μm. Solve for the load and pitch angle for a known pivot point of 2.54 mm from trailing edge.

NUMERICAL ALGORITHM	LOAD (gr)	PITCH (μrad)	EXECUTION CPU (sec)
INTEGRAL DISCRETIZATION VARIABLE GRID (50 × 21)	12.56	124.36	68.23
EXPONENTIAL APPROXIMATION VARIABLE GRID (50 × 21)	12.48	126.15	25.08
EXPONENTIAL APPROXIMATION CONSTANT GRID (45 × 21)	12.25	132.64	21.67
EXPONENTIAL APPROXIMATION CONSTANT GRID (34 × 21)	12.22	135.81	17.44

FIGURE 11-67: COMPARISON OF NUMERICAL ALGORITHMS

REFERENCES

1. Bird,G.A. Molecular Gas Dynamics. Claredon Press, 1976.

2. Booker, J.F. and Huebner, K.H. Application of Finite Element Methods to Lubrication: An Engineering Approach. Journal of Lubrication Technology, Transactions of the ASME. 94, 4 (October 1972), 313-323.

3. Briggs, G.R. and Herkart, P.G. Unshielded Capacitor Probe Technique for Determining Disk Memory Ceramic Slider Flying Characteristics. I.E.E.E. Trans. on Magnetics 45 (september 1971), 68-73.

4. Brunner, R.K., Harker, J.M., et.al. A Gas Film Lubrication Study, Part III: Experimental Investigation of Pivoted Slider Bearings. IBM Journal of Research and Development. 8 (July 1959), 260-274.

5. Burgdorfer, A. The Influence of the Molecular Mean Free Path on the Performance of Hydrodynamic Gas Lubricated Bearings. Journal of Basic Engineering, Transactions of the ASME. 81, 3 (March 1959), 94-100.

6. Castelli, V. and Pirvics, J. Review of Numerical Methods in Gas Bearing Film Analysis. Journal of Lubrication Technology, Transactions of the ASME. 90, 4 (October 1968), 777-792.

7. Christensen, H. and Tonder, K. The Hydrodynamic Lubrication of Rough Bearing Surfaces of Finite Width. Journal of Lubrication Technology, Transactions of the ASME. 93, 3 (July 1971), 324-330.

8. Coleman, R.L. A Brief Comparison of the Accuracy of Time Dependent Integration Schemes for the Reynolds Equation. Journal of Lubrication Technology, Transactions of the ASME. 94, 4 (October 1972), 330-334.

9. Constantinescu,V.N. Gas Lubrication. The American Society of Mechanical Engineers, 1969.

10. DiPrima, R.C. Asymptotic Methods for an Infinitely Long Slider Squeeze Film Bearing. Journal of Lubrication Technology, Transactions of the ASME. 190, 1 (January 1968), 173-183.

11. DiPrima, R.C. Higher Order Approximations in the Asymptotic Solution of the Reynolds Equation for Slider Bearings at High Bearing Numbers. Journal of Lubrication Technology, Transactions of the ASME. 91, 1 (January 1969), 45-51.

12. Elrod, H.G. Private Discussions on Numerical Solution Techniques For Solving the Modified Reynolds Equation. Private Communications

13. Elrod, H.G. and McCabe, J.T. Theory for Finite-Width High-Speed Self-Acting Gas Lubricated Slider (and Partial Arc) Bearings. Journal of Lubrication Technology, Transactions of the ASME. 91, 1 (January 1969), 17-24.

14. Elrod, H.G. Lubrication Theory for Newtonian Fluids With Striated Roughness or Grooving. 21, Lubrication Laboratory - Columbia University, 1972.

15. Fuller,D.D. Theory and Practice of Lubrication for Engineers. John Wiley and Sons, Inc., 1956.

16. Gross,W.A. Gas Film Lubrication. John Wiley and Sons, Inc., 1962.

17. Gross, W.A. and Zachmanoglou, E.C. Perturbation Solutions for Gas Lubricating Films. Journal of Basic Engineering, Transaction of ASME. 83, 3 (June 1961), 139-144.

18. Harper, J., Levenglick, P., and Wilczynski, J. An Interferometric Method of Determining the Separation Between Two Moving Surfaces. I.B.M. Research Report. RC-1189, May, 1964.

19. Hoagland, A.S. Digital Magnetic Recording. John Wiley and Sons, Inc., 1963.

20. Hsing, F.C. and Malanoski, S.B. Mean Free Path Effect in Spiral Grooved Thrust Bearings. Journal of Lubrication Technology, Transactions of the ASME. 91, 1 (January 1969), 69-78.

21. Kogure, K., Kaneko, R., and Mitsuya, Y. Static Characterisitcs of Gas Lubricated Slider Bearings under Submicron Spacing Conditions. Private Communications

22. Lin, C., and Sullivan, R.F. An Application of White Light Interferometry in Thin Film Measurements. IBM Journal of Research and Development. 19 (May 1972), 269-278.

23. Lipschutz, L.D. Dynamic Measurement of Small Separations by a Light Interference Method. Proceedings of the International Conference on Magnetic Recording, Institute of Electronic Engineer, July, 1964.

24. Pear, C.B. Magnetic Recording in Science and Industry. Reinhold Publishing Corporation, 1967.

25. Reddi, M.M. Finite Element Solution of the Incompressible Lubrication Problem. Journal of Lubrication Technology, Transactions of the ASME. 91, 3 (July 1969), 524-533.

26. Reddi, M.M. and Chu, T.T. Finite Element Solution of the Steady-State Compressible Lubrication Problem. Journal of Lubrication Technology, Transactions of the ASME. 92, 3 (July 1970), 495-503.

27. Rhow, S.K. and Elrod, H.G. The Effects on Bearing Load-Carrying Capacity of Two-Sided Striated Roughness. Journal of Lubrication Technology, Transactions of the ASME. 96, 4 (October 1974), 554-560.

28. Roache, P.J. Computational Fluid Dyanmics. Hermosa Publishers, 1972.

29.   Rohsenow, W.M. and Hartnett, J.P. Handbook of Heat Transfer. McGraw-Hill Book Company, 1973.

30.   Schaaf, S.A. and Sherman, F.S. Skin Friction in Slip Flow. Journal of Aeronautical Sciences 21, 2 (1953), 85-90.

31.   Schmitt, J.A. and DiPrima, R.C. Asymptotic Methods for an Infinite Slider Bearing With a Discontinuity in Film Slope. Journal of Lubrication Technology, Transactions of the ASME. 98, 3 (July 1976), 446-452.

32.   Schmitt, J.A. and DiPrima, R.C. Asymptotic Methods for a General Finite Width Gas Slider Bearing. Journal of Lubrication Technology, Transactions of the ASME. 100, 2 (April 1978), 254-260'.

33.   Sereny, A. Experimental Investigation of Gas Bearings with Ultra-Thin Films. Ph.D. Th., Columbia University, June 1977.

34.   Sun, D.C. and Chen, K.K. First Effects of Stokes Roughness on Hydrodynamic Lubrication. Journal of Lubrication Technology, Transactions of the ASME. 99, 1 (Jan 1977), 2-9.

35.   Tseng, R.C. Rarefaction Effects of Gas-Lubricated Bearings in a Magnetic Recording Disk File. Journal of Lubrication Technology, Transactions of the ASME. 97, 4 (October 1975), 624-629.

36.   Tzeng, S.T. and Saibel, E. Surface Roughness Effect on Slider Bearing Lubrication. A.S.L.E., Trans. 10 (1967), 334-338.

37.   White, J.W. and Nigram, A. A Factored Implicit Scheme for the Numberical Solution of the Reynolds Equation at Very Low Spacings. Journal of Lubrication Technology, Transactions of the ASME. 102, 1 (January 1980), 80-85.

APPENDIX A

DERIVATION OF THE MODIFIED REYNOLDS EQUATION

The modified Reynolds equation as given by equation (3.3) is derived in this appendix. The equation was first developed by Burgdorfer [5]. In this investigation, the equation is slightly different from Burgdorfer's to give a better insight into the effect of side leakage. The equation below are written with reference to the cartesian coordinate system defined in Figure 11-2.

The appropriate Navier-Stokes equations and continuity equation for the gas bearing problem are:

Momentum:

$$\frac{\partial p}{\partial x} = \mu \frac{\partial^2 u}{\partial z^2} \qquad (11.1)$$

$$\frac{\partial p}{\partial y} = \mu \frac{\partial^2 v}{\partial z^2} \qquad (11.2)$$

$$\frac{\partial p}{\partial z} = 0 \qquad (11.3)$$

Continuity:

$$\frac{\partial}{\partial x}\left[\rho \int_0^h u\, dz\right] + \frac{\partial}{\partial y}\left[\rho \int_0^h v\, dz\right] = 0 \qquad (11.4)$$

The boundary conditions are:

$$u\,(z{=}0) = U + \lambda \left.\frac{\partial u}{\partial z}\right|_{z=0} \qquad (11.5)$$

$$u \ (z{=}h) \ = \ -\lambda \ \frac{\partial u}{\partial z}\bigg|_{z=h} \qquad (11.6)$$

$$v \ (z{=}0) \ = \ \lambda \ \frac{\partial v}{\partial z}\bigg|_{z=0} \qquad (11.7)$$

$$v \ (z{=}h) \ = \ -\lambda \ \frac{\partial v}{\partial z}\bigg|_{z=h} \qquad (11.8)$$

From equation (11.3), it follows that the pressure p is independent of z. Integrating equation (11.1) twice with respect to z and using the boundary conditions (11.5) and (11.6) gives:

$$u = -\frac{1}{2\mu} \ \frac{\partial p}{\partial x}\Big[h\lambda + hz - z^2\Big] + U\Big[1 - \frac{z + \lambda}{h + 2\lambda}\Big] \qquad (11.9)$$

Similarly, solving equation (11.2) with boundary condition (11.7) and (11.8) gives:

$$v = -\frac{1}{2\mu} \ \frac{\partial p}{\partial y}\Big[h\lambda + hz - z^2\Big] \qquad (11.10)$$

Substituting equations (11.9) and (11.10) into equation (11.4) gives:

$$\frac{\partial}{\partial x}\Big[\rho \frac{h^3}{12\mu} \frac{\partial p}{\partial x}(1 + \frac{6\lambda}{h})\Big] + \frac{\partial}{\partial y}\Big[\rho \frac{h^3}{12\mu} \frac{\partial p}{\partial y}(1 + \frac{6\lambda}{h})\Big] = \frac{\partial}{\partial x}\Big[\frac{\rho U h}{2}\Big] \qquad (11.11)$$

Because the viscosity is nearly independent of pressure in the range considered and since the temperature variations across the gas film are small, the viscosity can be assumed to be constant. Moreover, an isothermal relationship can be assumed, i.e.

$$\frac{p}{p_a} = \frac{\rho}{\rho_a} \qquad (11.12)$$

With the above assumptions, equation (11.11) becomes:

$$\frac{\partial}{\partial x}\left[ph^3\frac{\partial p}{\partial x}\left(1 + \frac{6\lambda}{h}\right)\right] + \frac{\partial}{\partial y}\left[ph^3\frac{\partial p}{\partial y}\left(1 + \frac{6\lambda}{h}\right)\right] = 6\mu U\left[\frac{\partial}{\partial x}(ph)\right]$$

(11.13)

Equations (11.11) and (11.13) are modified forms Reynolds equation for the slip flow region $(0 < \lambda/h < 1)$. The boundary condition on equation (11.11) or (11.13) is:

$$p(x,y) = p_a \qquad \text{on all boundaries} \qquad (11.14)$$

To write equation (11.13) in dimensionless form, define the following:

$$P = p/p_a \qquad (11.15)$$

$$X = x/l \qquad (11.16)$$

$$Y = y/w \qquad (11.17)$$

$$H = h/h_{min} \qquad (11.18)$$

For constant temperature,

$$\frac{\lambda}{\lambda_a} = \frac{p_a}{p} \qquad (11.19)$$

With equations (11.15) to (11.19), equation (11.13) becomes:

$$\left(\frac{w}{l}\right)^2\frac{\partial}{\partial X}\left[PH^3\frac{\partial P}{\partial X}\left(1 + \frac{6K_\infty}{PH}\right)\right] + \frac{\partial}{\partial Y}\left[PH^3\frac{\partial P}{\partial Y}\left(1 + \frac{6K_\infty}{PH}\right)\right] = \Lambda\left(\frac{w}{l}\right)^2\frac{\partial}{\partial X}(PH)$$

(11.20)

where

$$\Lambda = \frac{6\mu U l}{p_a h_{min}^2} \qquad (11.21)$$

$$K_\infty = \frac{\lambda_a}{h_{min}}$$ (11.22)

In equation (11.20), the slider width to length ratio appears as the result of the non-dimensionalization process. With this ratio present, the effect of side leakage is more evident. As the equation clearly shows, the side flow term (i.e. the Y-derivative term) may not be neglected if the width to length ratio is small since the other terms in the equation are multiplied by the factor $(w/l)^2$. Typically, the (w/l) ratio for the present narrow bearing is about 0.1.

Equation (11.20) can be written in the following form:

$$\left(\frac{w}{l}\right)^2 \frac{\partial}{\partial X}\left[PH^3\frac{\partial P}{\partial X}(1 + \frac{6K_\infty}{PH})\right] + \frac{\partial}{\partial Y}\left[PH^3\frac{\partial P}{\partial Y}(1 + \frac{6K_\infty}{PH})\right] = \Lambda^* \frac{\partial(PH)}{\partial X}$$ (11.23)

where the Modified Bearing Number is define as -

$$\Lambda^* = \Lambda\left(\frac{w}{l}\right)^2$$ (11.24)

APPENDIX B

EXPONENTIAL APPROXIMATION OF REYNOLDS EQUATION

In this appendix, the exponential approximation of the Modified Reynolds equation is outlined. This technique was originally developed by H.G. Elrod [12]. The author is very grateful to Professor Elrod for sharing this algorithm.

The steady-state modified Reynolds equation can often be written in terms of the mass fluxes:

$$\frac{\partial}{\partial X}(\dot{m}_x) + \frac{\partial}{\partial Y}(\dot{m}_y) = 0 \tag{11.25}$$

where

$$\dot{m}_x = - PH^3(1 + \frac{6K_\infty}{PH})\frac{\partial P}{\partial X} + \Lambda_x HP \tag{11.26}$$

$$\dot{m}_y = - PH^3(1 + \frac{6K_\infty}{PH})\frac{\partial P}{\partial Y} + \Lambda_y HP \tag{11.27}$$

with the variables nondimensionalized as follows:

$$X = \frac{x}{T} \quad ; \quad Y = \frac{y}{T} \quad ; \quad P = \frac{p}{P_a} \quad ; \quad H = \frac{h}{h_{min}}$$

Now consider the mass flux in the X direction as given by equation (11.26), which is is a non-linear first order differential equation in P. Assuming this mass flux ($\dot{m}_x$) is constant between two points, say X_i and X_{i+1}, and

also assuming the coefficients in equation (11.26) are constant with some average value between the two points, Equation (11.26) can be rewritten as:

$$\dot{m}_x = - C_1 \frac{\partial P}{\partial X} + C_2 \qquad (11.28)$$

where

$$C_1 = \overline{PH^3 \left(1 + \frac{6K_\infty}{PH}\right)} \qquad (11.29)$$

$$C_2 = \overline{\Lambda_x H} \qquad (11.30)$$

(The bar denotes some averaged value between X_i and X_{i+1})

The boundary condition on equation (11.26) is:

$$P = P_i \qquad \text{at } X = X_i \qquad (11.31)$$

The solution for equation (11.26) with the above boundary condition (11.31) is:

$$P = \frac{\dot{m}_x}{C_2}\left[1 - e^{\left(\frac{C_2}{C_1}\right)(X - X_i)}\right] + P_i \, e^{\left(\frac{C_2}{C_1}\right)(X - X_i)} \qquad (11.32)$$

or solving for $\dot{m}_x$, equation (11.32) becomes -

$$\dot{m}_x = \frac{C_2(P_i - P)}{\left[e^{\left(\frac{C_2}{C_1}\right)(X - X_i)} - 1\right]} + C_2 P_i \qquad (11.33)$$

Therefore, the mass flux between X_i and X_{i+1} is given by:

$$\dot{m}_x = \frac{C_2(P_i - P_{i+1})}{\left[e^{\left(\frac{C_2}{C_1}\right)(X_{i+1}-X_i)} - 1\right]} + C_2 P_i \qquad (11.34)$$

where C_1 and C_2 are given by equations (11.29) and (11.30), respectively.

Similar expression can be obtained for the mass flux in the Y direction, i.e. between Y_j and Y_{j+1}:

$$\dot{m}_y = \frac{C_4(P_j - P_{j+1})}{\left[e^{\left(\frac{C_4}{C_3}\right)(Y_{j+1}-Y_j)} - 1\right]} + C_4 P_j \qquad (11.35)$$

where

$$C_3 = \overline{PH^3\left(1 + \frac{6K_\infty}{PH}\right)} \qquad (11.36)$$

$$C_4 = \overline{\Lambda_y H} \qquad (11.37)$$

(The bar denotes some average value between Y_j and Y_{j+1})

With $\dot{m}_x$ and $\dot{m}_y$ known, standard finite difference approximation can be applied to equation (11.25) for each grid point and the problem can thus be solved with either Column Method or Alternating Directional Implicit (ADI) scheme or Alternating Directional Successive Line Relaxation scheme.

APPENDIX C

DATA REDUCTION PROCEDURE

In this study, the bearing clearance profile for each experiment is determined by fitting the experimental data with an assumed surface profile using the method of least squares. The experimental data is in the form of interference fringes as shown in Figure 11-13. Before the fitting process can begin, the dark fringes on each slider shoe from the the two lasers are located and their order identified. To identify the order of the fringes appearing on the shoe, the location of the fringes from the Helium-Neon laser is plotted as shown in Figure 11-14 by assuming their orders are known. Once this is done, the fringes from the Helium-Cadmium laser is also plotted on the same figure. If the resulting superposition of the two sets of fringes does not make any sense, the process is repeated until the fringes establish a meaningful surface contour as shown by Figure 11-14. Once this is accomplished, the order of the "red" and "blue" fringes are determined.

As shown in Figure 11-14, in order to determine the flying profile of the shoe, that is, the trailing edge clearance and the pitch angle, a "parabolic" surface profile (crown) is fitted to the data points on the shoe. For example, in the figure, a 0.051 μm crown seems to give a good fit for shoe B of the PA3 slider. Similar procedure is followed for determining the profile for shoe

A of the same slider. Because the two shoes of the slider are physically connected to each other, their relative positions with each other must be maintained when fitting the data. This criterion cannot not be satisfied when fitting by hand and a large error can result in determining the flying characteristics of the slider.

This potential error in fitting can be significantly reduced with the use of the Method of Least Squares because the flying profile determined using this fitting technique is mathematically the best that can be obtained for the available data.

The equation of the curve that is to be fitted through the data points is given by the following expression: (refer to Figure 11-2 for notations)

$$h^f = h_t + h_{s1} + \theta_r y - \theta_p x \tag{11.38}$$

where
h^f = fitted clearance

h_t = average trailing edge clearance

θ_r = roll angle

θ_p = pitch angle

(x,y) = location of fringe on the shoe

and h_{s1} is the surface profile given by –

$$h_{s1} = h_c\left[\left(\frac{2x}{(1-l_r)} + 1\right)^2 - 1\right] \tag{11.39}$$

Therefore, for each fringe k, the location and the order of the fringe is known and the fitted clearance is

given by -

$$h_k^f = h_t + h_{s1_k} + \theta_r y_k - \theta_p x_k \qquad (11.40)$$

Furthermore, at the k<u>th</u> fringe, the actual clearance is also known and is given by:

$$h_k^a = (n-1)\frac{\lambda}{2} \qquad n = 1,2,3,\ldots \qquad (11.41)$$

where   n = order of the fringe

   λ = wavelength of laser

   h_k = actual clearance at k<u>th</u> fringe

For each data point in the experiment, there is a h_k^f and a h_k^a associated with it. Because there is error between the fitted clearance and the actual clearance at each fringe, it is desired that the parameters h_t, θ_p, θ_r be determined such that the sum of the squares of these errors be minimized. Mathematically, the problem can be stated as follows:

Let the sum of the squares of the errors be given by the following expression:

$$E = \sum_{k=1}^{m} (h_k^a - h_k^f)^2 \qquad m = \text{no. of data pts.} \quad (11.42)$$

and to minimize the error, E, with respect to the parameters h_t, θ_p, and θ_r means:

$$\frac{\partial E}{\partial h_t} = \frac{\partial E}{\partial \theta_r} = \frac{\partial E}{\partial \theta_p} = 0 \qquad (11.43)$$

Substituting equations (11.40) and (11.41) into equation (11.42) and carrying out the differentiation as prescribed

by equation (11.43), a system of three equations with three unknowns (h_t, θ_p, θ_r) results:

$$
\begin{bmatrix}
m & \sum\limits_{k=1}^{m} y_k & \sum\limits_{k=1}^{m} x_k \\[2em]
\sum\limits_{k=1}^{m} y_k & \sum\limits_{k=1}^{m} y_k^2 & -\sum\limits_{k=1}^{m} x_k y_k \\[2em]
-\sum\limits_{k=1}^{m} x_k & -\sum\limits_{k=1}^{m} x_k y_k & \sum\limits_{k=1}^{m} x_k^2
\end{bmatrix}
\begin{bmatrix}
h_t \\[2em] \theta_r \\[2em] \theta_p
\end{bmatrix}
=
\begin{bmatrix}
\sum\limits_{k=1}^{m}(h_k - h_{sl_k}) \\[2em]
\sum\limits_{k=1}^{m}(h_k - h_{sl_k}) y_k \\[2em]
\sum\limits_{k=1}^{m}(h_k^a - h_{sl_k}) x_k
\end{bmatrix}
\quad (11.44)
$$

The only free parameter appearing in the above equation is the crown height, h_c, which is in h_{sl}. Once the crown height is specified, the above system of equations (11.44) can be solved for h_t, θ_p, and θ_r. To examine how well the assumed curve fitted the data, the error given by equation (11.42) is calculated. Therefore, to determine the best crown on each shoe, different combinations of crown on each shoe are tried and the combination that gives the least error in fitting is designated as the crowns on the two shoes. Moreover, the h_t, θ_p, and θ_r values calculated from equation (11.44) for the best crown combination are also designated as the flying profile of the slider.

APPENDIX D

ALTERNATING DIRECTIONAL IMPLICIT
AND
SUCCESSIVE LINE RELAXATION SCHEMES

This appendix gives an outline of the Alternating Directional Implicit (ADI) scheme and the Alternating Directional Successive Line Relaxation (ADSLR) scheme used to solve the system of equations resulting from discretizing the Reynolds equation. To discretize the equation, the finite difference approximation can be applied directly to the Reynolds equation given by equation (11.25). It is recognized that equation (11.25) is a mass balance equation. Thus to discretize the equation, a mass balance is performed at each grid point.

Consider the variable grid mesh as shown below and let the arrows denote the directions of mass flow into and out of the grid cell about node (i,j) –
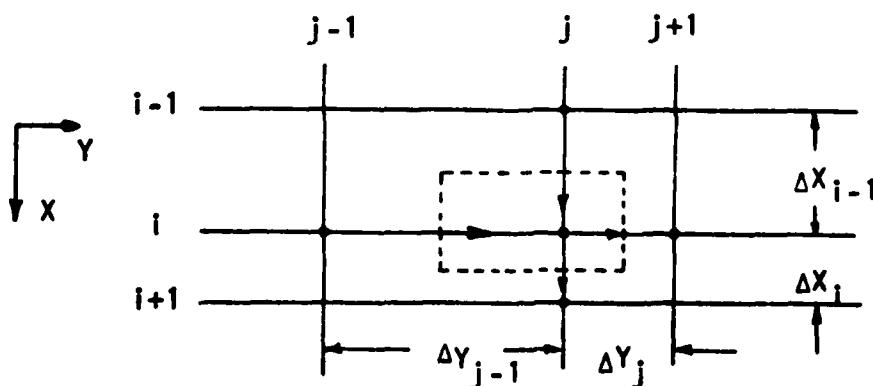
The mass balance at node (i,j) is simply stated as

follows:

$$\text{(mass in)} - \text{(mass out)} = \text{mass accumulated}$$

where the mass fluxes in the x and y directions are given by equations (11.34) and (11.35), respectively.

Consider the mass in and out of node (i,j) in the x direction:

The mass flux into the node is given by:

$$(\dot{m}_x)_{in} = \frac{C_2(P_{i-1,j} - P_{ij})}{\left[e^{(\frac{C_2}{C_1})(X_i - X_{i-1})} - 1 \right]} + C_2 P_{i-1,j} \tag{11.45}$$

while the mass flux out of the node is given by:

$$(\dot{m}_x)_{out} = \frac{C_2(P_{i,j} - P_{i+1,j})}{\left[e^{(\frac{C_2}{C_1})(X_{i+1} - X_i)} - 1 \right]} + C_2 P_{i,j} \tag{11.46}$$

Thus the mass balance in the X direction can be written as follows:

$$\left[A^- P_{i-1,j} - A^- P_{ij} + C_2^- P_{i-1,j} - A^+ P_{ij} + A^+ P_{i+1,j} - C_2^+ P_{ij} \right] \overline{\Delta Y}$$

with $\overline{\Delta Y} = \frac{1}{2}(\Delta Y_{j-1} + \Delta Y_j)$ \qquad (11.47)

where

133

$$A = -\frac{-C_2(\Delta P)}{\left[e^{(\frac{C_2}{C_1})(\Delta X)} - 1\right]} \qquad (11.48)$$

with superscripts $^-$ and $^+$ denoting
some averaged values between X_{i-1} and X_i,
and X_i and X_{i+1}, respectively.

Similarly the mass balance in the Y direction is given as follows:

$$\left[B^- P_{i,j-1} - B^- P_{ij} + C_4^- P_{i,j-1} - B^+ P_{ij} + B^+ P_{i,j+1} - C_4^+ P_{ij}\right]\overline{\Delta X}$$

with $\quad \Delta X = \frac{1}{2}(\Delta X_{i-1} + \Delta X_i)$ $\qquad (11.49)$

where

$$B = \frac{-C_4(\Delta P)}{\left[e^{(\frac{C_4}{C_3})(\Delta Y)} - 1\right]} \qquad (11.50)$$

with superscripts $^-$ and $^+$ denoting
some averaged values between Y_{j-1} and Y_j,
and Y_j and Y_{j+1}, respectively.

The mass accumulated at (i,j) is given by:

$$H_{ij}\overline{\Delta X \Delta Y}\frac{(P_{i,j}^{n+1} - P_{i,j}^{n})}{\Delta T} \qquad (11.51)$$

Thus, the discretized form of the Reynolds equation becomes:

$$\left[A^-P_{i-1,j} - A^-P_{ij} + C_2^-P_{i-1,j} - A^+P_{ij} + A^+P_{i+1,j} - C_2^+P_{ij}\right]\overline{\Delta Y}$$

$$+ \left[B^-P_{i,j-1} - B^-P_{ij} + C_4^-P_{i,j-1} - B^+P_{ij} + B^+P_{i,j+1} - C_4^+P_{ij}\right]\overline{\Delta X}$$

$$= H_{ij}\overline{\Delta X}\,\overline{\Delta Y}\frac{(P_{ij}^{n+1} - P_{ij}^{n})}{\Delta T} \tag{11.52}$$

In this study, the Peaceman-Rachford ADI method is employed. The advancement of the equation over ΔT is accomplished in two steps (two half-time steps) -

1st Step:

$$\left[A^-P_{i-1,j}^{n} - A^-P_{ij}^{n} + C_2^-P_{i-1,j}^{n} - A^+P_{ij}^{n} + A^+P_{i+1,j}^{n} - C_2^+P_{ij}^{n}\right]\overline{\Delta Y}$$

$$+ \left[B^-P_{i,j-1}^{n+\frac{1}{2}} - B^-P_{ij}^{n+\frac{1}{2}} + C_4^-P_{i,j-1}^{n+\frac{1}{2}} - B^+P_{ij}^{n+\frac{1}{2}} + B^+P_{i,j+1}^{n+\frac{1}{2}} - C_4^+P_{ij}^{n+\frac{1}{2}}\right]\overline{\Delta X}$$

$$= H_{ij}\overline{\Delta X}\,\overline{\Delta Y}\frac{(P_{ij}^{n+\frac{1}{2}} - P_{ij}^{n})}{\Delta T} \tag{11.53}$$

2nd Step:

$$\left[A^-P_{i-1,j}^{n+1} - A^-P_{ij}^{n+1} + C_2^-P_{i-1,j}^{n+1} - A^-P_{ij}^{n+1} + A^-P_{i+1,j}^{n+1} - C_2^-P_{ij}^{n+1}\right]\overline{\Delta Y}$$

$$+ \left[B^-P_{i,j-1}^{n+\frac{1}{2}} - B^-P_{ij}^{n+\frac{1}{2}} + C_4^-P_{i,j-1}^{n+\frac{1}{2}} - B^+P_{ij}^{n+\frac{1}{2}} + B^+P_{i,j+1}^{n+\frac{1}{2}} - C_4^+P_{ij}^{n+\frac{1}{2}}\right]\overline{\Delta X}$$

$$= H_{ij}\overline{\Delta X}\,\overline{\Delta Y}\frac{(P_{ij}^{n+1} - P_{ij}^{n+\frac{1}{2}})}{\Delta T} \tag{11.54}$$

It should be noted that in the first half-time step, only the Y direction is implicit while the X direction is explicit. On the other hand, in the second half-time

step, X direction becomes implicit and Y becomes explicit. In either step, the most recent values are used for the explicit terms; for example, in the second half-time step, the coefficients and the explicit terms are evaluated by using the values from the first half-time step.

It should also be noted that from examining equations (11.53) and (11.54), it is clear that terms involving $P_{i,j}$ from the X and Y directions are kept separate in the two half-time steps. However, in Successive Line Relaxation method, the $P_{i,j}$ terms from the two directions are assumed to be implicit. Therefore, the two half-time steps given by equations (11.53) and (11.54) become :

1st Step:

$$\left[A^- P^n_{i-1,j} - A^- P^{n+\frac{1}{2}}_{ij} + C^-_2 P^n_{i-1,j} - A^+ P^{n+\frac{1}{2}}_{ij} + A^+ P^n_{i+1,j} - C^+_2 P^{n+\frac{1}{2}}_{ij} \right] \overline{\Delta Y}$$

$$+ \left[B^- P^{n+\frac{1}{2}}_{i,j-1} - B^- P^{n+\frac{1}{2}}_{ij} + C^-_4 P^{n+\frac{1}{2}}_{i,j-1} - B^+ P^{n+\frac{1}{2}}_{ij} + B^+ P^{n+\frac{1}{2}}_{i,j+1} - C^+_4 P^{n+\frac{1}{2}}_{ij} \right] \overline{\Delta X}$$

$$= H_{ij} \overline{\Delta X} \, \overline{\Delta Y} \frac{(P^{n+\frac{1}{2}}_{ij} - P^n_{ij})}{\Delta T} \tag{11.55}$$

2nd Step:

$$\left[A^- P^{n+1}_{i-1,j} - A^- P^{n+1}_{ij} + C^-_2 P^{n+1}_{i-1,j} - A^+ P^{n+1}_{ij} + A^+ P^{n+1}_{i+1,j} - C^+_2 P^{n+1}_{ij} \right] \overline{\Delta Y}$$

$$+ \left[B^- P^{n+\frac{1}{2}}_{i,j-1} - B^- P^{n+1}_{ij} + C^-_4 P^{n+\frac{1}{2}}_{i,j-1} - B^+ P^{n+1}_{ij} + B^+ P^{n+\frac{1}{2}}_{i,j+1} - C^+_4 P^{n+1}_{ij} \right] \overline{\Delta X}$$

$$= H_{ij} \overline{\Delta X} \, \overline{\Delta Y} \frac{(P^{n+1}_{ij} - P^{n+\frac{1}{2}}_{ij})}{\Delta T} \tag{11.56}$$

In this study, the above mentioned scheme is called the Alternating Direction Successive Line Relaxation (ADSLR) scheme. The only difference between the ADI and ADSLR scheme is the manner in which the $P_{i,j}$ terms are treated.

Following the above outlined steps, two equations similar to equations (11.53) and (11.54) or equations (11.55) and (11.56) can be written for each interior grid point depending on whether ADI or ADSLR scheme is used. The resulting set of equations when written in matrix form is tridiagonal and can be easily solved by using Gaussian Elimination. Therefore, to solve for the steady-state solution, the scheme is iterated until the solution does not change between (full) time steps.

APPENDIX E

VARIABLE GRID SPACING ASSIGNMENT SCHEDULE

In this appendix, the scheme used to assign the variable grid spacing in the numerical algorithms is outlined. Variable grid spacing in both the X and Y directions were used, but a much finer mesh is used in the X direction. The same variable grid assignment scheme was used for all the different numerical algorithms tested. All the computer codes developed during the course of this project can handle grid size up to 51 points along the bearing and 21 points across the bearing. However, for all cases studied, 21 grid points were used in the Y direction even when symmetry is present. Thus in effect, when there is symmetry, 21 grid points are assigned across half the bearing width with the effect of assigning 41 grid points across the entire bearing. Therefore, a more accurate solution can be obtained. On the other hand, in the X direction, the number of grid points assigned is dependent on the operating bearing number based on the trailing edge clearance with a minimum of 45 grid points and a maximum of 51 grid points. Thus, if the bearing number is very large, 51 grid points would be used, while if the bearing number is small, only 45 grid points would be used. The exact number of grid points to use is decided by the computer based on the bearing number. In any case, there would be always 9 grid points assigned to the ramp region. The variable grid assignment was

designed such that fine grids are joined with coarse grids with grids of intermediate sizes.

The scheme used to assigned the variable grid mesh is given below which is taken from the computer program developed during the course of this project. Because the program was designed to handle either constant grid spacing or variable grid spacing, the scheme used to assign constant grid spacing is also given below. It should be noted that unless the ramp length is an integral fraction of the "land" section, it would be impossible to assign constant grid spacing throughout the length of the bearing. Consequently, there would be one grid spacing which will be different from the rest. This special situation is fully accounted for in the constant grid assignment scheme.

The grid assignment scheme used for either constant grid or variable grid spacing are as follows: (The notation used are self-explanatory)

```
C *****************************************************
C ******AUTOMATIC GRID SPACING ASSIGNMENT ********
C *****************************************************
C
C *** GRIDX - LOGICAL VARIABLE
C          - .TRUE. MEANS X SPACING SPECIFIED
      IF(GRIDX) GO TO 20
C *** EGRIDX - LOGICAL VARIABLE
C          - .TRUE. MEANS CONSTANT GRID
      IF(EGRIDX) GO TO 50
C *** VARIABLE GRID ASSIGNMENT IN X DIRECTION
C
C *** NXR - NUMBER OF DIVISIONS IN THE RAMP REGION
C
      NXR=8
      NXR1=NXR+1
      NXL=22
C
```

```
C *** XL  - LENGTH OF THE BEARING
C *** XLR - LENGTH OF THE RAMP REGION
C
      DXR=XLR/20.0
      DXR4=DXR*4
C
C *** ASSIGN GRID SPACING IN THE RAMP REGION
C
      DO 30 I=1,4
      DX(I)=DXR4
      DX(I+4)=DXR
   30 CONTINUE
C
C *** ASSIGN GRID SPACING AFTER THE BREAK
C
      DXF=(XL-XLR)/FLOAT(NXL)
      DXF14=DXF/4.0
      DXFH=DXF/2.0
      DXF34=DXF*3.0/4.0
      DX(NXR1)=DXFH
      DX(NXR1+1)=DXFH
      DX(NXR1+2)=DX34
      DX(NXR1+3)=DX34
      DX(NXR1+4)=DX34
      DX(NXR1+5)=DX34
      NXR6=NXR1+6
C
C *** ASSIGN GRID SPACING BEFORE THE TRAILING EDGE
C
C *** BEARNO  -  BEARING NUMBER BASED ON THE
C ***              TRAILING EDGE CLEARANCE
C ***              ( = 6*VISC*U*XL/PA/HT/HT)
C
      TEXL=139.0/15.0/BEARNO
      NXFLAT=NXR1+NXL+2
      NXFACT=INT(TEXL/DXF)
      NXFLAT=NXFLAT-NXFACT
      TEMP=TEXL-(FLOAT(NXFACT)*DXF)
      ITEMP=INT(TEMP/DXF14)
      IFORK=ITEMP+1
      GO TO (31,32,33,34), IFORK
   31 DX(NXFLAT+1)=DXF14
      DX(NXFLAT+2)=DXF14
      DX(NXFLAT+3)=DXF14
      DX(NXFLAT+4)=DXF14-TEMP
      GO TO 35
   32 DX(NXFLAT+1)=DXF14
      DX(NXFLAT+2)=DXF14
      DX(NXFLAT+3)=DXFH-TEMP
      GO TO 35
   33 DX(NXFLAT+1)=DXF14
      DX(NXFLAT+2)=DXF34-TEMP
      GO TO 35
```

```
                   34 DX(NXFLAT+1)=DXF-TEMP
                   35 II=NXFLAT+4-ITEMP+1
                      NXF=NXFLAT-6
                      DO 36 I=NXR6,NXF
                      DX(I)=DXF
                   36 CONTINUE
                      DX(NXF+1)=DXF34
                      DX(NXF+2)=DXF34
                      DX(NXF+3)=DXF34
                      DX(NXF+4)=DXF34
                      DX(NXF+5)=DXFH
                      DX(NXFLAT)=DXFH
      C
      C *** ASSIGN FINE GRID SPACING AT THE TRAILING EDGE
      C
                      TEMP=1.0/BEARNO
                      DX(II)=3.0*TEMP
                      DX(II+1)=2.0*TEMP
                      DX(II+2)=TEMP
                      DX(II+3)=TEMP
                      DX(II+4)=TEMP/2.0
                      DX(II+5)=TEMP/2.0
                      DX(II+6)=TEMP/4.0
                      DX(II+7)=TEMP/4.0
                      DX(II+8)=TEMP/5.0
                      DX(II+9)=TEMP/5.0
                      DX(II+10)=TEMP/5.0
                      DX(II+11)=TEMP/10.0
                      DX(II+12)=TEMP/15.0
                      NX=II+12+1
                      NXM1=NX-1
      C *** END OF VARIABLE GRID ASSIGNMENT IN X DIRECTION
                      GO TO 20
      C
      C *** CONSTANT GRID SPACING ASSIGNMENT IN X DIRECTION
      C
      C *** NXL - NUMBER OF DIVISION WANTED IN THE LAND SECTION
      C
                   50 DDX=(XL-XLR)/NXL
      C *** CHECK TO SEE IF RAMP LENGTH IS AN INTEGRAL
      C            FRACTION OF THE LAND SECTION
                      FACT=XLR/DDX
                      NXR=INT(FACT)+1
      C *** IF IT IS NOT, TAKE CARE OF THE ODD BALL WITH 'DX1'
                      DX1=(FACT-FLOAT(NXR-1))*DDX
                      DX(1)=DX1
      C *** NX - TOTAL NUMBER OF GRID POINTS (MAX OF 51)
                      NX=NXR+NXL+1
                      NXR1=NXR+1
                      NXM1=NX-1
                      DO 70 I=2,NXM1
                      DX(I)=DDX
                   70 CONTINUE
```

```
C *** END OF CONSTANT GRID SPACING ASSIGNMENT
C ***          IN X DIRECTION
C
C *** GRID ASSIGNMENT IN Y DIRECTION
C
C *** GRIDY - LOGICAL VARIABLE
C            - .TRUE. MEANS Y GRID SPECIFIED
   20 IF(GRIDY) GO TO 80
C *** EGRIDY - LOGICAL VARIABLE
C            - .TRUE. MEANS CONSTANT Y GRID
      IF(EGRIDY) GO TO 110
C *** VARIABLE GRID ASSIGNMENT IN Y DIRECTION
      IF(.NOT.SYMM) GO TO 81
C *** SYMMETRY  (HALF BEARING WIDTH)
      DYSUM=0.0
C *** YW - BEARING WIDTH
      DYW4=YW/2.0/20.0/4.0
      DO 91 J=1,6
      DY(J)=DYW4
      DYSUM=DYSUM+DY(J)
   91 CONTINUE
      DO 92 J=7,9
      DY(J)=2.0*DYW2
      DYSUM=DYSUM+DY(J)
   92 CONTINUE
      DDY=(YW/2.0-DYSUM)/11.0
      DO 93 J=10,20
      DY(J)=DDY
   93 CONTINUE
C *** END OF SYMMETRIC CASE
      GO TO 80
C *** NON-SYMMETRIC CASE  (Y GRID SPACING)
   81 CONTINUE
      DYSUM=0.0
      DYW4=YW/20.0/4.0
      DO 94 J=1,3
      DY(J)=DYW4
      DYSUM=DYSUM+DY(J)
   94 CONTINUE
      DO 95 J=4,6
      DY(J)=2.0*DYW4
      DYSUM=DYSUM+DY(J)
   95 CONTINUE
      DDY=(Y2/2.0-DYSUM)/4.0
      DO 96 J=7,10
      DY(J)=DDY
   96 CONTINUE
      DO 97 J=11,20
      JJ=21-J
      DY(J)=DY(JJ)
   97 CONTINUE
C *** END OF VARIABLE GRID SPACING IN Y DIRECTION
      GO TO 80
```

```
C
C *** CONSTANT GRID SPACING IN Y DIRECTION
C
  110 CONTINUE
C *** MY - NUMBER OF GRID POINTS IN Y (MAX OF 21)
      MYM1=MY-1
      DDY=YW/MYM1
      DO 120 J=1,MYM1
      DY(J)=DDY
  120 CONTINUE
C *** END OF GRID ASSIGNMENT ROUTINE ***
   80 IF(SYMM) DY(MY)=DY(MYM1)
C ********************************************************
C ********************************************************
```

DISTRIBUTION LIST FOR UNCLASSIFIED
TECHNICAL REPORTS ISSUED UNDER

CONTRACT N00014-75-C-0552 TASK 062-491

All addressees receive one copy unless otherwise specified

Defense Documentation Center
Cameron Station
Alexandria, VA 22314   12 copies

Professor Bruce Johnson
U.S. Naval Academy
Engineering Department
Annapolis, MD 21402

Technical Library
David W. Taylor Naval Ship Research
    and Development Center
Annapolis Laboratory
Annapolis, MD 21402

Professor C. S. Yih
The University of Michigan
Department of Engineering Mechanics
Ann Arbor, MI 48109

Professor T. Francis Ogilvie
The University of Michigan
Department of Naval Architecture
    and Marine Engineering
Ann Arbor, MI 48109

Office of Naval Research
Code 211
800 N. Quincy Street
Arlington, VA 22217

Office of Naval Research
Code 438
800 N. Quincy Street
Arlington, VA 22217   3 copies

Office of Naval Research
Code 473
800 N. Quincy Street
Arlington, VA 22217

Library
U.S. Naval Academy
Annapolis, MD 21402

NASA Scientific and Technical
    Information Facility
P.O. Box 8757
Baltimore/Washington International
    Airport
Maryland 21240

Professor Paul M. Naghdi
University of California
Department of Mechanical Engineering
Berkeley, CA 94720

Librarian
University of California
Department of Naval Architecture
Berkeley, CA 04720

Professor John V. Wehausen
University of California
Department of Naval Architecture
Berkeley, CA 94720

Library
David W. Taylor Naval Ship Research
    and Development Center
Code 522.1
Bethesda, MD 20084

Mr. Justin H. McCarthy, Jr.
David W. Taylor Naval Ship Research
    and Development Center
Code 1552
Bethesda, MD 20084

Dr. William B. Morgan
David W. Taylor Naval Ship Research
    and Developemnt Center
Code 1540
Bethesda, MD 20084

Director
Office of Naval Research Branch Office
Building 114, Section D
666 Summer Street
Boston, MA 02210

Library
Naval Weapons Center
China Lake, CA 03555

Technical Library
Naval Surface Weapons Center
Dahlgren Laboratory
Dahlgren, VA 22418

Technical Documents Center
Army Mobility Equipment Research
  Center
Building 315
Fort Belvoir, VA 22060

Technical Library
Webb Institute of Naval Arch.
Glen Cove, NY 11542

Dr. J.P. Breslin
Stevens Institute of Technology
Davidson Laboratory
Castle Point Station
Hoboken, NJ 07030

Professor Louis Landweber
The University of Iowa
Institute of Hydraulic Research
Iowa City, IA 52242

R.E. Gibson Library
The Johns Hopkins University
Applied Physics Laboratory
Johns Hopkins Road
Laurel, MD 20810

Lorenz G. Straub Library
University of Minnesota
St. Anthony Falls Hydraulic Lab.
Minneapolis, MN 55414

Library
Naval Postgraduate School
Monterey, CA 93940

Technical Library
Naval Underwater Systems Center
Newport, RI 02840

Engineering Societies Library
345 East 47th Street
New York, NY 10017

The Society of Naval Architects
   and Marine Engineers
One World Trade Center, Suite 1369
New York, NY 10048

Technical Library
Naval Coastal System Laboratory
Panama City, FL 32401

Professor Theodore Y. Wu
California Institute of Technology
Engineering Science Department
Pasadena, CA 91125

Technical Library
Naval Ship Engineering Center
Philadelphia Division
Philadelphia, PA 19112

Director
Office of Naval Research Branch Office
1030 E.Green Street
Pasadena, CA 91125

Army Research Office
P.O. Box 12211
Research Triangle Park, NC 27709

Editor
Applied Mechanics Review
Southwest Research Institute
8500 Culebra Road
San Antonio, TX 78206

Technical Library
Naval Ocean Systems Center
San Diego, CA 92152

ONR Scientific Liaison Group
American Embassy - Room A-407
APO San Francisco 86503

Librarian
Naval Surface Weapons Center
White Oak Laboratory
Silver Sprin-, MD 20910

Defense Research and Development Attache
Australian Embassy
1601 Massachusetts Avenue, NW
Washington D.C. 20036

Librarian Station 5-2
Coast Guard Headquarters
NASSIF Building
400 Seventh Street, SW
Washington D.C. 20591

Library of Congress
Science and Technology Division
Washington, D.C. 20540

Dr. A. L. Slafkosky
Scientific Advisor
Commandant of the Marine Corps
Code AX
Washington, D.C. 20380

Maritime Administration
Office of Mariotime Technology
14th & E Streets, NW
Washington, D.C. 20230

Maritime Administration
Division of Naval Architecture
14th & E Street, NW
Washington, D.C. 20230

Dr. G. Kulin
National Bureau of Standards
Mechanics Section
Washington, D.C. 20234

Naval Research Laboratory
Code 2627
Washington, D.C. 20375 6 copies

Library
Naval Sea Systems Command
Code 09GS
Washington, D.C. 20362

Mr. Thomas E. Peirce
Naval Sea Systems Command
Washington, D.C. 20362

Commanding Officer
NROTC Naval Administrative Unit
Massachusetts Institute of
    Technology
Cambridge, MA 02139

Oceanographer of the Navy
200 Stovall Street
Alexandria, VA 22332

Office of Naval Research
Code 212
800 N. Quincy Street
Arlington, VA 22217

Office of Naval Research
Code 221
Arlington, VA 22217

Dr Coda H. T. Pan
Shaker Research Corporation
Northway 10, Executive Park
Ballston Lake, NY 12019

Mr. William M. Ellsworth
David W. Taylor Naval Ship Research
    and Development Center
Code 1100
Bethesda, MD 20084

Dr. Francois N. Frenkiel
David W. Taylor Naval Ship Research
    and Development Center
Code 1802.2
Bethesda, MD 20084

Dr. Alan Powell
David W. Taylor Naval Ship Research
    and Development Center
Code 0100
Bethesda, MD 20084

Commander
Puget Sound Naval Shipyard
Bremerton, WA 98314

Mr. S. Abramovitz
Abramovitz Associates Inc.
P.O. Box 393
Bronxville, NY 10708

Dr. Alfred Ritter
Calspan Corporation
Advanced Tbchnology Center
P.O. Box 400
Buffalo, NY 14225

Library
C.S. Draper Laboratory
Technology Square
Cambridge, MA 02139

Dr. Edgar J. Gunter, Jr
University of Virginia
School of Engineering and
    Applied Science
Charlottesville, VA 22903

Professor A.R. Kuhlthau
Director, Research Laboratories
    for the Engineering Sciences
Thornton Hall
University of Virginia
Charlottesville, VA 22903

Professor L. N. Tao
Illinois Institute of Technology
Chicago, IL 60616

Mr. William J. Anderson
NASA Lewis Research Center
Cleveland, OH 44135

Commander
Charleston Naval Shipyard
Naval Base
Charleston, SC 29408

Mr. J.W. Kannel
Battelle Memorial Institute
505 King Avenue
Columbus, OH 43201

Mr. Richard P. Shevchenko
Pratt and Whitney Aircraft Corp.
East Hartford, CT 06103

Mr. H. M. Anderson
Xerox Data Systems
701 South Aviation Boulevard
El Segundo, CA 90245

Professor Ralph Burton
Northwestern University
Department of Mechanical
    Engineering and Astronautical
    Sciences
Evanston, IL 60210

Commander
Long Beach Naval Shipyard
Long Beach, CA 90801

Mr. L. R. Manoni
Manager, Advanced Programs
United Aircraft Corporation
    Systems Center
1690 New Britain Avenue
Farmington, CT 06023

Research and Technology Division
Army Engineering Reactors Group
Fort Belvoir, VA 22060

Mr. Peter H. Broussard, Jr.
National Aeronautics and Space
    Administration
George C. Marshall Space Flight Center
Guidance and Control Division
Huntsville, AL 35812

Professor William K. Stair
Assistant Dean, Mechanical and
    Aerospace Engineering
University of Tennessee
Knoxville, TN 37916

Professor J. Modrey
Purdue University
School of Mechanical Engineering
Lafayette, IN 47907

Professor Albert T. Ellis
Universtiy of California, San Diego
Department of Allied Mechanics
    and Engineering Sciences
La Jolla, CA 92093

Professor William R. Lindbert
University of Wyoming
Department of Mechanical Engineering
Laramie, WY 82071

Mr. Otto Decker
Mechanical Techology Incorporated
968 Albany-Shaker Road
Latham, NY 12110

Mr. Wilbur M. Shapiro
Mechanical Technology Incorporated
968 Albany-Shaker Road
Latham, NY 12110

Mr. Philip Eisenberg
Presiden, Hydronautics, Incorporated
7210 Pindell School Road
Laurel, MD 20810

Mr. Bill Holliday
Head & Media Development
Control Data Corporation
Normandale Division
7801 Computer Avenue
Minneapolis, MN 55424

Professor Paul F. Pucci
Naval Postgraduate School
Mechanical Engineering Department
Monterey, CA 93940

Professor Vittorio Castelli
Columbia University
Department of Mechanical
    Engineering
New York, NY 10027

Professor Harold G. Elrod
Columbia University
Department of Mechanical
    Engineering
New York, NY 10027

Professor Dudley D. Fuller
Columbia University
Department of Mechanical
    Engineering
New York, NY 10027

Mr. Ralph F. DeAngelias
Norden Division of United
    Technology Research Center
Helen Street
Norwalk, CT 06852

Mr. Anthony W. Lawrence
Northrop Corporation
Electronics Devision
100 Morse Street
Norwood, MA 02062

Mr. R. G. Jordan
Oak Ridge Gaseous Diffusion Pl.
Union Carbide Corporation –
    Nuclear Division
P.O. Box P
Oak Ridge, TN 37830

Mr. Harry Rippel
Franklin Research Center
A Division of the Franklin Institute
Mechanical Engineering Laboratory
The Benjamin Franklin Parkway
Philadelphia, PA 19103

Technical Library
Philadelphia Naval Shipyard
Philadelphia, PA 19112

Dr. F. Osterle
Carnegie Institute of Technology
Department of Mechanical Engineering
Pttsburgh, PA 15213

Technical Library
Naval Missile Center
Point Mugu, CA 93041

Commander
Norfolk Naval Shipyard
Portsmouth, VA 23709

Commander
Portsmouth Naval Shipyard
Portsmouth, NH 03801

Mr. Rabab Shahbender
RCA Laboratories
David Sarnoff Research Center
Princeton, NJ 08540

Chief, Document Section
Redstone Scientific Information
    Center
Army Missile Command
Redstone Arsenal, AL 35809

Dr. A. Eshel
Ampex Corporation
401 Broadway
Redwood City, CA 94063

Mr. Manfred Wildmann
Ampex Corporation
Advanced Technology Division
401 Broadway
Redwood City, CA 94063

Mr. Kenneth A. Liebler
Director of Engineering
National Micronetics, Inc.
5600 Kearny Mesa Road
San Diego, CA 92111

Dr. Jack W. Hoyt
Naval Ocean Systems Center
Code 2501
San Diego, CA 92152

Page 6

Technical Library
Hunters Point Naval Shipyard
San Francisco, CA 94135

Library
Pearl Harbor Naval Shipyard
Box 400
FPO San Francisco, CA 96610

Mr. C. C. Moore
Manager. Reliability and
    Safety Engineering
Gas Turbine Division
General Electric Company
Schenectady, NY 12345

Professor Bruce H. Adee
University of Washington
Department of Mechanical
    Engineering
Seattle, WA 98195

Mr. Arthur Huxley
Admiralty Compass Observatory
Ditton Park
Slough, Berks, England

Mr. Roland Baldwin
Section Head - Inertial Components
Honeywell Inc., Aerospace Division
13350 U.S. Highway 19
St. Petersburg, FL 33733

Professor Richard C. DiPrima
Rensselaer Polytechnic Institute
Department of Mathematical Sciences
Troy, NY 12181

Mr. Walt Tucker
Brookhaven National Laboratory
Nuclear Engineering Department
Upton, NY 11973

Technical Library
Mare Island Naval Shipyard
Vallejo, CA 94592

Mr. E. Roland Maki
General Motors Corporation
Mechanical Development Department
12 Mile and Mound Roads
Warren, MI 48090

AFDRD-AS/M
U.S. Air Force
The Pentagon
Washington, D.C. 20330

Air Force Office of Scientific
    Research/NA
Building 410
Bolling AFB
Washington, D.C. 20332

Mr. W. M. Crim
Department of Energy
Office of Coal Research
400 1st Street, NW
Washington, D.C. 20545

Mr. Clarence E. Miller, Jr.
Department of Energy
Division of Reactor Development
    and Technology
400 1st Street, NW
Washington, D.C. 20545

Professor J. V. Foa
George Washington University
School of Engineering and
    Applied Science
Washington, D.C. 20006

Naval Air Systems Command
Code 03
Washington, D.C. 20361

Naval Air Systems Command
Code 03B
Washington, D.C. 20361

Naval Air Systems Command
Code 310
Washington, D.C. 20361

Naval Air Systems Command
Code 5301
Washington, D.C. 20361

Library
Naval Sea Systems Command
Code 09GS
Washington, D.C. 20362

Naval Ship Engineering Center
Code 6034
Washington, D.C. 20362

Page 7

Naval Ship Engineering Center
Code 6101
Washington, D.C.   20362

Naval Ship Engineering Center
Code 6110
Washington, D.C.   20362

Naval Ship Engineering Center
Code 6114
Washington, D.C.   20362

Naval Ship Engineering Center
Code 6136
Washington, D.C.   20362

Naval Ship Engineering Center
Code 6140
Washington, D.C.   20362

Strategic Systems Projects Office
Department of the Navy
Washington, D.C.   20376

Mr. R. Dayton
Air Force Aero Propulsion Laboratory
Wright-Patterson AFB, OH   45433

REPORT DOCUMENTATION PAGE	READ INSTRUCTIONS BEFORE COMPLETING FORM

1. REPORT NUMBER	2. GOVT ACCESSION NO.	3. RECIPIENT'S CATALOG NUMBER
No. 28	AD-A087 400	

4. TITLE (and Subtitle)	5. TYPE OF REPORT & PERIOD COVERED
Experimental Investigation of Hydrodynamic Self-Acting Gas Bearings at High Knudsen Numbers	FINAL 1977 - 1980
	6. PERFORMING ORG. REPORT NUMBER

7. AUTHOR(s)	8. CONTRACT OR GRANT NUMBER(s)
Yiao-Tee Hsia and Gerald A. Domoto	N00014-75-C-0552

9. PERFORMING ORGANIZATION NAME AND ADDRESS	10. PROGRAM ELEMENT, PROJECT, TASK AREA & WORK UNIT NUMBERS
Columbia University Tribology and Lubrication Research Lab. New York, New York 10027	TASK NR 062-491

11. CONTROLLING OFFICE NAME AND ADDRESS	12. REPORT DATE
Office of Naval Research Code 438, 800 N. Quincy Street Arlington, VA 22217	July 1, 1980
	13. NUMBER OF PAGES
	136

14. MONITORING AGENCY NAME & ADDRESS(If different from Controlling Office)	15. SECURITY CLASS. (of this report)
(same as above)	Unclassified
	15a. DECLASSIFICATION/DOWNGRADING SCHEDULE

16. DISTRIBUTION STATEMENT (of this Report)

Qualified requestors may obtain copies of this report from D.D.C.

This document has been approved for public release and sale; its distribution is unlimited.

17. DISTRIBUTION STATEMENT (of the abstract entered in Block 20, if different from Report)

18. SUPPLEMENTARY NOTES

19. KEY WORDS (Continue on reverse side if necessary and identify by block number)

Modified Reynolds Equation; Maxwell Slip Boundary; Molecular Slip; Mean Free Path; Ambient and Local Knudsen Number; Modified Bearing (Compressibility) Number; Transition Flow; Surface Accommodation Coefficient; Narrow Bearing; Alternating Direction Successive Line Relaxation Scheme.

micrometers

20. ABSTRACT (Continue on reverse side if necessary and identify by block number)

This investigation gives experimental confirmation of the "slip flow" theory, developed by Burgdorfer, for modelling hydrodynamic gas bearing with clearances below 0.25 μm. An interferometric technique using two CW lasers is used to measure the small clearances with an 0.025 μm accuracy. The pitch and roll angles of the slider bearing and the surface contour of the slider are also measured interferometrically. → next page

(over)

DD FORM 1473 EDITION OF 1 NOV 68 IS OBSOLETE
1 JAN 73

BLOCK 20: (continued)

The effects of molecular rarefaction are studied by operating the bearing in different gas media with different mean free paths. Air is used to study Knudsen number below 0.5 while helium is used to study Knudsen number above 0.5.

Experimentally measured trailing edge clearances and pitch angles are compared with theoretical predictions using the "modified" Reynolds equation with velocity slip boundary conditions. The modified Reynolds equation is solved numerically using two different numerical algorithms. Excellent agreement between experiment and theory is found for clearances as high as 1.60 μm to as low as 0.075 μm with corresponding ambient Knudsen number of 0.04 and 2.51, respectively.

* * * * * * * * * * * * * * * * * * . * *

Micrometers

D
FI
9